All-Dielectric Metasurfaces for Sensing Applications

INAUGURALDISSERTATION

zur Erlangung der Würde eines Doktors der Philosophie vorgelegt der Philosophisch-Naturwissenschaftlichen Fakultät der Universität Basel

von

Giulia PRONE

2023

Genehmigt von der Philosophisch-Naturwissenschaftlichen Fakultät

auf Antrag von

Prof. Dr. Marcel Mayor,

Prof. Dr. Michel Calame und

Prof. Dr. Christophe Galland.

Basel, den 13. Dezember, 2022

Prof. Dr. Marcel Mayor

Dekan

Acknowledgments

I would like to thank everyone who has taken the time to listen to my requests, provided me with fantastic ideas, and offered me support over these intense and productive years. This work would not have been feasible without the great skills and personalities that surrounded me on a daily basis.

Many thanks to PROF. MARCEL MAYOR, my academic supervisor at the University of Basel, for motivating me to undertake this research project and providing helpful comments throughout my PhD studies. I am also grateful to PROF. MICHEL CALAME from the University of Basel and EMPA for serving as the second academic supervisor, and to PROF. CHRISTOPHE GALLAND from EPFL Lausanne for serving as an external expert in my PhD committee. NATHALIE PLATTNER-LONGHI's administrative assistance is also greatly appreciated.

I am grateful to DR. EMANUEL LÖRTSCHER, my supervisor at IBM Research Europe - Zurich in Rüschlikon, for allowing me to conduct my research in the Binnig and Rohrer Nanotechnology Center. His feedback and the frequent exchanges encouraged me in steering my research in the right direction. I would also want to express my gratitude to DR. THOMAS BRUNSCHWILER, DR. BRUNO MICHEL, DR. HEIKE RIEL, and DR. ALESSANDRO CURIONI for their continuous support.

At IBM Research Europe - Zurich in Rüschlikon, I would like to express my gratitude to the entire cleanroom operations team as well as the teams

from the modelshop, stockroom, and chemical coordination. I would especially want to thank DR. ANTONIS OLZIERSKY for his assistance with e-beam lithography, UTE DRECHSLER for her expert advise in improving my fabrication procedures, and ROBERT LOVCHIK for his assistance with the microfluidic and surface chemistry aspects of my project. TRUDI ENDER's administrative assistance is also greatly appreciated. I am really grateful to DR. DOMINIK SCHERRER, DIEGO MONSERRAT LÓPEZ, GIAN-MARCO GABRIELI, SERPIL KIOKEKLI, and EMANUELE PICCOLI for creating a great working atmosphere in our IBM work sub-group. I loved working with the Mayor research group's TIM HOHNER, DAVID VOGEL, and JÖEL KELLER.

Finally, many thanks to my parents, my partner MATTHIAS, and friends that supported and loved me throughout this long process.

To my parents.
Everything I have and everything I am, I owe it all to you.

Abstract

Dielectric metasurfaces are a family of flat-optical components that offer novel approaches to light manipulation, paving the way to exciting new applications. Regardless of the underlying operating theory, realizing such nanometer-sized devices calls for excellent fabrication accuracy, ideally on the sub-10 nm level, especially if resonance conditions need to be matched. Electron-beam lithography (EBL) is capable of achieving such feature sizes. Transparent substrates as used for optical transmission devices, however, present a big challenge as charge carriers accumulate in the substrate and cause long-range proximity effects. Furthermore, EBL's sequential exposure drastically limits the size of exposable areas, making it practically unaffordable for applications beyond research.

The aim of this thesis was to design and characterize structures engineered at the nano-scale, called metasurfaces, to implement compact optical elements and systems with capabilities beyond those of conventional refractive and diffractive optics.

The first chapter addresses the theoretical aspects of nanophotonics, metasurfaces, and sensing modalities. The second chapter will include a brief overview of the metasurfaces concept, unit-cell design, and pattern choice. The design and simulation of tilted arrays of elliptical-shaped dielectric unit-cells will be presented. In Chapter 3, the emphasis is on the metasurfaces manufacturing, beginning with the fabrication challenges that must be addressed to construct such a device, and a brief description of electron-beam lithography (EBL) and nanoimprint lithography (NIL). Following that, a

three-layer transfer technique based on EBL and NIL is described. The results for master fabrication, substrate preparation, NIL patterning, pattern transfer, metrology, and overall fabrication will be discussed. The fourth chapter will provide a customized microscopy setup for measuring the intensity variations of the created metasurfaces. First, a quick explanation of optical transmission spectroscopy and the overall signal processing method that will be used in the subsequent chapters will be provided. Following that, a brief overview of microfluidic devices with metasurfaces will be provided. The optical setup will then be presented, and system control will be demonstrated using commercially available software. Finally, the design and fabrication of a microfluidic chamber will be shown. Chapter 5 will provide an overview of the various strategies for tuning dielectric metasurfaces, with a focus on the tunability provided by geometrical modifications and changes in the refractive index of the immediate environment. In Chapter 6, a universal immobilization technique for structures exposing a sulfhydryl group (thiols) on silicon substrates will be shown, and contact-angle goniometric and XPS studies will be used to monitor surface changes. Following that, experimental streptavidin sensing will be demonstrated employing arrays of silicon nanoellipse resonators coated with biotin. Finally, Chapters 7 and 8 will provide an overview of the preceding chapters' outcomes as well as an outlook on future applications.

Contents

"È sapiente solo chi sa di non sapere, non chi s'illude di sapere e ignora così perfino la sua stessa ignoranza."

Socrate

Chapter 1

Introduction

The promising potential of refractive index engineering, as well as advances in transformation optics, have been a key trigger for the growing focus on metamaterials in recent years. Metamaterials are new synthetic materials designed to achieve unique properties, not normally present in nature. This chapter begins with a theoretical introduction to nanophotonics and metasurfaces. Then, the recent advances and developments of different optical metasurface platforms are discussed and the operational principles of the dielectric metasurface platform are explained, which is the basis of all the work presented in the following chapters. In the end, a brief description of the content of the thesis is provided.

1.1 Photonics and Nanophotonics

Photonics has revolutionized our daily lives, introducing outstanding inventions and technologies. The exemplary consideration of the communications industry makes it clear that today's ubiquitous Internet owes its performance and speed only to innovations in optical physics. Similarly, imaging techniques in biology and medicine have benefited from advances in bio-photonics, which enable the imaging and even manipulation of living cells with photons. Furthermore, photonics enables the development of high efficiency devices in the fields of energy conversion for renewable

energy sources, which is a fundamental prerequisite for the decarboniza-
tion of energy production. Finally, many fabrication methods in nanotech-
nology would not work without advances in photonics. Likewise, many
nanoscale devices only work with photonic parts, such as miniaturized opti-
cal sensors[80].

Thanks to the ability to fabricate sub-wavelength precise systems using nan-
otechnology methods, confining of light became possible at the nanometer
scale, enabling the efficient generation of light, improved interaction between
light and matter, and the fabrication of high-precision optical sensors.

1.2   Photonic crystals

Photonic crystals (PhC) were one of the first miniaturized photonic systems
realized on a chip. It consists of periodic structures in which interchanged
zones of low and high refractive index are stacked in a determined way.
Photonic crystals are the optical counterpart of ions in the crystal lattice that
change the electrons in semiconductors, since they affect light through their
periodic structure, and then refractive index modulation. The many-scatter
behavior of light at the interfaces between the different refractive index re-
gions in the photonic crystal can cause destructive interferences, creating
band gaps. Consequently, it is possible to modify the photonic crystal struc-
tures as desired in order to propagate only determined wavelengths.

Photonic crystals can be divided into three main groups:

- **1D PhC**: the easier structure of a photonic crystal is constituted by
  thin film layers of different dielectric constants that are periodically de-
  posited on a surface (Figure 1.1, first column). This kind of photonic
  crystal occurs in nature, for example, in the colors present in certain
  parts of animals' bodies. The colored wings of butterflies (Figure 1.1 A)

represent a famous example. In 1887, Lord Rayleigh presented and fabricated the first artificial one-dimensional photonic crystal. The development of deposition techniques like atomic layer deposition (ALD), chemical vapor deposition (CVD), plasma enhanced CVD (PECVD), etc., paved the way for a wider variety of materials, together with a more precise fabrication, allowing for accurate tuning of the desired optical response. One-dimensional photonic crystals find many applications in optical systems, light sources, and lasers exploiting anti-reflection coatings, Bragg gratings, and efficient mirrors.

- **2D PhC**: this type of photonic crystals (Figure 1.1, middle column) is constituted by an alternation along two orientations of different dielectric constant materials. Also in this case, it is possible to find a counterpart in nature, for example peacock fathers (Figure 1.1 B) show a peculiar color, which looks brilliant and pearly. The first literature description of 2D PhCs is from 1987 by Eli Yablonovich and John Sajeev[71]. In 2D photonic crystals, holes are commonly drilled into a specific substrate presenting a high dielectric constant in a periodic pattern. To further tighten the light confinement, it is possible to include defects in the photonic crystal material, allowing manipulation up to the diffraction limit. Photonic crystals with customized, artificially put defects are suitable for optical memories with high efficiency, light guides, and ultrafast lasers[87,102,3].

- **3D PhC**: this kind of structure, like the previous ones, presents alternation of materials with different refractive indices (Figure 1.1, last column). Nature also exhibits these arrangements, including non-perfect three-dimensional photonic crystals in different families of beetles, but also different types of opals. Opals are composed of a face-centered cubic lattice formed by dielectric spherical self-assembled beads (Figure 1.1 C). By multi-step lithography techniques, it is possible to fabricate such structures artificially.

Photonic crystals represent an excellent way for manipulating light, however, the downscaling of such photonic devices based on photonic crystals is very demanding due to the intrinsically low dielectric constant in dielectric materials and the diffraction limit.
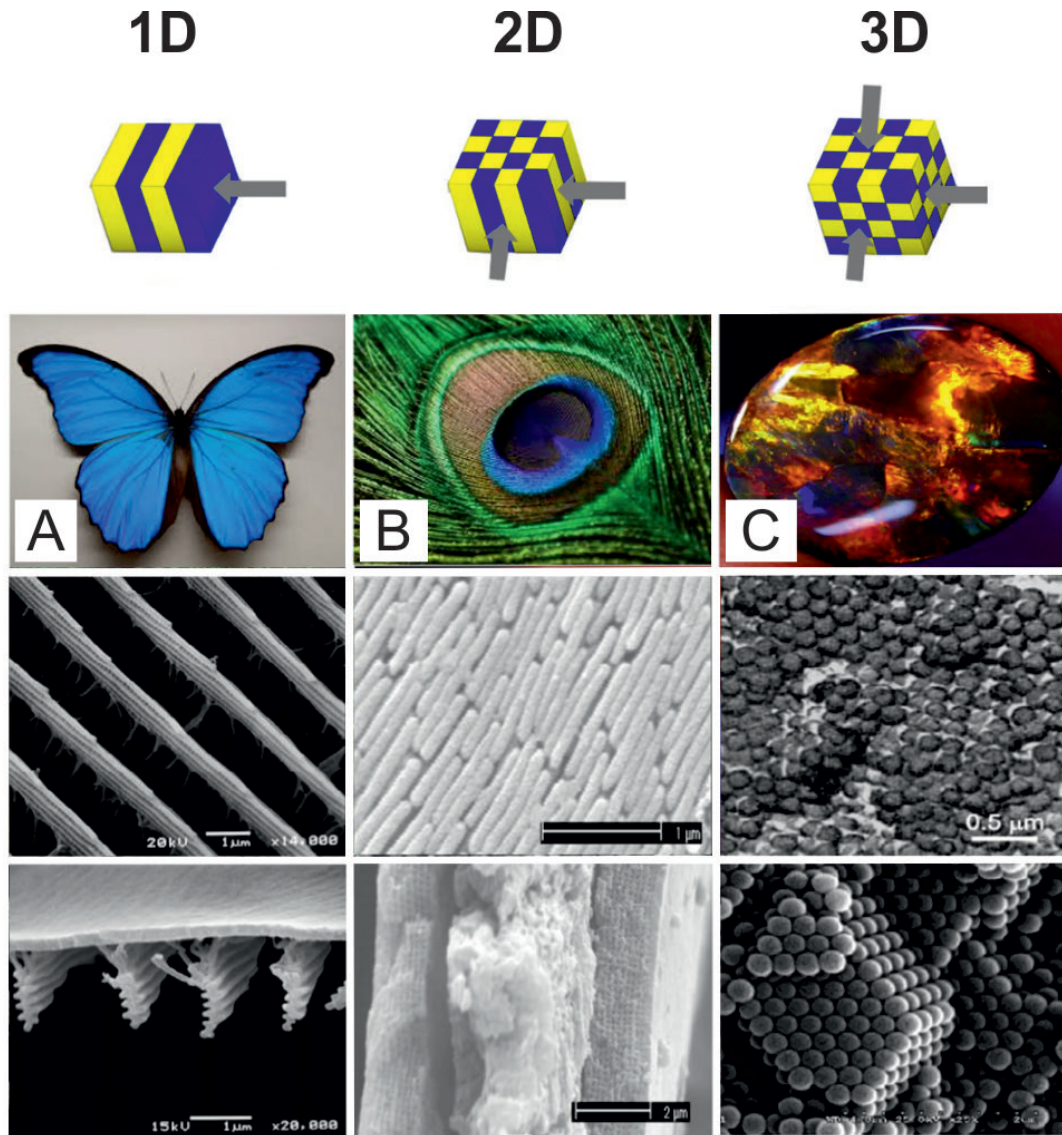

FIGURE 1.1: Schematic of photonic crystals in nature: Colored image and scanning electron microscope (SEM) images of (A) a Morpho butterfly, adapted from [177], (B) a peacock feather, adapted from [195], (C) opals, adapted from [107].

1.3 Surface Plasmon Polaritons

The fabrication of devices with surface plasmonic polaritons (SPPs) offers a viable way to control and regulate light propagation and dispersion at the nanometer scale[188], which helps to overcome the diffraction limit. The electromagnetic excitation that occurs at the boundary between a metal and a dielectric substance is more specifically represented by SPP. A highly increased optical near field can also be produced by the resonant interaction between SPP and outside electromagnetic radiation at metallic surfaces.

The propagation length of SPPs, together with many other characteristics, is dependent mainly on the dielectric constant ϵ. In an ideal material presenting negligible losses it is possible to express the dielectric permittivity with the formula:

$$\epsilon = n^2,$$

with n representing the refractive index of the material. In metals the permittivities present negative values, which can be order of magnitude bigger than the dielectric counterpart. This is due to the huge number of free electrons present in the conduction band, able to flow inside the crystal lattice. As shown in Figures 1.2 A and B, the mixed wave, given by photons and electric charge oscillations arising at the interface between metal and dielectric, represent the already mentioned SPP. Since metals show a high refractive index, the oscillations remain confined to narrow, subwavelength, volumes, greatly increasing the light-matter interactions.

SPPs were observed for the first time by Wood in 1902, since unexplained features were found in optical reflection measurements on metallic gratings[164]. Later on, Maxwell Garnett was able to observe bright colours appear on metal-doped glasses[110], and then, in 1908, Mie introduced the theory of light scattering by spherical particles in 1908[111].

Surface plasmon resonances were used for the first time in 1983, to distinguish really small changes in the refractive index localized at the interface

of a metal and a dielectric upon antibody binding[96]. It was measured as a shift of the reflectance peak in the light spectra, similarly to what is shown in Figure 1.2 C.

Nowadays, the SPR techniques represent the best approach for label free and real time chemical and biological interactions measurements. Among other things, the method is so favored because of its high reproducibility and sensitivity[65].
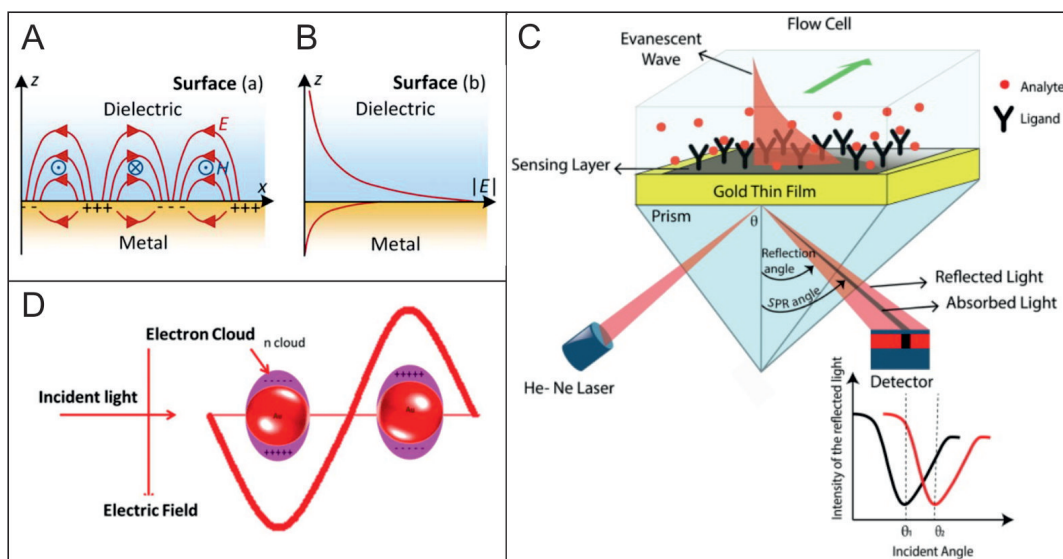
FIGURE 1.2: Localized surface plasmons and surface plasmon polaritons. (A) At the interface between a metal and a dielectric, the surface plasmon polariton's electric field can be generated. Figure adapted from ref. [78] (B) Propagation and decay of the electric field of the surface plasmon polariton. Figure adapted from ref. [78] (C) Schematics of an SPR sensor for biosensing applications and an SPR sensorgram displaying a resonance shift after the binding. Figure adapted from ref. [44]. (D) Schematics of localized surface plasmon resonance taking place in metal nanoparticles. Figure adapted from ref. [12].

1.4 Localized Surface Plasmon Polaritons

Additionally to surface plasmons occurring at the plane surface, other geometries can be considered, which include bound electron plasmons, such as metallic particles or voids of different topologies. In this case, it is possible to talk about localized surface plasmon resonances (LSPR) excitations[184]. Localized surface plasmon resonance (LSPR), Figure 1.2 D, is an optical phenomenon caused by light interacting with conductive nanoparticles (NPs) whose wavelength is smaller than that of the incident light. In surface plasmon resonance, electrons of a conduction band can be excited collectively by the electric field of incident light. As a consequence, coherent localized plasmon oscillations occur with a resonant frequency that is strongly influenced by the composition, size, geometry, dielectric environment, and separation distance of NPs[122].

Many applications have been already explored, starting with subwavelength wave-guides[103,104], thanks to the electromagnetic field confinement ability of this method, up to the performance optimization of computing systems. Nanoparticles are also exploited for energy generation, photocatalysis, photo-detection, H_2O desalination, up to medical applications like thermal cancer therapy and pregnancy tests[10,151,1,193,63,55].

1.5 Metamaterials

Metamaterials represent a new class of functional materials presenting special patterns and structures at the nano- and micro-scale, allowing them to interact with diverse types of energy systems that are not usually seen in nature. This type of material owns special properties and capabilities due to its artificial inner nanostructure together with the chemical composition of the chosen material itself, and that are making this kind of system capable of unique properties, not findable in common materials and fabrication

techniques. Metamaterials are constituted of different stacks of alternated elements that come from common materials like metals and dielectrics.

The properties and functions of a metamaterial are determined by its artificially designed structural units. The structural units of the metamaterial can be adapted and engineered in size and shape, the inter-distance of the single units can be tailored, and also defects can be embedded in the desired location. These parameters influence the interstructural interaction and the metamaterial's refractive index, ranging from negative, to near-zero or positive values.

1.6   Metasurfaces

As a result of subwavelength fabrication techniques and functional materials integration, metamaterials and metasurfaces have opened up new ways for the realization of novel electromagnetic properties and functions[57]. As mentioned before, metamaterials need multiple layers of material to work efficiently, but they can produce many losses together with a challenging nanofabrication process. For this reason, the focus has been put on the manipulation of light by exploiting two-dimensional (2D) structures: metasurfaces. Metasurfaces are constituted of thin layers patterned with different, finite, elements of different shapes.

The metasurface working principle is based on diffraction. It can be explained starting from the Huygens-Fresnel principle (Figure 1.3), which affirms that each point of an optical wavefront can be seen as a spherical wavelet source, and the sum of all the secondary wavelets is giving the new wavefront. When a flat unstructured surface is hit and crossed by a light beam impinging normally, the wavefront shape and direction are not changed (Figure 1.3 A). On the other hand, when the substrate is a metasurface constituted of different optical antennas, each of them scatters the incident beam and creates a spherical secondary wavelet where the response
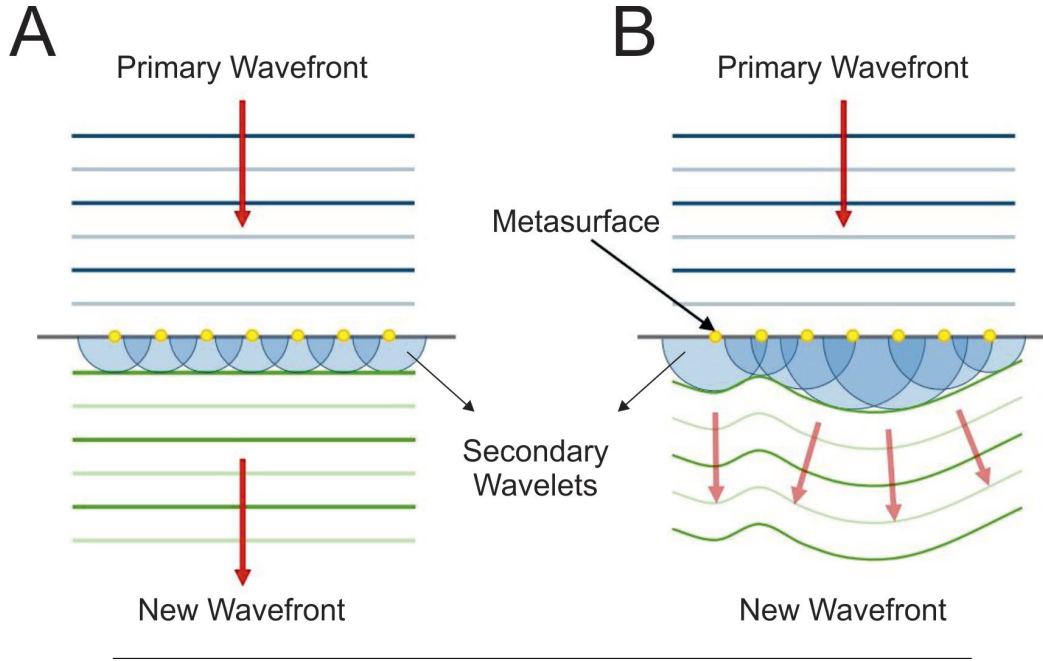
FIGURE 1.3: Schematic representation of the Huygens-Fresnel principle. Figure adapted from ref. [39]

is depending on the optical antenna characteristics. When these wavelets, having spatially-variated phase delays, interfere with each other, the output wavefront is modelled into the desired direction and shape (Figure 1.3 B). Metasurfaces can be divided into two main classes, based on the chosen material: plasmonic and dielectric metasurfaces.

1.6.1 Plasmonic metasurfaces

Plasmonic metasurfaces are metallic artificial structures where the underlying physical principle is governed by surface plasmon resonances. Thanks to the metal properties, when the optical antenna is subjected to an external field, the electrons present in the conduction band will be free to move from their original position, and energy to bring the system to equilibrium will be generated. If the applied electromagnetic field is an alternating one, the electrons in the conduction band will start to fluctuate around the central ions. This physical behavior of the electron is explained by the Lorentz oscillator model, where the amplitude of the shift owns a specific peak in the surrounding resonance frequency. Here, the observed shifts of the phase can reach π

values on the spectral resonance amplitude[118,14]. Moreover, as previously mentioned, plasmon resonances are sensitive to many changes like dielectric environment and geometry of the antennas[74].
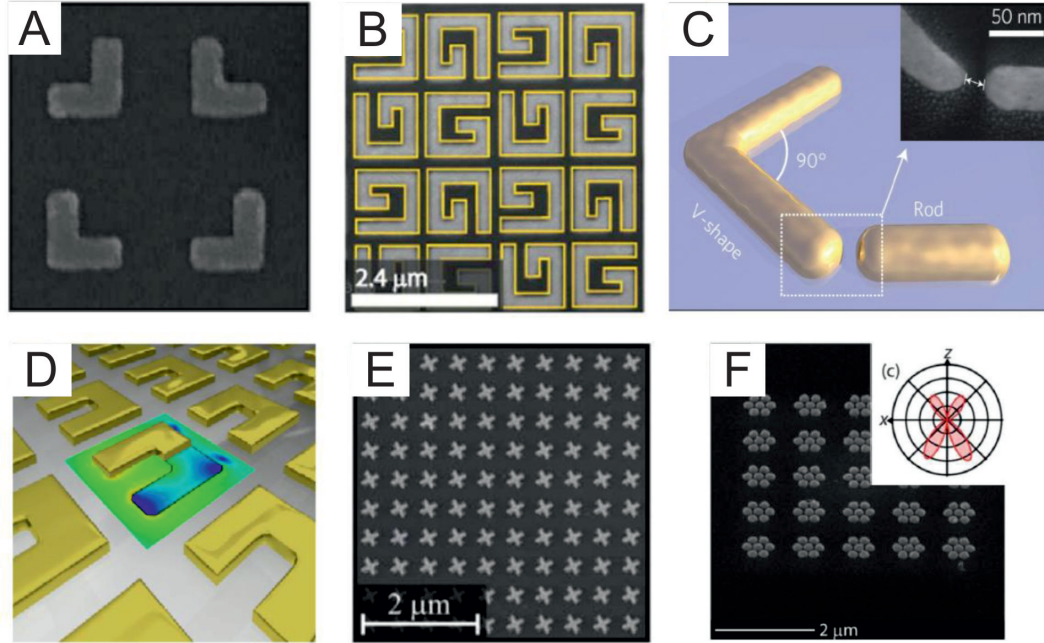
FIGURE 1.4: Examples of plasmonic metasurfaces. Examples of asymmetric and centrosymmetric plasmonic structures: (A) L-shaped nanoantennas, (B) G-shaped chiral structures, (C) multi-resonant antennas, (D) split-ring resonators, (E, F) centrosymmetric nanoantennas. Adapted from ref. [85].

The first artificial metasurfaces were based on localized surface plasmon resonances. Several examples of plasmonic metasurfaces are displayed in Figure 1.4, where the devices presented are covering different applications. The nanofabrication of identical nanoparticles allows having a collective behavior able to show a strong light-matter interaction producing specific resonant features. These patterned surfaces can have different applications, like light generation[16] or enhanced sensing[6]. Moreover, different healthcare applications are allowed by the possibility of simple integrability of these systems in downsized photonic devices[15]. Furthermore, thanks to the flexibility of engineering and periodic arrangement possibilities with accuracy up to the nano scale and subwavelength resolution, many more applications

were made possible: devices with amplitude, polarization, and phase optical control[100,180,181]; fabrication of lenses, beam steering, and holograms; superlens and cloaking devices able to tune the refractive index[141,4,95,112].

Despite plasmonic antennas showing many advantages thanks to their electromagnetic field localization and reduced dimensions, also problems have to be overcome due to the elevated absorption losses, mainly in the optical wavelength range, which are reducing the device efficiency.

1.6.2 Dielectric metasurfaces and Mie resonances

Even though optical wavefront control and sensing are interesting applications of plasmonic metasurfaces, these devices are essentially constrained by the plasmonic materials' inherent Ohmic losses. In the last ten years, a different platform based on low-loss dielectric has been developed for fabricating metasurfaces. The Mie scattering of subwavelength resonators is primarily responsible for the physics of optical resonances in dielectric metasurfaces[83]. When analyzing the scattering of particles showing similar wavelength, such as gold nanoparticles, in a homogeneous environment, such as water, while being excited by electromagnetic plane waves, Gustav Mie provided the solution to Maxwell's equations, which became known as the Mie solution[111,68].

For the last century, Mie scattering has served as the starting point for contemporary research on the rapidly emerging scattering phenomena in manufactured micro- and nanostructures. Mie resonances are effective electric and magnetic resonances that occur in the optical wavelength region and are found in dielectric resonators. Each Mie resonance's radiation pattern consists of a variety of multipoles with magnetic and electric components. Typically, one multipole dominates for subwavelength dielectric particles with simple geometries, and it controls whether the mode is magnetic or electric.
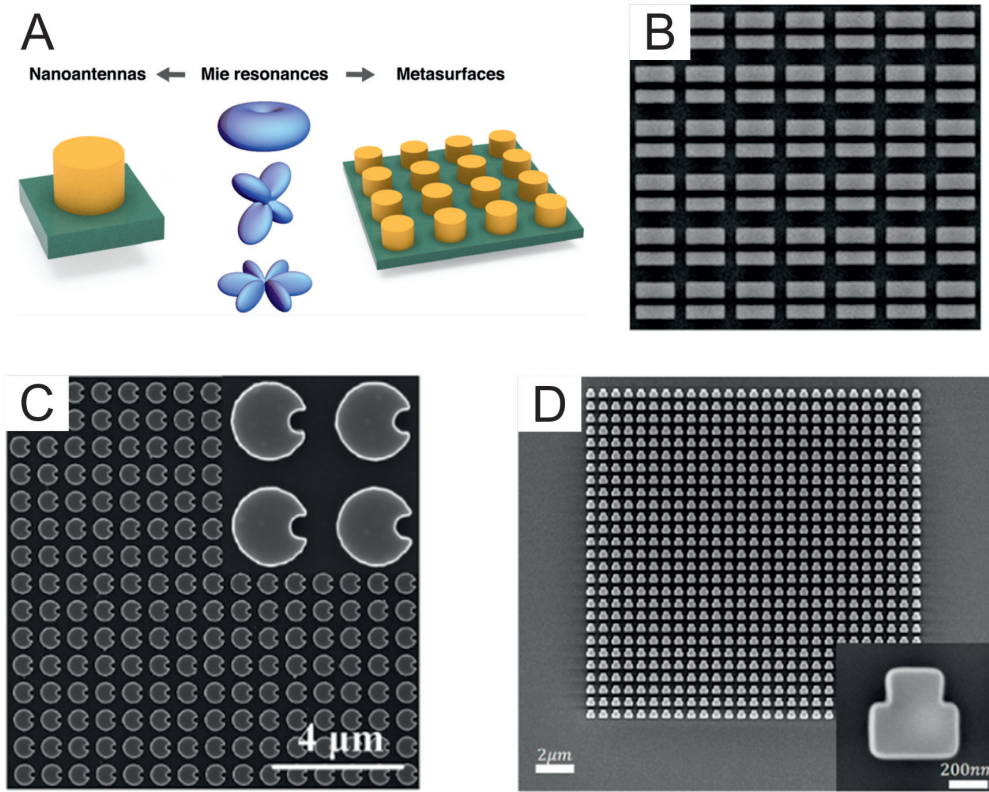
FIGURE 1.5: Dielectric metasurfaces and Mie resonances. (A) Sketch of Mie resonances in dielecric nanoantennas and metasurfaces. (B-D) Scanning electron micrograph of silicon metasurfaces where quasi-BICs are experimentally used. Images adapted from ref. [83].

In dielectric systems, Mie resonances are described as self-sustaining excitations owning resonant wavelengths that are comparable to the particle distinctive size d, which is linked to the refractive index of the particle as d $\sim \lambda/$n, where λ is the wavelength in the free space. To manufacture Mie resonances in the visible and near-IR spectral ranges, nanoscale meta-atoms need to have a high refractive index. Mie resonances, which employ non-radiating current settings and bound states in the continuum that can induce significant enhancements of local fields at the nanometer scale and are critically dependent on the system geometry, can be used to confine light in high-index dielectric systems[83]. When incident light with frequencies below or close to the band-gap frequency of the materials is used to excite regular dielectric resonators, such as spheres, cubes, cylindrical disks, and rods, both magnetic and electric dipole resonances originating from the oscillating displacement

currents are excited. This is in contrast to metallic resonators where the resonant modes are ruled by electric dipoles.

The magnetic dipole resonance is the lowest resonant mode, followed by the electric resonance[9,13]. The dimensions and construction of the resonators, together with their surroundings, influence the modes. Corresponding to the magnetic resonances in the context of metallic split-ring resonators[128], the magnetic Mie resonance has special circulating displacement currents[46,82,142] and produces the largest magnetic field enhancement in the resonator's center. This characteristic makes it possible to use a variety of unique light manipulation techniques that are difficult to implement with plasmonic metasurfaces, such as increased chiral sensing[146] and complete forward scattering employing Huygens metasurfaces[38,99]. By carefully adjusting the metasurface geometry and material selection, Mie-type resonances can be precisely controlled for a variety of target wavelengths, from ultraviolet (UV), visible[24], through infrared (IR)[137]. The design of metasurfaces for a wide range of applications, including sensing, diffraction-limited light focusing, polarization control, miniature spectroscopy, and holography, is greatly facilitated by this scalability[129,8,75,47].

Recently, experimental evidence of quasi-BICs in Si metasurfaces with high Q factor values for various meta-atom designs was presented[83]. Figure 1.5 (B-D) displays SEM images of three metasurfaces housing quasi-BICs that have high Q factors thanks to innovative radiative loss engineering and sophisticated electron-beam lithography methods. Applications for such metasurfaces include biosensing, nonlinear harmonic production, increased coupling to excitons in two-dimensional materials, and quantum effects. These applications all target high-Q resonances. Biosensors can be helpful for personalized care with frequent testing as well as screening to enable early identification of serious health disorders. Unfortunately, the commercially available biosensing techniques are time-consuming, expensive, and dependent on specialized individuals, trained lab staff, and intricate protocols.

1.7 Molecular Sensing

The field of molecular sensing, and especially biosensing, is developing a lot in the last years. The fusion of scientific disciplines like physics, engineering, chemistry, biology, and data science has led to the development of completely novel detection schemes and sensor functionalities. In order to embrace the fascinating range of growing technologies, sensor technologies for sensing all types of molecules utilizing various non-restrictive operation principles as "molecule sensing" or "chemical sensing" have recently been developed. Biosensors are a subset of sensors that use bioreceptors made of biological materials to bind target analytes, which are often biomolecules but can also be other chemicals.

1.7.1 Relevance of molecular sensing

Since molecular sensors and biosensors are useful on many levels, including assisting with the diagnosis of diseases, the characterization and development of medications, as well as the knowledge of both pathological and physiological processes, their significance and role are expanding in many industries.

The development of diagnostic instruments for point-of-care testing (POCT) is a significant area of research and investment that aims to address the serious health problems brought on by the various diseases[150]. For instance, POCT devices have been created for hepatitis B, malaria, tuberculosis, HIV, and Ebola[116]. Another pertinent example is POCT for Covid-19, which was used to create and distribute SARS-CoV-2 fast antigen testing, greatly aiding in the containment of the pandemic[183].

Molecule sensors can aid in the diagnosis of diseases as well as their treatment, for example, through advancing pharmaceutical research or therapeutic drug monitoring for doses adjustment[53]. Biosensors are employed in the development of biopharmaceutical products for the measurement of protein stability and activity as well as the discovery and characterization of new

drugs[179]. SPR biosensors, for instance, provide access to data such as a medication's binding kinetics, which is crucial for determining the drug's duration of action and clinical effect as well as discriminating between related pharmacological molecules[56,120]. Beyond diagnosis and treatment, biosensors can also provide an important contribution by advancing our knowledge of fundamental biological functions and disease causes[168,124].

Thus, it is evident that while molecular sensing and biosensing have already played a significant role in many sectors, there is still much opportunity for innovation and the demonstration of new sensor capabilities.

1.7.2 Molecular Sensing Working Principle

The mechanism of molecule/chemical sensing is made up of a number of components that when combined allow for the detection of signals brought on by the binding or even the simple presence of analytes (Figure 1.6). Samples containing the analytes can be buffer solutions or gases containing the analyte(s), or they can be complex such as saliva, blood, breath, fumes, or other fluids containing many distinct compounds.

For the purpose of increasing the concentration of the targeted analyte and making it easier to detect, certain sensors incorporate an initial amplification phase. An example would be biosensors designed to find microRNA (miRNA), which are tiny biomolecules with great diagnostic value because of their critical role in biological processes, such as the regulation of gene expression. These biosensors frequently amplify the quantity of miRNA analytes using polymerase chain reaction (PCR) techniques[76,72]. Amplification of the PCR is also playing a significant part in the identification and amplification of nucleic acids (DNA, RNA) to increase their concentration into a detectable range[157]. Other types of amplifications exist for other types of analytes, and are used by some sensors to amplify the signal impact of the targeted analyte. The binding of big nanoparticles to the analyte, for example, is used to increase its size or optical signal for improved detection[138].
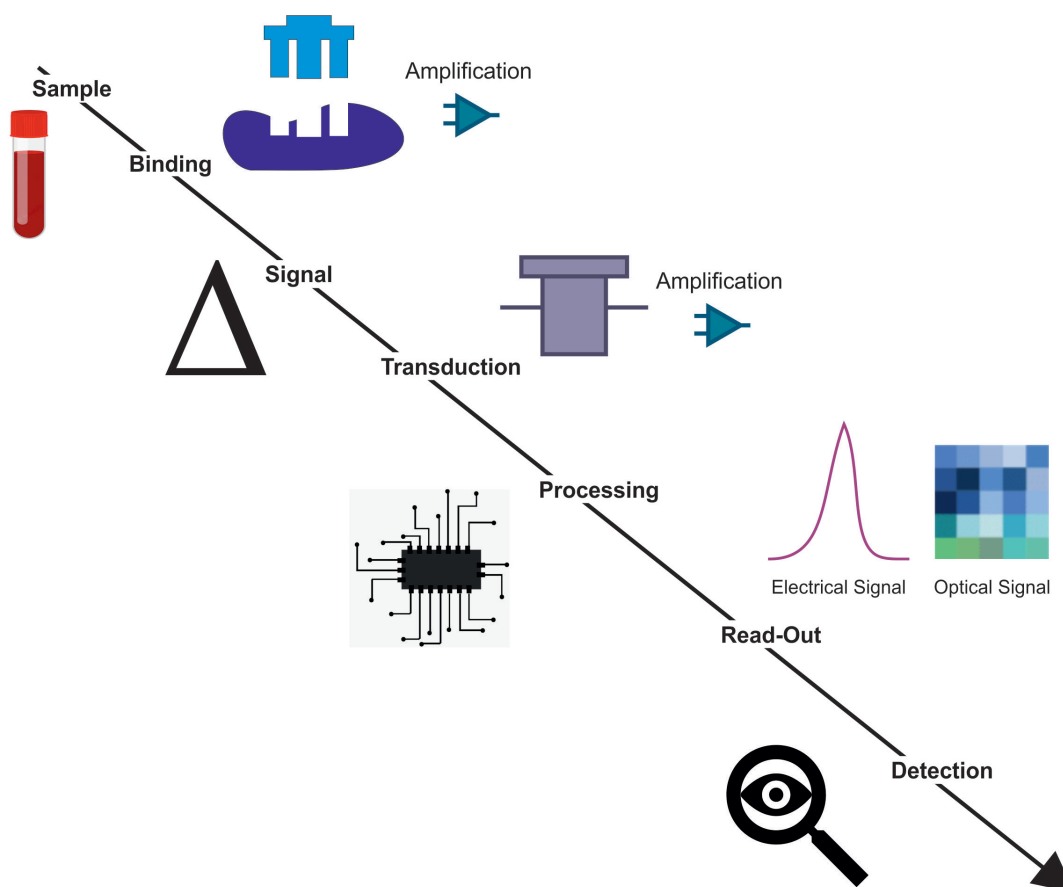
FIGURE 1.6: A general illustration of the components of the chemical/molecule sensing process. Biosensors are defined as sensors with a binding mechanism based on bio-receptors.

Binding the analyte prior detection is a very typical procedure for all sensor types, although it is not strictly necessary. Sensors using bio-receptors are referred to as biosensors. The binding typically happens via receptors tailored to a particular target analyte. Contrarily, some sensors, like electronic tongues and noses, combine non-specific receptors with variable degrees of affinity, causing analytes to produce a binding pattern that resembles a fingerprint and allowing for detection[52,19]. Without the need for receptors, binding can also take place, for example, through physisorption, as seen in the synthesis of lipid bilayers (SLBs) on silica surfaces[97,145] or the binding of DNA to graphene[69].

A change in a physical quantity, like as mass, light, temperature, or electrical charge, is the minimal requirement for molecule sensing. A transducer,

which transforms one form of energy into another to produce a quantifiable signal, is also a component of the majority of molecular sensors. Examples of transducer components include electrochemical, piezoelectric, and opto-electronic components[117]. It is interesting to note that while some sensors contain one or more transduction steps, some do not. Examples are the popular lateral flow pregnancy test and the quick SARS-CoV-2 antigen test, which allow users to observe the optical signal produced by binding[79].

1.7.3 Label-Free Sensing Method

Analytes frequently need to be labelled in traditional detection methods. In many traditional bioassays, a target analyte is first drawn from solution by an immobilized ligand, and then the interaction between the two molecules is examined using specific detection reagents. Bead-based flow cytometry and enzyme-linked immunosorbent assay (ELISA) are two examples of these techniques[93,64]. The effects of labelling on the biomolecules' structure and/or function can distort experimental results. They may have the ability to totally deactivate the biomolecule under study. Additionally, the label components' non-specific binding to other bioassay components may result in undesired background signal. When working with complicated materials like serum, plasma, or cell culture supernatants, this is extremely troublesome.

An appealing alternative to conventional label-based methods for quantifying molecular interactions is label-free quantification. Impedance- or optics-based biosensors are used in label-free technology (also known as label-free detection or label-free sensing) to assess the changes that take place when an analyte binds to a ligand immobilized on a biosensor surface[134]. This method eliminates the need to artificially manipulate the various assay components and allows for the real-time monitoring of the interaction.

Classic Sandwich Immunoassay (e.g. ELISA)
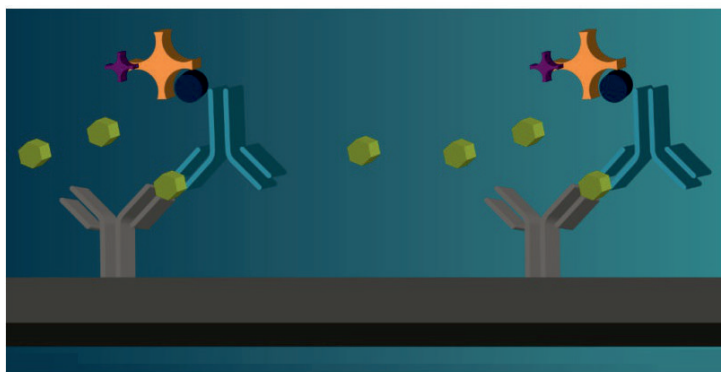
Label-Free Technology
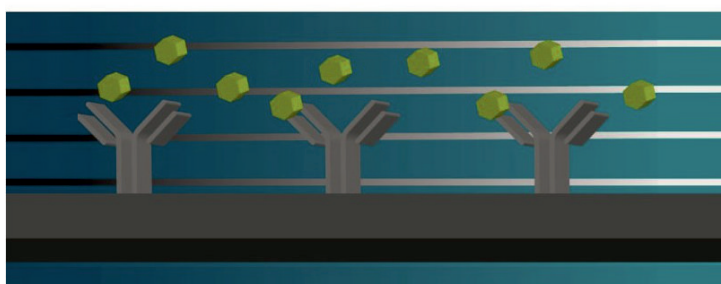
Fluorophore labeled streptavidin
Biotinylated detection antibody
Analyte
Capture antibody

FIGURE 1.7: Schematic of interaction analysis methods

Label-Free Interaction Analysis Advantages

In the direct investigation of natural molecules, label-free interaction analysis methods are employed. Since they do not rely on synthetic probes or labels to comprehend molecular interactions, they produce biologically pertinent data that is more likely to represent the behavior of these molecules in their natural state. This is essential for building a solid body of information that may be used to better understand structure–activity correlations, conduct central illness research, and find safe and effective treatments.

Importantly, label-free technology enables scientists to conduct studies that are just impossible with traditional approaches that only deliver end-point outcomes. The dynamic, real-time interaction analysis made possible by

label-free monitoring includes kinetic and affinity analyses as well as an assessment of binding specificity[121].

Conventional Methods for Label-Free Interaction Analysis

As already mentioned earlier, when examining physiological interactions between biomolecules, it is beneficial to employ a label-free, real-time monitoring system since labels might affect the biological process being studied. For instance, adding fluorescent dyes to analytes can change their natural behavior. SPR and QCM sensors are two of the most well-known label-free technology options:

- Surface Plasmon Resonance (SPR)[65], and

- Quartz Crystal Microbalance (QCM)[48].

In Figure 1.8, a schematic of their working principle is shown.

These methods are frequently employed to ascertain the affinities between various biomolecules since they are sensitive enough to detect monolayers of biomolecules in aqueous solutions[191].
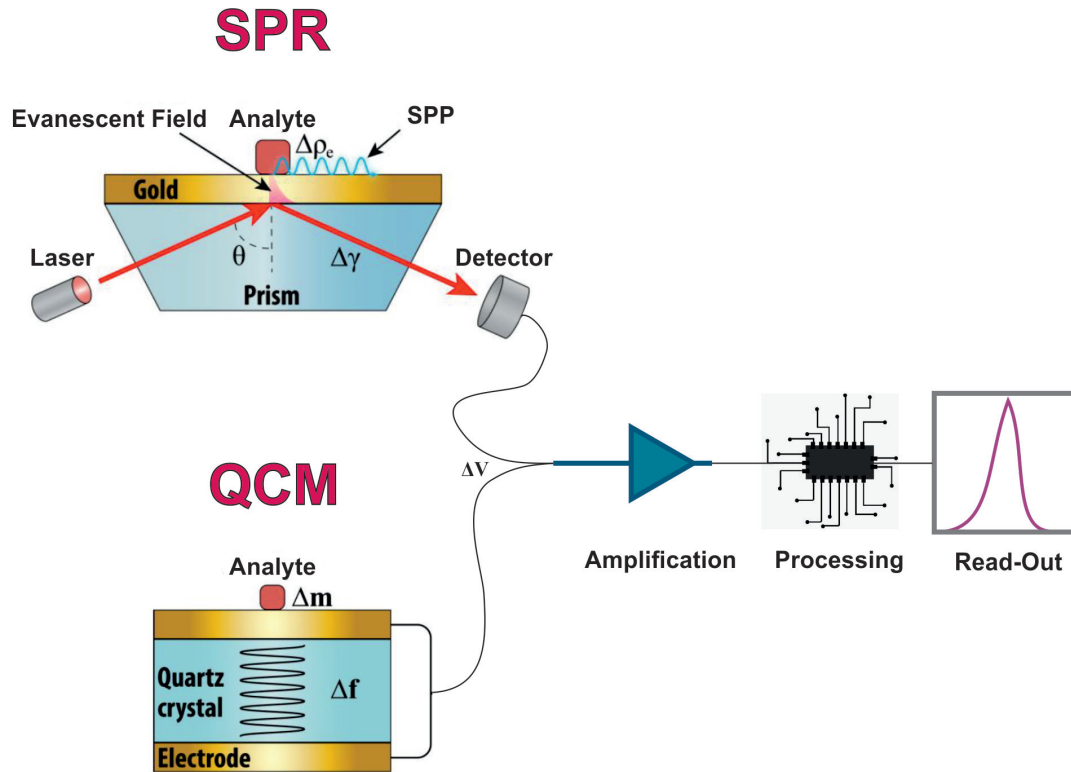
FIGURE 1.8: Schematics of SPR and QCM sensors operations.
SPR: Surface plasmon polaritons (SPPs) are excited on the gold
surface in contact with the sample media when a laser beam
impinges on a fine nanolayer of gold at the resonance angle θ
through a prism. Analytes at the surface will change the elec-
tron density $\Delta\rho_e$, which will change the resonance angle. Angle
scanning can be used to assess this resonance shift as a change
in light intensity at a constant angle or as a change in resonance
angle. A photodetector subsequently transforms this optical in-
put $\Delta\gamma$ into an electrical signal ΔV, which is then amplified,
processed, and read out—typically in the form of a sensorgram.
QCM: The piezoelectric effect is used to create an auditory reso-
nance between two electrodes and a quartz crystal. As analytes
attach to the surface, a change in mass Δm causes an alteration
in the acoustic resonance Δf, which is then further transformed
to an electric signal ΔV for amplification, processing, and read-
out through piezoelectric transduction.

1.8 Motivation and Outline of the Thesis

A new platform for controlling light using ultra-compact photonic device designs has emerged: metasurfaces. It is possible to modify the shape of the metasurface unit cell to provide optical functions as needed. Although metasurfaces have already shown a variety of capabilities, there is still work to be done (e.g., from the fabrication and upscaling point of view) before the technology is used widely and has commercial applications. This PhD dissertation demonstrates the creation of new metasurfaces and the methods used to create them for use in near-infrared applications. It focuses on the creation of dielectric metasurfaces and label-free sensing in the NIR region for the detection of aqueous and non-aqueous dielectric environments.

Here, the metasurfaces can deliver relevant near-field improvements, enhancing the molecules' absorbance signals by orders of magnitude. As a result, research of sub-monolayer systems and chemically precise detection of analytes at low concentrations are made possible by metasurface-based detection methods. It is also possible to design dielectric metasurfaces that cover a broad spectral range, up to the visible spectrum.

Tunable dielectric metasurfaces are demonstrated in this doctoral thesis, which show high-accuracy (<10 nm) nanostructures on transparent substrates, geometrically scaled in resonance behavior from the NIR to the visible wavelength range. However, it is extremely difficult to construct such nanophotonic devices using large-scale nanofabrication processes due to the restricted selection of appropriate materials.

Mid-IR metasurfaces have currently been manufactured using nanofabrication techniques that are not scalable, which results in the high cost of metasurface production. Therefore, a common and CMOS-compatible mid-IR metasurface manufacturing process flow is required to promote the diffusion of the technology for commercial applications. This thesis presents a method for wafer-scale metasurface manufacturing for mid- N-IR photonics

and sensing and has a significant emphasis on metasurface nanofabrication by exploiting, for example, nanoimprint lithography (NIL).

The thesis is divided into seven chapters.

Chapter 2 includes a brief overview of the metasurfaces concept, unit-cell design, and pattern choice. Tilted arrays of elliptical-shaped dielectric unit-cells will be designed and simulated.

In Chapter 3, the emphasis will be on the principle of metasurfaces, manufacturing, beginning with the many problems that must be addressed to construct such a device, and a brief description of electron-beam lithography (EBL) and nanoimprint lithography (NIL). Following that, a unique three-layer transfer technique based on EBL and NIL is described. The results for master fabrication, substrate preparation, NIL patterning, pattern transfer, metrology, and overall fabrication are provided. Finally, the chapter ends with a review and a brief overview of the many potential uses of this manufacturing approach.

In Chapter 4, a customised microscopy setup is introduced to measure the intensity changes of the manufactured metasurfaces. First, a brief overview of optical transmission spectroscopy is provided, as well as the general signal processing strategy that will be employed in the next chapters. Following that, a brief description of microfluidic devices that can incorporate metasurfaces is offered. The optical setup design is then presented, and system control is shown using commercially available software. Finally, the design and manufacture of a microfluidic chamber are demonstrated.

Chapter 5 provides an overview of the many techniques to tune dielectric metasurfaces, with a particular emphasis on the tunability afforded by geometrical variations and changes in the local environment refractive index.

Chapter 6 gives a general immobilization technique for structures exposing a sulfhydryl group (thiols) on silicon substrates, and contact-angle goniometric and XPS analyses were used to track the changes that are occurring on the

surface. After that, experimental streptavidin sensing is demonstrated utilizing arrays of silicon nanoellipse resonators coated with biotin using products that were readily accessible on the market. It experimentally demonstrates the potential of a nanoscale, all-dielectric platform for biosensing.

Last, Chapters 7 and 8 give a summary of the results of the previous chapters and an outlook to future applications.

Chapter 2

Metasurface Unit-Cell Design

2.1 Introduction

The remarkable range of applications enabled by metasurfaces is mostly due to the adaptability of its constituent parts. Devices with distinct capabilities can be created by carefully designing the constitutional units that spatially vary the phase shifts embodied by metasurfaces. In this short chapter, the focus will be on metasurfaces concept, unit-cell design, and pattern choice.

2.2 Elliptic Metasurface Unit-Cell Building Blocks

This doctoral thesis employed a metasurface design based on tilted arrays of elliptical-shaped dielectric unit-cells. The collective resonances are formed here by polarizing the electric dipole modes along the long axis of each individual unit-cell. The scattering loss, which is determined by the overlap of the field polarization and the scattering channels' mode profile, determines the resonance's linewidth in an ideal system. The zero-order plane waves that are moving normally serve as the scattering channels for the periodically tilted metasurface used in this study. The total electric dipole moment in each unit cell is then used to calculate the overlap between the plane wave and the mode profile. By carefully adjusting the unit cell shape, including the orientation angle θ of the single ellipses unit, the tilted design enables careful control of this overlap.
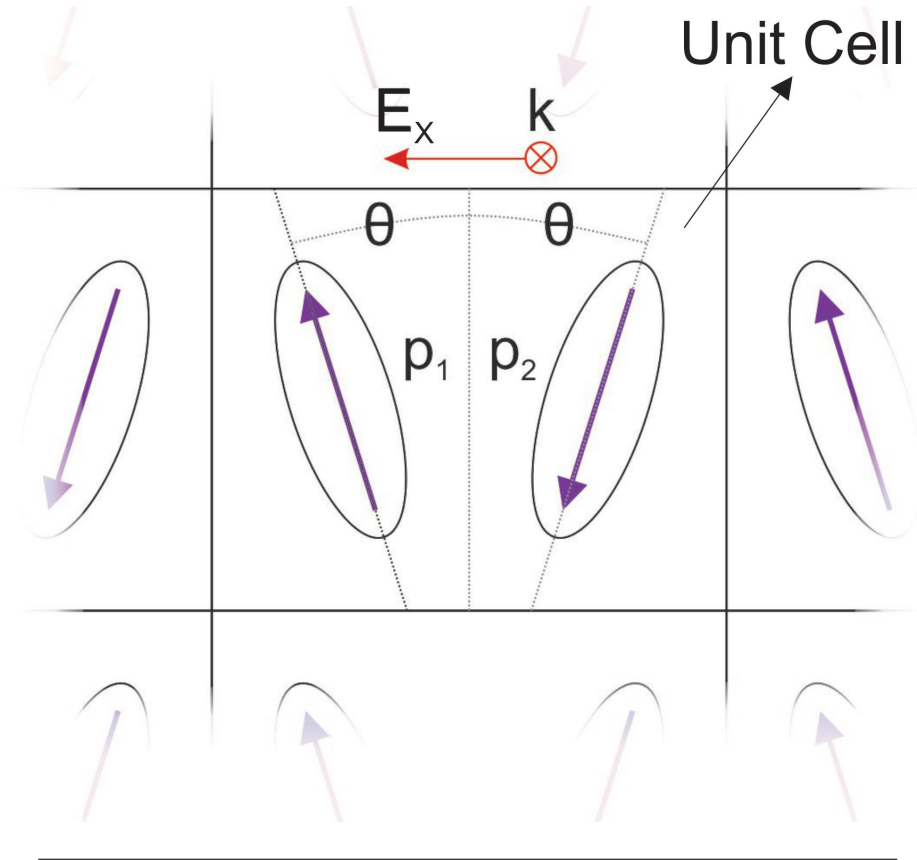
FIGURE 2.1: Collective dipole mode representation of the array
if excited with polarized light E_x.

During collective mode excitation, looking at the dipole moments, p, of the unit-cells, the dominant component, p_x, is actually perpendicular to the incident field polarization, E_x^0, as shown in Figure 2.1. On the other side, the parallel components are anti-symmetrically distributed ($p_{1,y} = -p_{2,y}$) which prevents out-coupling of light in the E_y-polarized plane wave. Thanks to that condition, the total scattering loss of the collective mode is substantially suppressed. Indeed, only the non-zero component is contributing to the scattering loss, which is the p_x component ($p_{1,x} = p_{2,x}$). In order to simplify the design simulation, it was assumed that the tilted array is located in a homogeneous background which is lossless.

In general, the scattered fields, both the forward, E^f, and the backward, E^b, can be described by the collective dipole resonance. The net, non-zero, dipole moment p_x can then be expressed as:

$$E^f = E_x^0 + \frac{i \cdot \omega \cdot z}{2 \cdot A} p_x;$$ (2.1)

$$E^b = \frac{i \cdot \omega \cdot z}{2 \cdot A} p_x;$$ (2.2)

where z is the wave impedance of the enclosing area, and A the unit cell area. Moreover, the net dipole moment, p_x, inside a unit cell can be expressed as

$$p_x = i \cdot 2 \cdot I \cdot p_{unit} \cdot \frac{sin\theta}{\omega};$$ (2.3)

where p_{unit} is the normalized dipole moment for a single unit-cell. I is the amplitude of the corresponding current, which is frequency-dependent and able to capture the resonant behavior. It can be expressed as:

$$I = \frac{E_x^0 \cdot p_{unit} \cdot sin\theta}{Z};$$ (2.4)

where Z is the total effective impedance of the unit-cell during collective resonance, which is including all the mutual interactions.

It is possible to approximate the effective impedance around a single resonance by using a RLC circuit:

$$Z = -i \cdot \omega \cdot L - \frac{1}{i \cdot \omega \cdot C} + R;$$ (2.5)

where R is the effective resistance and consists exclusively of the radiative loss.

To comply with energy conservation, it requires that:

$$|E_x^0|^2 = |E^f|^2 + |E^b|^2; \tag{2.6}$$

here, by substituting Eq. 2.1, 2.2, 2.3, and 2.4 in Eq. 2.6 and then using the following identity:

$$Re(Z^{-1}) = \frac{Re(Z^*)}{2 \cdot |Z|} = \frac{R}{2 \cdot |Z|}; \tag{2.7}$$

the relation between the effective resistance R and orientation angle θ results:

$$R = \frac{2 \cdot z \cdot p_{unit}^2 \cdot sin^2\theta}{A}. \tag{2.8}$$

Knowing the quality factor, which is given by $Q = R^{-1}\sqrt{L/C}$ (together with the capacitance C and the effective inductance L) and not substantially sensitive to small angles θ, it is expected that $Q \propto 1/sin^2\theta$. It looks like the quality factor remarkably grows upon decreasing angle θ. Realistically, the best attainable Q-factor is limited by different factors, like material losses and sample size. The chosen tilted design is able to provide an easy way to control the Q-factor, which can be applied simply to different unit-cells designs, not only elliptical ones. All these considered, associating the higher Q-factor with the lower orientation angle, it is possible to increase the resonators' sensitivity with respect to changes in the local environment, resulting in an improved fingerprint detection performances. Nevertheless, this high sensitivity makes the system more susceptible to small variations in the geometrical structures, which can be challenging from the fabrication point of view.

2.2.1 Unit-Cell simulation

In this work, an angle orientation of $\theta = 17.5°$ was chosen as a trade-off between sensitivity and fabrication challenges. Different from many geometries based on guide mode, where the electric field is mainly confined inside the high-index material, here the unit-cell-based collective dipole resonance is allowing a strong near-field enhancement at the unit-cell surface, which is an attractive characteristic for surface-based molecular sensing. To double check the design performance, the resonance behavior was simulated by a master student in an IBM/EPFL collaboration, Yashashwa Pandey, using the following geometrical parameters $A = 280$ nm, $B = 100$ nm, $P_x = 500$ nm, and $P_y = 410$ nm, where A and B are respectively the long and short axis of the ellipses, whereas P_x and P_y are the unit cell periodicity along the x and y axis. In the simulations, the structure height, H, and the orientation angle, θ, were fixed to $H = 100$ nm and $\theta = 17.5°$, respectively.
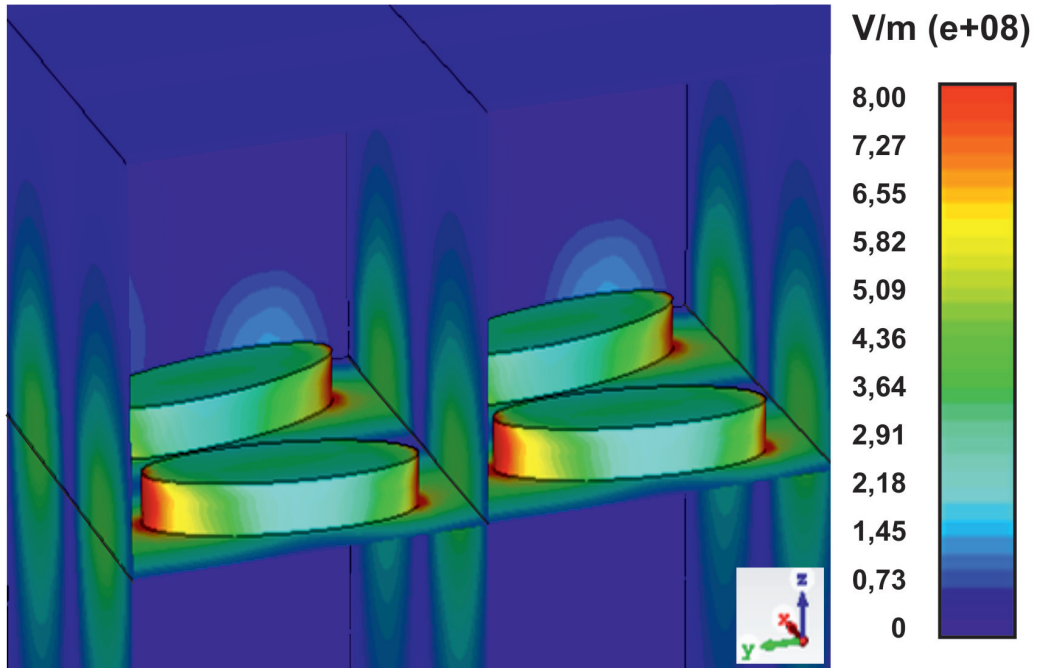

FIGURE 2.2: Simulated near-electric field intensity enhancement E measured at the resonance frequency with orientation angle $\theta = 17.5°$. Simulated by CST Studio Suite - Software for Electromagnetic Field Simulation.

Figure 2.2 shows the electric near-field enhancement distribution simulated with CST Studio Suite, which is a software for electromagnetic field simulation. Here a drastically enhanced electric near-fields distribution in between the unit-cells was found, with electric near-field intensity $|E|^2$ enhancements in the range of many broadly studied metal-based antennas used in practical applications[21].

Generally, in metallic resonators it is easier to obtain high-field confinements due to the huge contrast between the surrounding environment and the dielectric function of the metal. Nonetheless, the high-field localization comes at some cost, since the Q-factor is affected by the typical damping present in the metal. Also if higher field enhancements can be achieved by using, for example, metallic nano-gap antennas, where the gap-spacings are smaller than 10 nm[40], they are very challenging in fabrication, mainly due to the reliability and reproducibility issues, which are key points for practical sensing devices with reproducible features and characteristics.

2.3 Conclusions

The concept of metasurfaces, unit-cell design, and pattern selection are all briefly discussed in this chapter. Design and simulation work was done on tilted arrays of elliptical dielectric unit-cells. A significantly improved electric near-fields distribution between the unit cells was observed, with electric near-field intensity enhancements in the range of many extensively researched metal-based antennas used in practical applications. This allowed for to successfully demonstrate the response of the unit-cell.

The fabrication of the dielectric metasurfaces will be covered in the following chapter utilizing the design shown here.

Chapter 3

Fabrication

Sections of this chapter are adapted from one published article, which appeared in
Advanced Photonics Research (DOI: 10.1002/adpr.202200014) [126]

3.1 Introduction

As a result of their nanostructures, which have periodic, subwavelength
dimensions, metasurfaces show optical properties not present in nature.
However, fabrication on the nanometer scale is difficult since electron-beam
lithography cannot produce large-area metasurfaces due to its high fabrica-
tion cost and long exposure times. While other optical technologies like holo-
graphic lithography and plasmonic lithography can circumvent these prob-
lems, they are still constrained by the optical diffraction limit. Research is
being conducted on mechanical nanopatterning processes like nanoimprint
lithography (NIL) in order to solve this fundamental issue[119]. With NIL, it is
possible to achieve sufficiently high cost-efficiency and high patterning reso-
lution, independently to the diffraction limit. Adopting NIL for metasurface
fabrication is not straightforward but may lead to rapid deployment of meta-
surfaces.

In this chapter, the focus will be on metasurfaces concept, manufacturing,
starting from the different challenges to be overcome to fabricate such a de-
vice are analyzed and a short overview of electron-beam lithography (EBL)

and nanoimprint lithography (NIL) is given. Thereafter, a novel three-layer transfer process is described, which is a combination of EBL and NIL. Results are presented for master fabrication, substrate preparation, NIL patterning, pattern transfer, metrology, and overall fabrication. Finally, the chapter concludes with a summary and a brief outlook on different possible applications of this fabrication method.

3.2 Fabrication Challenges

As stated at the end of the previous section, the dielectric metasurfaces' performances are directly related to the reproducibility of the desired geometrical shapes, sizes, and optical properties of the chosen material. First of all, to start the metasurface nanofabrication, a proper substrate material has to be selected. It should be transparent, show negligible absorption and have a low refractive index. This last parameter is required to increase the contrast between the refractive index of the nanostructures and the substrate, and then to confine the electromagnetic field to the nanoresonator and avoid resonant mode leaking[7,58]. To work in the visible spectral range, quartz was chosen as substrate material, which has near-zero absorption losses, relatively low refractive index, good mechanical durability to support the metasurfaces, and makes them also cost-effective in terms of the material required.

While fabricating metasurfaces in the IR regime is still doable by UV photolithography[149], to scale down the structures' dimension in order to operate in the near-IR or even visible regime is challenging, since feature sizes below 10 nm are required. Furthermore, in addition to improving performance over the state-of-the-art technology, key to commercial success of new devices in general, and metasurfaces in particular, are scalability, cost efficiency, and high-throughput manufacturing capabilities.

The efficiency of operation for this type of device depends on the attained manufacturing accuracy. As described above, the geometric dimensions

should be controlled below the 10 nm level, ideally in all three dimensions, constituting very demanding fabrication requirements. It is possible to use several maskless direct writing techniques, such as direct laser writing (DLW), electron beam lithography (EBL), focused ion beam lithography (FIB), or scanning probe lithography (SPL) to create structures with feature sizes below 10 nm[154,22,155]. In addition, interference and extreme ultraviolet lithography can achieve similar feature sizes, with the disadvantage of using really expensive masks, not convenient for research purposes, and being limited in the achievable geometric shapes. Whereas DLW is limited in lateral resolution depending on the used wavelength, SPL can only pattern down to a depth of a few nms at such high resolution, which then requires an additional pattern transfer step to produce a higher topology. In return, FIB creates damage in target materials, including ion channeling effects, and has generally a rather slow patterning rate. Concerning EBL, the biggest challenges are proximity effects, as it will be discussed more in detail later.

Although each method offers specific advantages, a common aspect of all direct-writing techniques is their sequential processing, which limits the possibility to upscale to large areas or to a large number of samples, thus preventing mass fabrication applications and widespread use. The operating and manufacturing costs of EBL are generally high, even though efforts are underway to massively parallelize the EBL through the interaction of multiple beams[173], creating both physical and economic barriers. Considering average exposure times of tens of hours for a standard EBL system, even for quite small areas, the costs for a single sample can exceed thousand of dollars in realistic calculations.

In addition to the long EBL exposure times, the interactions of the electrons with the resist and the substrate cause so-called electron proximity effects, which lead to a deviation of the resist structures exposed and developed from the initial design[130].

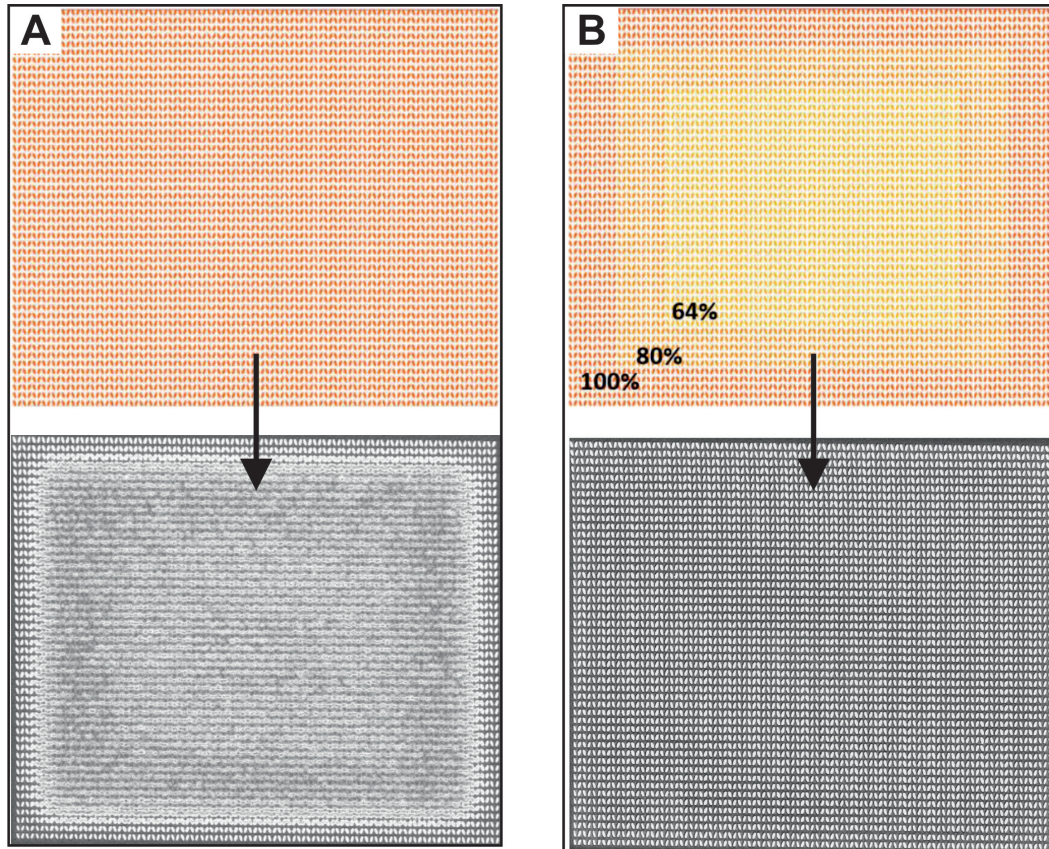Although proximity correction algorithms based on point-spread functions

FIGURE 3.1: Example of dose tests on two types of arrays, one without any consideration of proximity effects (A), and one with consideration of proximity effects (B). In the latter case, the dose was reduced when moving from periphery to the center of the array by 20% in two discrete steps.

or similar models are at the heart of modern EBL data preparation[114,167], transparent and non-conductive substrates, as mainly used for transmission optics, are still difficult to manage because the charge carriers are not drained and can accumulate unevenly depending on the density of the structure, the stack, the intensity, etc. To overcome the proximity effects on non-conductive substrates, it is necessary to write labor-intensive empirical test structures for a stack with additional charge drainage layers before the design can be properly exposed, once again contributing to high overall costs.

An example of correction of the proximity effect can be seen in Figure 3.1. Here, the orange arrays on the top represent the design, while the two at the bottom represent the final results. Figure 3.1 A shows an example of a

non-optimized manufacturing procedure, while the final optimized result is shown on the right (B). The final pattern was obtained after various iterations in both design and dose tests. In the following section, a deeper insight into EBL will be given.

3.3 Electron Beam Lithography

Lithography is the most commonly used technique to create a precise shape of designed resonators, which is why the majority of the metasurfaces are fabricated using electron beam lithography (EBL) methods. In EBL, to write the desired, customized shapes, a focused electron beam is scanned over an electron-sensitive polymer film, called EBL-resist, which is previously coated onto the metasurface material. When the electrons interact with the resist, they can either crosslink or break the polymer bonds, changing the solubility in the developer of the resist. Then, after exposure, a latent pattern appears in the resist, which can then be selectively dissolved to provide patterned access to the underlying substrate on the metasurface material. Following development, the surface-formed resist patterns can be used as an etch mask or lift-off layer. A schematic of the different process possibilities is shown in Figure 3.2. In the project here described, to transfer the final patterns into the metasurface material, first, a dry plasma etching process is performed, followed by an oxygen plasma treatment to remove the residual resist.

The advantage of EBL is that it can achieve a spatial resolution of less than 10 nm without the need of photolithographic masks. Therefore, it is an excellent method for rapid prototyping of metasurfaces and represents the standard method for making nanophotonic devices for research purposes.

Figure 3.3 A shows a wavefront shaping metasurface made by EBL, which operates up to the deep ultraviolet (DUV) spectral region[186]. Here, the EBL method allows for reproducibly fabricating nanoantennas ranging from 50 nm to 160 nm in size. Another example of nanoantennas made by EBL is shown in Figure 3.3 B, which consists of Si dimer resonators with a gap size
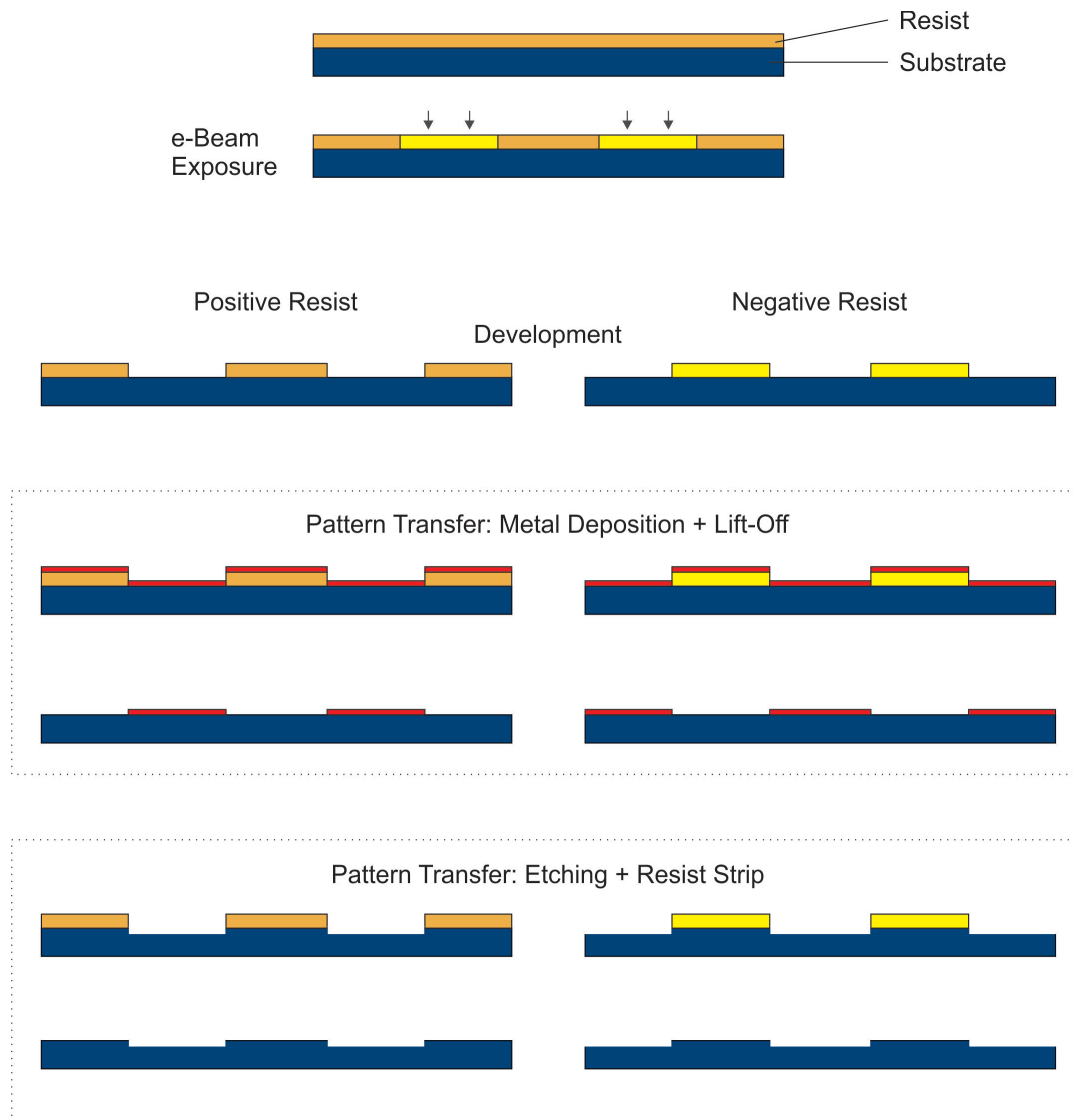
FIGURE 3.2: Schematic of EBL approaches for positive and negative resists, and pattern transfer processes: metal deposition & lift-off, and etching & resist strip.
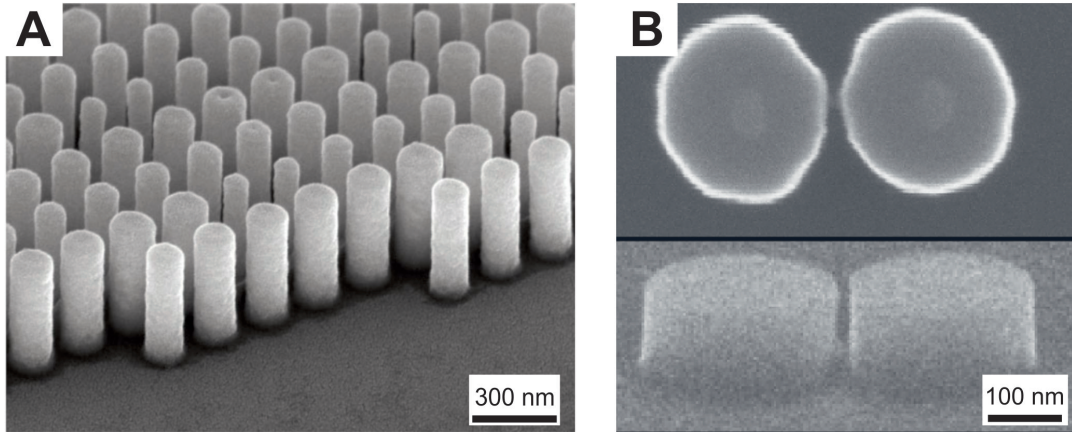
FIGURE 3.3: Metasurface nanofabrication methods: (A) SEM image of EBL fabricated metasurfaces operating in the UV spectral range. Adapted from ref. [186]. (B) SEM image of Si unit-cells fabricated with EBL, with a gap size of 20 nm. Adapted from ref. [23].

of 20 nm[23]. Si dimer structures can confine light to the nanogap, providing strong signal amplification for surface-enhanced Raman spectroscopy applications.

EBL is a powerful method to fabricate advanced metasurfaces with nanoscale resolution. However, as it was mentioned in the previous section, it is limited by its writing speed, which is about 1 mm per hour depending on the spatial resolution and the size of the electron beam and moreover, it is not possible to increase the speed of nanofabrication with EBL methods. Therefore, electron beam lithography is not an optimal fabrication route for large area nanofabrication and mass production of metasurfaces.

3.4 Nanoimprint Lithography

As previously mentioned, in the event that identical nanostructures are needed either in various positions on the same target wafer or on multiple target wafers, an attractive method of fabricating structures more economically than by EBL alone (or any other direct writing nanostructuring method) is nanoimprint lithography (NIL)[136]. Based on seminal work performed in

the 1990s[34,33], NIL is based on the transfer of a master structure to a target substrate by imprinting. This process is repeatable and large areas can be patterned by step-and-repeat routines.

More specifically, NIL uses mechanical steps to fabricate nanostructures, leading to various types of NIL processes. Generally, a rigid mold with nanopatterns, called master, is pressed with constant force into a resin made from a polymer material to transfer nanopatterns to the resin. It is important to notice that the fabrication of nanoimprint stamp is often performed by EBL, which is the approach followed in this work, as described in detail in the Results section, 3.6.2 subsection.
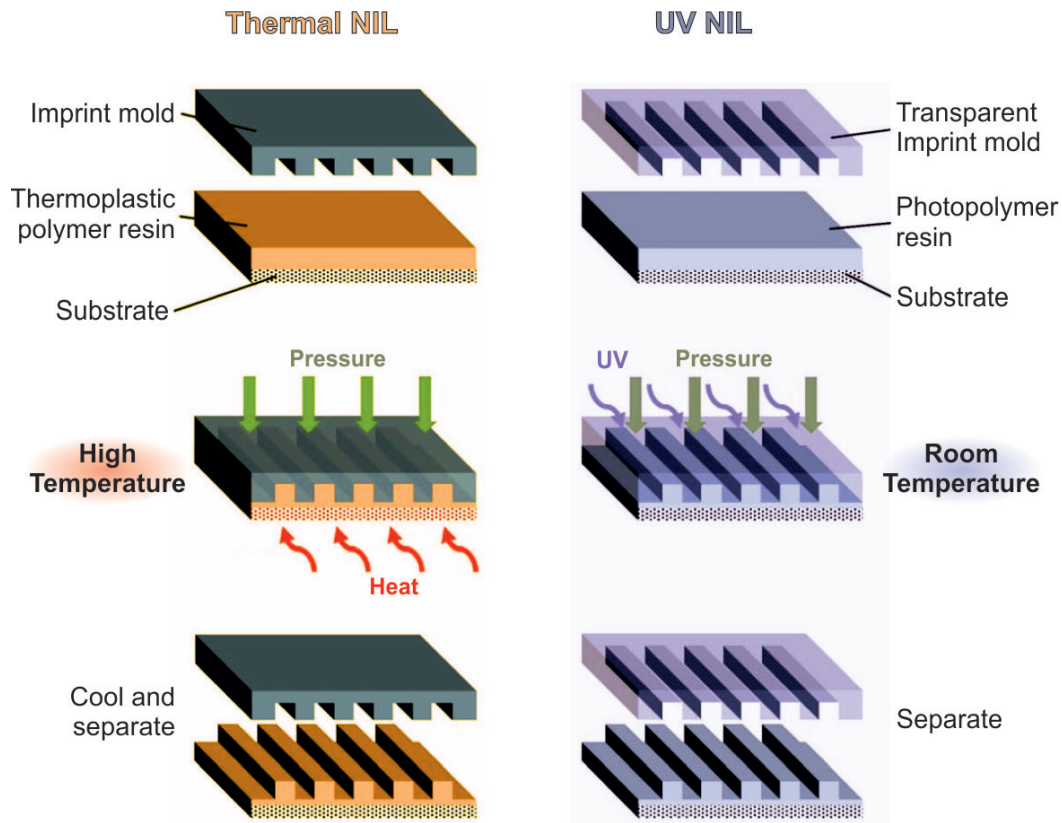

FIGURE 3.4: Schematics of thermal NIL (left) and ultraviolet (UV) NIL (right). Adapted from [119].

Thermal and ultraviolet (UV) NIL are the two widely used conventional NIL techniques. A schematic representation of these processes can be seen in Figure 3.4. In thermal NIL, heat is used to cure and harden a thermoplastic polymer resin. Some examples of thermal NIL being employed to increase the resolution of NIL below 25 nm are presented in Figure 3.5[31,33,32]. UV NIL, on the other hand, solidifies the resin using ultraviolet light. Due to the minimal system requirements, quick response times, and lack of a heat source or thermal conductance, it often has higher productivity[61]. The outcomes of using UV NIL to create 5 nm nanopatterns and 5 nm gap Au nanopatterns by the lift-off method[11] are shown in Figure 3.5 C-E. Additionally, the NIL procedure can be utilized to create consistent nanopatterns on a variety of surfaces using so-called soft NIL approaches[125], which employ flexible molds made of polymeric materials like polydimethylsiloxane (PDMS).

In general, nanoimprint lithography enables mass-production of metasurfaces with a resolution comparable to the EBL, as it replicates the masters on the nm-scale. Although various wafer-scale nanofabrication methods have been used to realize metasurfaces, due to the type of materials to be used to obtain the suitable optical properties in the visible / near-infrared, it remains highly challenging to realize metasurfaces with high throughput without detrimentally affecting the underlying layers during the etching steps, which can eventually change the output fabrication results in an unpredictable way. For these reasons, there is a need for a cost-effective and high-throughput nanofabrication method to efficiently fabricate mid-IR metasurfaces.

3.5   Three-Layer Transfer Process by EBL and NIL

To solve up-scaling hurdles of EBL, a combination of EBL and NIL was implemented. Hereafter, a comparison between the standard NIL process and a novel three-layer transfer process is presented[42].

As can be observed in Figure 3.6 A, a light-transparent mold was made from
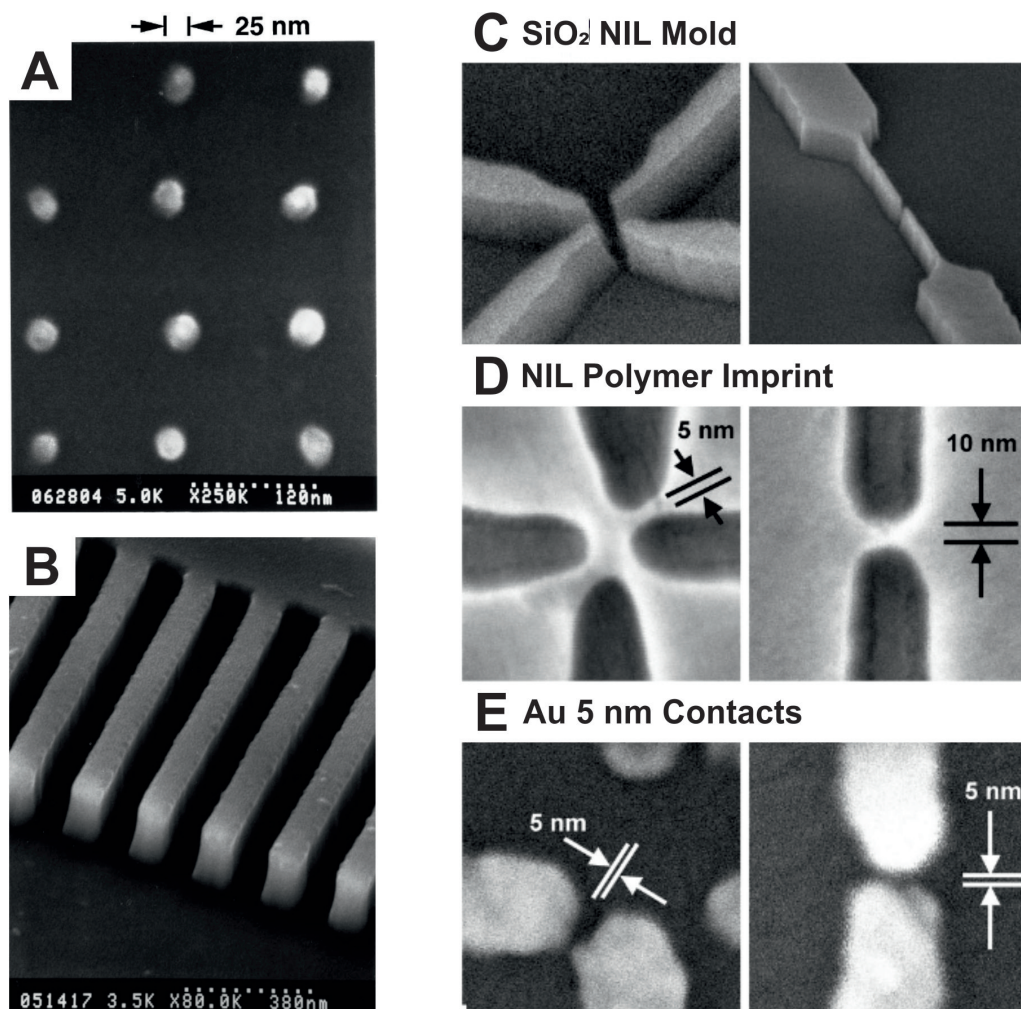
FIGURE 3.5: Scanning electron microscope (SEM) images of metal dots of 25 nm in diameter and a periodicity of 120 nm manufactured by thermal NIL (A) and strips 70 nm wide and 200 nm high on the left panel[31]. SEM images of a mold of silicon oxide (C), resin imprinted after UV NIL (D), and Au contacts after metal evaporation and resist liftoff, showing a resolution of 5 nm UV NIL used to contact single molecules (E) on the right panel[11].

A Nanoimprint Lithography (simplified Processing Steps)

Pressure / UV light / Temperature

NIL resist
Semiconductor
Substrate

B Direct Patterning using Si-based NIL Resists

Critical dimension — NIL resist
Semiconductor
Substrate

Non-selective removal — Critical dimension

Critical dimension

C Indirect Patterning using Si-based NIL Resists

Etching 1

Critical dimension — NIL resist
Layer T
Layer P
Layer S
Substrate

Selective removal

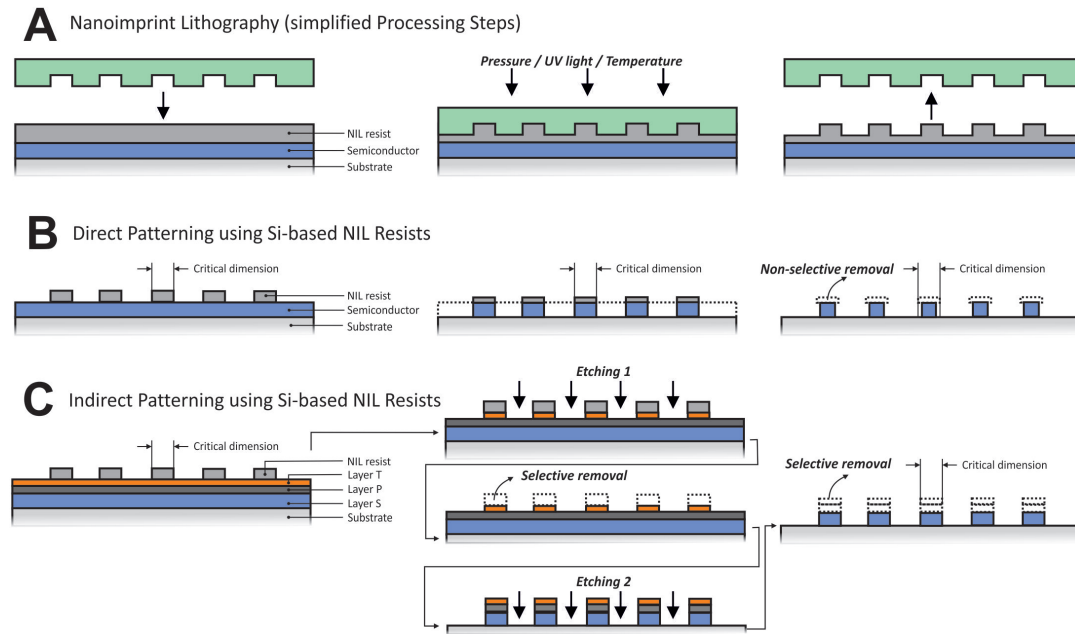*Selective removal* — Critical dimension

Etching 2

FIGURE 3.6: (A) Schematics of the processing steps in nanoimprint lithography (NIL) using a stamp (fabricated by a master by molding; not shown here) to pattern the NIL resist coated substrate. When the stamp gets in contact with the NIL resist, depending on the fluidic properties and size of the structures, external pressure and capillary forces drive the filling process of the stamp structures. The transformation of the resist from liquid phase to solid phase can be achieved by ultraviolet (UV) light or temperature, or a combination thereof. The residual layer is removed by non-selective etching (not shown here). (B) Direct transfer of NIL patterned resist structures into a semiconductor layer with inevitable reductions in feature size and structure height, as well as surface roughening due to non-selective removal of NIL resist. (C) Indirect transfer using a three-layer system; etching of a transfer layer, selective removal of the NIL resist without affecting the protective and buried layers, opening of the protective layer, and final etching of the semiconductor layer with subsequent selective removal of the protective layer (without affecting the semiconductor layer). Compared to (B), more accurate dimensions can be maintained as no reductions in feature size and height occur as a result of non-selective removal of the NIL resist. Furthermore, being protected, surfaces and morphologies can be kept clean and free of defects.

an EBL pre-fabricated Si master (as will be described later in details 3.6.2) using a UV-curable working stamp resin (EVG UV-NIL AS) on a flexible backplane. This type of process is called SmartNIL® technology and is performed by external partners (EVG). Here, the target substrate is coated with a photosensitive, acrylic imprint resist and contacted at low pressure with the still liquid resist. Thanks to capillary forces, the stamp structures are filled with resist. In this way, the resist conforms with the topology of the mold (Figure 3.6 A, middle panel). The liquid resist is then cured upon exposure to UV light through the transparent mold, thereby cross-linking the resist and yielding a uniform, rigid polymer network. After the resist is cross-linked, the mold can be removed (Figure 3.6 A, right panel), leaving behind the negative topology of the working stamp in the resist. The target substrate can be further processed by a direct pattern transfer (Figure 3.6 B), based on an etching step with the NIL resist acting as etch mask (Figure 3.6 B, middle panel). For many material classes, the residual NIL resist can then be selectively removed without affecting the target material, obtaining the final structures (Figure 3.6 B, right panel).

For the emerging class of fully dielectric metasurfaces, the conventional NIL as described above has been deployed for the fabrication of perovskite nanometer gratings and nanohole arrays[105], Si_xN_y gratings of width less than 100 nm[173], epitaxial α-quartz nanopillars[189] or poly-Si metalenses[91], mostly manufactured under high productivity conditions as recently reviewed[119]. If the material to be patterned consists of Si, for example, silicon-on-insulator[161] or silicon-on-glass, however, the conventional processing path can no longer be used without detrimentally affecting the semiconductor layer as the latter will be removed simultaneously or at least severely attacked by the cleaning agents (e.g., SF_6). Consequently, a direct pattern transfer (Figure 3.6 B) is not directly applicable to dielectric metasurfaces. Whereas some uniform reductions in feature size can potentially be addressed through labor-intensive design and efforts, a generic process is desirable. Before proposing such a processing path, it should be noted that

the master used for molding can be made of any material that allows replication to a working stamp. This also includes high conductivity substrates that enable high-resolution EBLs without causing severe proximity effects.

Motivated by the excellent scalability, resolution, and cost offered by NIL, a new processing route[42] is proposed that enables high-performance NIL resists with low etching selectivity to semiconductors yet to be used for patterning amorphous, microcrystalline, or crystalline semiconductors. The process is adapted from the production of complementary metal oxide semiconductors (CMOS) and is based on a three-layer system. This stack consists of the NIL layer, a transfer layer, and a protective layer on top of the semiconductor. The processing concept has different steps; first, the patterned NIL layer is transferred into the transfer layer, subsequently allowing selective removal of the NIL resist thanks to the protection of the semiconductor by the protective layer. The transfer layer will act as a rigid mask to structure the protective layer. Finally, the protective and transfer layers are used to pattern the semiconductor before selectively removing them. As a result, the semiconductor surface is completely cleaned and the lateral dimensions are not affected by non-selective etching.

The concept of selective etching becomes evident if illustrated with an example of its implementation; the protective layer can be composed of Al_xO_y, while the transfer layer can be SiO_2. The removal of the NIL layer is then performed by means of SF_6 oxygen plasma (Figure 3.6 C, central panel) followed by cleaning under rather harsh conditions, applicable since the semiconductor is fully protected. The transfer into the semiconductor is then performed by inductively coupled plasma reactive ion etching (ICP-RIE) (Figure 3.6 C, center panel) using a combination of the protective and transfer layers or just the protective layer alone - after the transfer layer has been removed. In principle, the generic process described can be used to transfer any nano-pattern, created with non-scalable and sequential lithographic methods, to large areas and real-world applications using step-and-repeat approaches of NIL and the three-layer concept. In particular, other material stacks composed of transfer,

protective, and target layers other than those described above can be structured in a very similar way using modified processing parameters or even different tools.

3.6   Results

The results of the three-layer process with combined EBL and NIL described before in Section 3.5 will be presented for dielectric metasurfaces compared to state-of-the-art direct patterning by the fabrication of all-dielectric metasurfaces based on amorphous Si on a transparent quartz substrate, using the structures described in Section 2.2. As a test system, pairs of tilted ellipses were chosen (Figure 3.8; inclination angle ϕ = 35 °) as *i)* they demonstrate very narrow and highly tunable absorption characteristics in the near-infrared (NIR) regime[98,176] and *ii)* ellipses are challenging and therefore geometrically benchmarking objects for any patterning technique besides simple dots[147], gratings[108] or rings[171,89]. In these ellipses, which make up an array of nanoantennas, incident light excites magnetic and electrical resonances so-called Mie resonances - which result in discrete peaks in the absorption spectrum with high extinction coefficients.

High irradiation efficiency and low heat conversion are observed due to the low absorption loss of the dielectric material. Since sub-wavelength dielectric resonators can support bound states in the continuum, light is strongly confined and, as a result, narrow resonances ($<$ 10 nm full width at half maximum - FWHM) show up. Their resonance frequencies depend on the specific geometry, the constituent material, and dielectric environment[81] which makes them interesting sensing elements with tunable spectral responses by design. Due to moderate filling factors, ellipse arrays reveal smaller extinction coefficients than high-density, sub-wavelength metasurface gratings[174]. The smallest deviations from the desired geometry, now, will be directly visible in the acquired optical spectra, rendering these structures ideal to demonstrate the accuracy of the fabrication.

3.6.1 Scaling Over a Large Spectral Range

To show the advantages of the novel fabrication approach, the aim was to miniaturize the geometries from the previously reported NIR[153] to the visible wavelength regime using the linear scaling law of the unit cell and the dimensions of the ellipses (Figure 3.7 A). Figure 3.7 B illustrates the scaling factors S ranging from 0.85 to 1.20 with $S = 1.00$ having $a = 280$ nm and $b = 100$ nm, respectively (Figure 3.7 A). The height h of the a-Si was kept constant at 100 nm, and the angle between the ellipses, ϕ, was not changed. Figure 3.7 C shows a sketch of the final ellipses arranged in to an array.
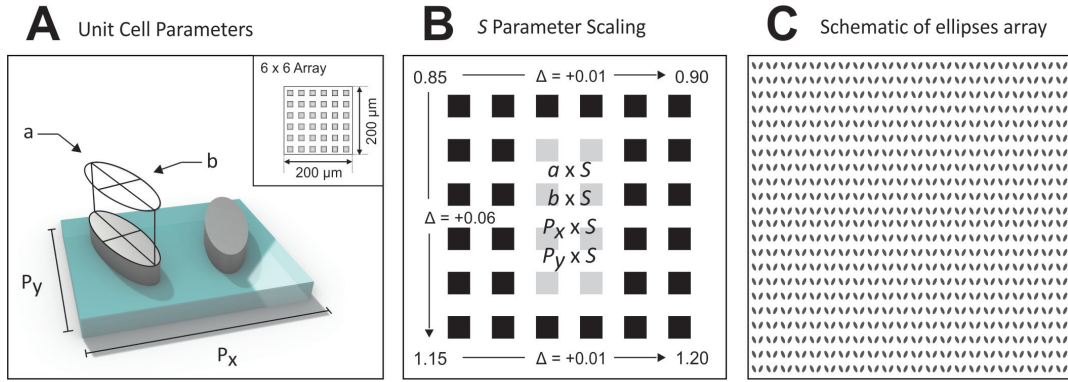

FIGURE 3.7: (A) Design of the unit cell of dimension p_x and p_y with a single pair of ellipses with long and short axes, a, and b, inclined by an angle ϕ. In the top-right inset, the upscaling of single-pair ellipses into identical 6 x 6 arrays is shown. (B) Uniform scaling of the dimensions of all ellipses and unit cell sizes by the scaling parameter S, aiming for an absorption resonance range from the NIR ($S > 1.1$) towards the visible range ($S < 1.0$). (C) Schematic of ellipses fabricated for $S = 1.00$ (with $a = 280$ nm, $b = 100$ nm, and $h = 100$ nm) on a transparent quartz substrate.

3.6.2 Master Fabrication

For EBL, pairs of inclined ellipses with nanoscale dimensions further represent a challenge as the pattern generator must operate non-parallel to the beam's two primary axes of deflection. In this work, the ellipses were exposed using "sequences", which is a shape generation mode of the Raith

EBPG5200 EBL system with an acceleration voltage of 100 kV and operating under ultra-silent conditions. The sequence is defined as a series of lines and jumps. It was taken advantage of this mode to place shots with sub-field resolution accuracy (0.5 nm). The ellipses were exposed using sub-field resolution units for placing the exels (exposure elements). With this mode, it was possible to achieve the maximum exel shot positioning accuracy for these non-orthogonal shapes. The filling of the ellipse was carried out starting from the circumference and ending at the center, following a spiral path. The writing order was from ellipse to ellipse along the entire pattern to reduce the effects of thermal drift (see arrows in Figures 3.8 C and D).
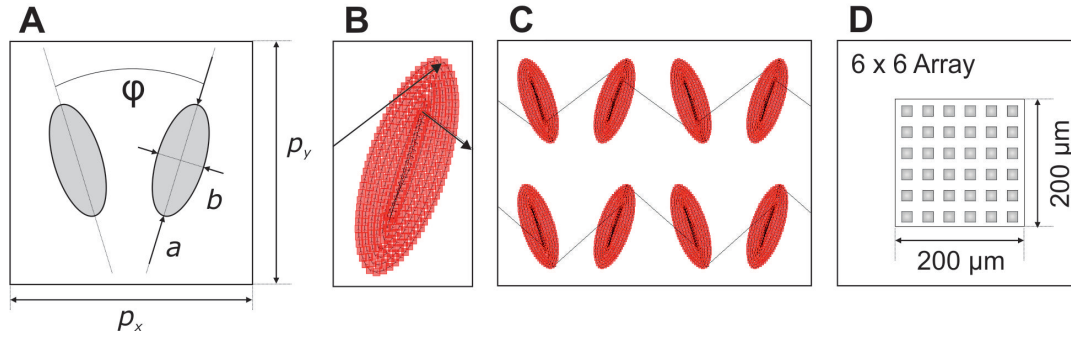

FIGURE 3.8: Design and EBL exposure elements. Design of the unit cell (A) of size p_x and p_y with a single pair of ellipses with long, a, and short, b, axes, being tilted by an angle ϕ. Ellipse filling (B) by EBL exposure elements starting from the edges and finishing at the centre in a spiral path. Upscaling of single-pair ellipses to identical 6 x 6 arrays (C).

The base dose used for exposing the patterns on the Si substrates was 7500 μC /cm^2. Patterns with 12 nA and 50 nA were exposed to accelerate the exposure, but there were no notable differences between the two in respect to ellipse dimensions after pattern transfer.

A schematic of the process flow can be observed in Figure 3.9. More specifically, it was used HSQ 4% resist two-step spin-coating with 90 nm thickness, without adhesion promoter. Prior to coating, the silicon wafer was cleaned with oxygen plasma, soaked in surpass 3000, and baked at around 150° to completely dehydrate the surface. The development was performed with the

standard process: AZ351B : H_2O = 1 : 3 for 5 min. Subsequently, quenching with water was performed by adding 8 volumes of water in the developer and then rinsing it in acetone and IPA. At the end, the sample was blow dry with N_2. For proximity effect correction (PEC), a point spread function for the corresponding stack was used.
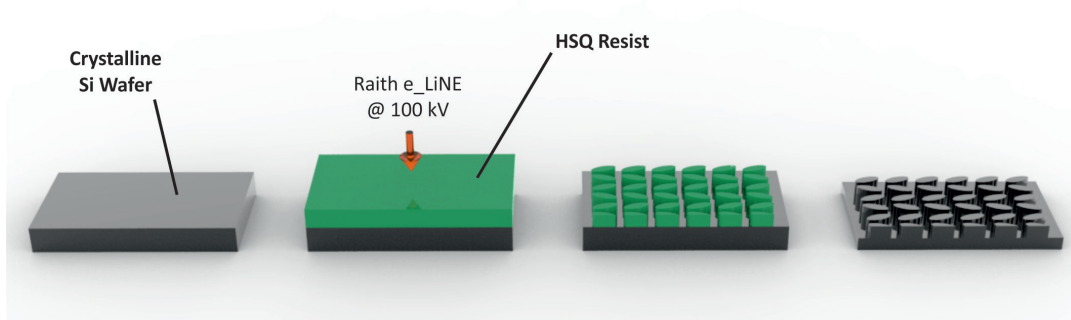

FIGURE 3.9: Schematics of the fabrication process flow for the Si Master.

Scanning electron microscope (SEM) was used to inspect the sample prior to etching. Once the design looked acceptable, the etching process was initiated. As a first step, ICP-RIE was performed for 1 minute using HBr etching at 80 W and radiofrequency plasma RF at 800 W. After cleaning the wafer with 600 W oxygen plasma ashing for 5 minutes, the sample was immersed in BHF for 10 seconds, washed in DI water, and dried with N_2.
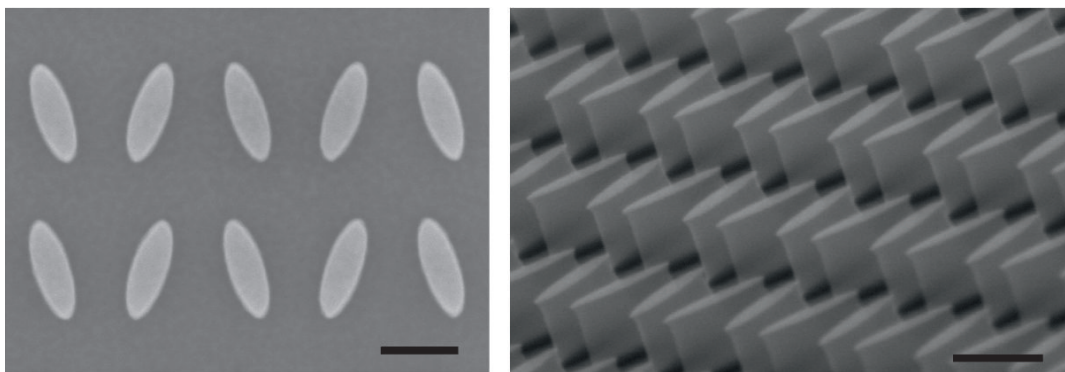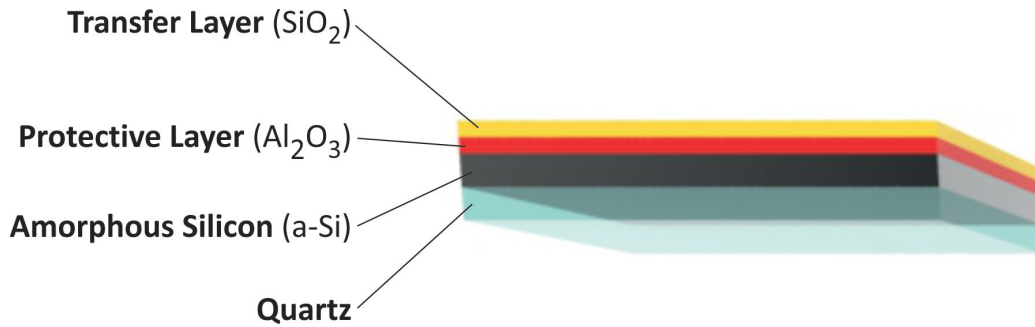

FIGURE 3.10: Scanning electron microscope (SEM) images of the final master from top (left panel) and tilted (right panel) view. Scale bar in both images: 200 nm.

Once the sample was finalized, SEM was used to check the final result. Figure 3.10 shows SEM images of the final master from the top and tilted perspectives.

3.6.3 Preparation of Target Substrates

Step	Deposition Technique	Material	Thickness
Step 1	PECVD	a-Si	100 nm
Step 2	ALD	Al_2O_3	12 nm
Step 3	PECVD	SiO_2	50 nm

FIGURE 3.11: Schematic (top image) and detailed value of thickness, material, and used technique (table) of the layers deposition to apply for the multi-step pattern transfer.

As shown more generally in Section 3.5, the substrate of the target sample for NIL, in this case quartz, must be coated with several layers in order to apply the previously described three-step layer transfer process. As it can be seen in Figure 3.11, in the first step, the quartz is coated with 100 nm amorphous silicon (a-Si) using plasma enhanced chemical vapor deposition (PECVD), which will be the metasurface material to be patterned. Subsequently, the Al_2O_3 layer is deposited with atomic layer deposition (ALD) with a thickness of 12 nm. This layer will constitute the protective layer. Finally, the sample is coated with SiO_2 at 50 nm, again using PECVD.
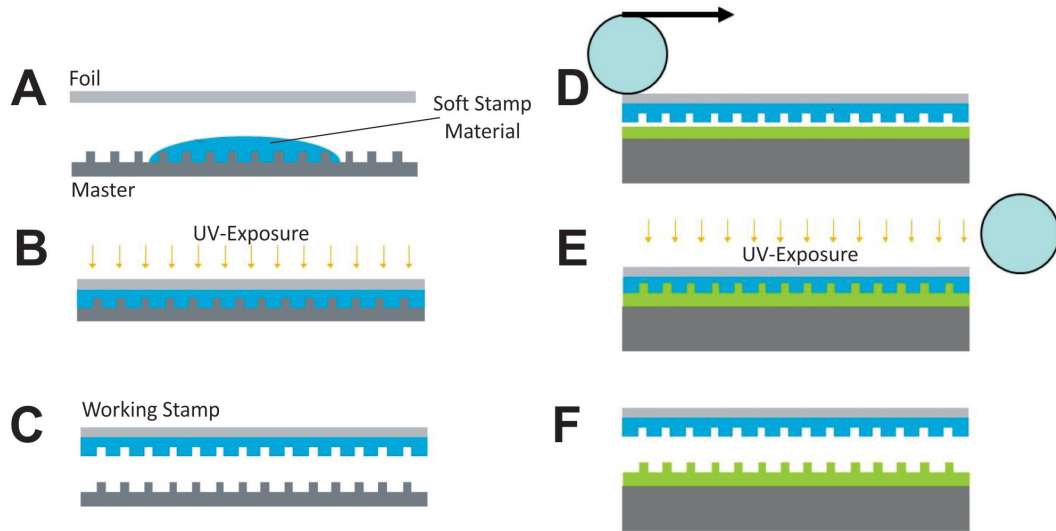
FIGURE 3.12: Schematic of the NIL process flow. Here, after the stamp fabrication, the pattern is imprinted on the UV-curable resist, ready to be transferred. (A-C) Fabrication of working stamp on foil substrate, (D-E) Imprint using roll on process.

3.6.4 NIL Patterning Process

As described in general before in Sections 3.4 and 3.5, after that the layers are successfully deposited on the substrate and the master is finalized, the NIL can take place. In Figure 3.12 the process flow is described. Before any process, an anti-sticking layer is applied on the master template. To start, the soft stamp material is dispensed on the master (Figure 3.12 A), then the foil substrate and the master are driven together and the soft layer is cured by UV exposure (Figure 3.12 B). When the working stamp is released (Figure 3.12 C), the negative of the nanostructures is ready to be imprinted on the target substrate. The imprinting is performed using a roll-on process. Here, the roll starts to move across the foil (Figure 3.12 D), keeping a conformal contact between the stamp and the substrate. When the roller has finished, its movement across the substrate, the sample is exposed to UV light (Figure 3.12 E). Finally, the foil is separated from the substrate. The substrate pattern is ready to be transferred into the target substrate layer.

3.6.5 Pattern Transfer and Final Sample

The three-layers transfer process described in Section 3.5 is now used to transfer the pattern into the a-Si. In Figure 3.13, the detailed description of the transfer process is shown. First, the residual layer is removed with ICP-RIE, then the SiO_2 is etched by 50 nm with RIE by employing CHF_3 to transfer the pattern into the transfer layer. The remaining resist was selectively removed by using HBr and the patterned transfer layer was then transferred into the protective layer by first etching Al_2O_3 and second the a-Si. This transfer was performed with ICP-RIE by using BCl_3. In the end, the sample was dipped in BHF to remove the remaining SiO_2 and Al_2O_3 to clean the sample. As stated earlier, thanks to this transfer process, the semiconductor surface is completely cleaned and the lateral dimensions are not affected by non-selective etching.
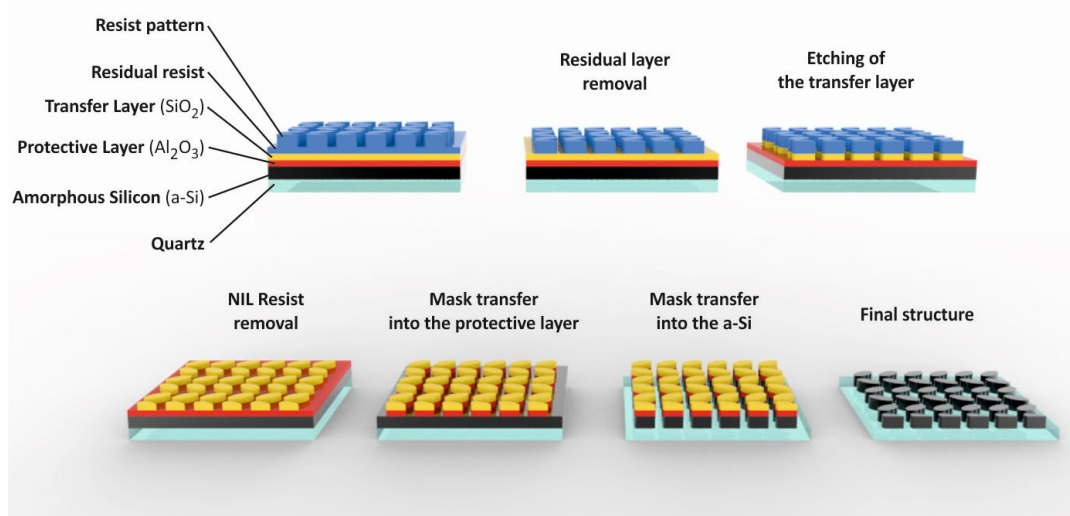

FIGURE 3.13: Schematic of the final structure transfer process flow. Here, the three-layer process presented in section 3.5 is used.

3.6.6 Metrology of the Fabrication Results

Prior to reporting the processing results, Atomic-Force Microscopy (AFM), Helium Ion Microscopy (HeIM), and Scanning Electron Microscopy (SEM),
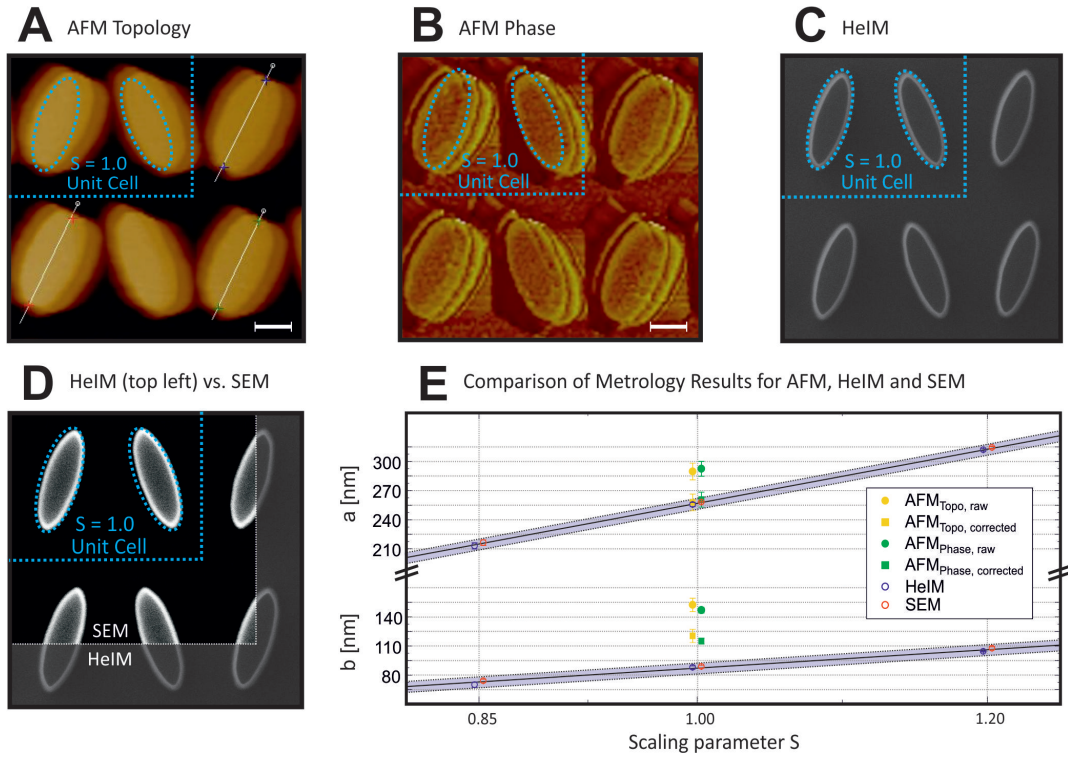
FIGURE 3.14: Comparison of metrological results for the final processed sample using AFM topology (A), AFM phase (B), HeIM (C), and SEM (D) (scaling bars: 100 nm). (E) Extracted values for the main parameters of the ellipses, *a* and *b*, for three scaling values *S* = 0.85, 1.00, and 1.20, respectively. The purple lines show the linear geometry variation with consistent, slightly larger SEM values compared to HeIM.

are assessed to test their metrological capabilities for a-Si metasurfaces on quartz. Figure 3.14 shows the images acquired for the processed sample with *S* = 1.00. Structures in AFM topology appear too large compared to the design (the unit cell is depicted as cyan overlay) (Figure 3.14 A). This is most likely due to the finite tip radius (around 20 nm diameter) as well as the step edges. As it can be seen in Figure 3.14 B, "shadows" indicate that the tip is partially out-of-contact. When compared to AFM, HeIM images are more accurate (Figure 3.14 C) since the circumference can easily be determined. However, in order to drain charges, samples had to be coated with 2 nm of platinum (Pt). Slightly more blurred edges appear in the SEM images (Figure 3.14 D) for both the SE2 and the in-lens detector. The direct comparison with HeIM shows that the center of the edges appears white in the SEM images

and should be taken as a physical boundary. The measurement accuracy by SEM for the upper edges of the metasurface is estimated to be around $\pm$ (2-5) nm. Therefore, SEM is ideally suited for measuring the dimensions of the elliptical metasurfaces and will therefore be used for all subsequent metrology tasks.
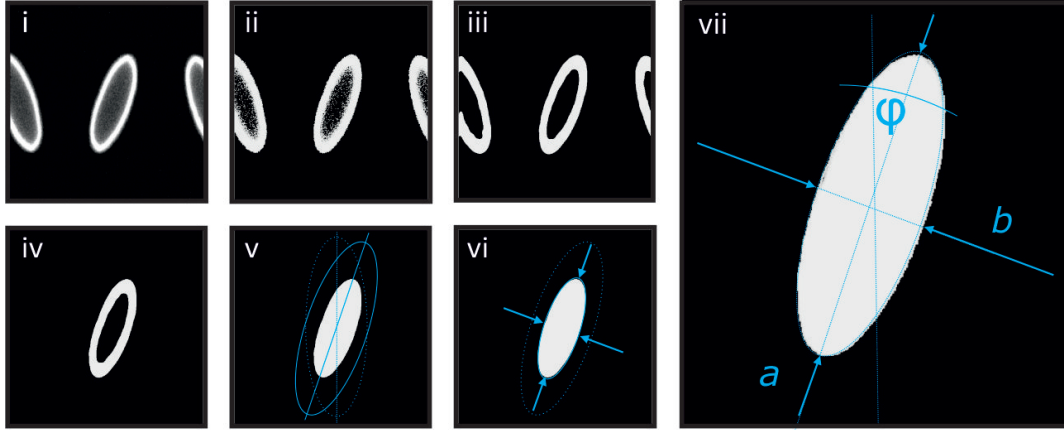

FIGURE 3.15: Automated Image Recognition Process for Metrology: automated image recognition/processing steps by (i) converting an SEM raw image into a binary image (ii), applying an FFT Filter (iii), removing border objects, and filling open areas within the structures (iv). Finally, pattern matching is performed using an ellipse shape to fit both angles (v) as well as long and short axes (vi), as depicted for the final processed image (vii).

First, the uniformity of individual metasurface elements was assessed across arrays of 200 μm x 200 μm (Figure 3.8). This is an essential characterization step as electron-induced proximity effects of densely-packed structures usually affect the uniformity, leading to alternating dimensions of the structures inside the arrays compared to the ones located at or close to edges. For the highly geometry-sensitive metasurfaces, smallest deviations from the nominal dimensions will result in locally different optical behavior and broadened optical absorption features when averaged over a large area. Furthermore, the inter-array uniformity is an important factor if large surfaces shall be created where all elements are intended to have identical optical properties.
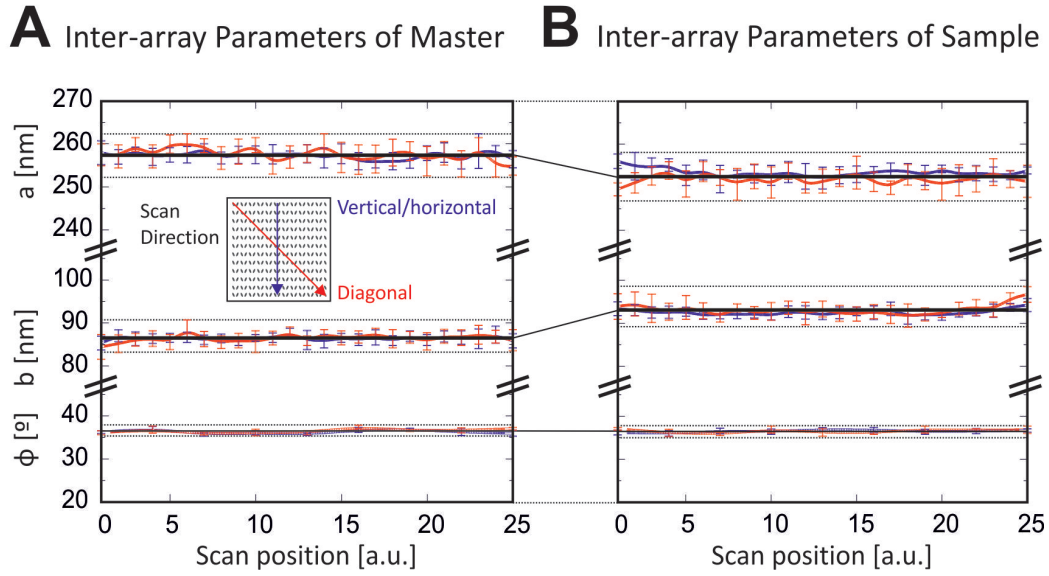
A Inter-array Parameters of Master   **B** Inter-array Parameters of Sample

F<small>IGURE</small> 3.16: Inter-array parameters determined for the Si master (A) and the processed sample (B) for the vertical/horizontal (blue trace) and diagonal (red trace) scan directions, respectively. The black lines represent the average values of the entire scan trace.

To determine the relevant parameters *a* and *b* for individual elements across the entire array, high-resolution SEM imaging is conducted along vertical/horizontal or diagonal line scans across an array (Figure 3.15), followed by automated image recognition (flattening, binarization, single-object isolation, pattern matching) and parameter extraction as illustrated in Figure 3.15. As the image recognition is based on an ellipse as the geometrical reference object and its angle is left as a degree of freedom for the pattern matching routine, the angle between the pair of ellipses can also be extracted and used as a measure to determine deviations from the perfect ellipse shape. To prevent charging upon SEM (at 3 kV), the final a-Si structures on quartz were coated with a uniform, 2 nm-thin layer of Pt which is, however, not needed for the high-conductive Si master.

Figure 3.16 A and B show vertical/horizontal (blue) and diagonal (red) line scans representing measurements of 8 ellipse pairs at each point for both Si master (B) and final sample (C), respectively. For the Si master, $a = (257.5 \pm 4.5)$ nm, and $b = (86.3 \pm 2.8)$ nm is found, as well as $a = (252.5 \pm 4.6)$ nm and

$b = (92.8 \pm 3.3)$ nm, for the final sample, respectively. The decrease of -5 nm for a and the increase of +8 nm for b upon replication can be explained by the volumetric shrinkage effects of the working stamp and the NIL resist upon cross-linking. The result is a superposition of bulk and surface interactions. The root cause of the anisotropic behavior, however, has not been identified yet, but is consistent and repeatable across all scaling values. Hence, the effect can be compensated by slightly adapting the master design. Looking at the scatter of all traces, no signs of proximity effects can be found within the measurement accuracy as more stochastic variations are revealed around the mean value, both for the Si master (deviation of $\pm$ 4.0 nm around the mean value) as well as for the final sample (deviation of $\pm$ 5 nm around the mean value). Hence, the use of a high-conductive substrate for EBL together with the novel indirect pattern transfer results in high-accuracy and uniform metasurfaces.

3.6.7   Comparison of Patterning Approaches

Figure 3.17 A shows a sketch of the final ellipses arranged in an array. A single ellipse fabricated as described above (left) and one structured by direct pattern transfer (right) are shown in Figure 3.17 B. As can be seen, the one on the right is still covered with residual NIL resist and suffers from defects and dimensional inaccuracies, in contrast to the almost perfect left. For the entire array, the structures appear smoother than in direct EBL writing as the later process suffers from proximity effects (Figure 3.17 C).
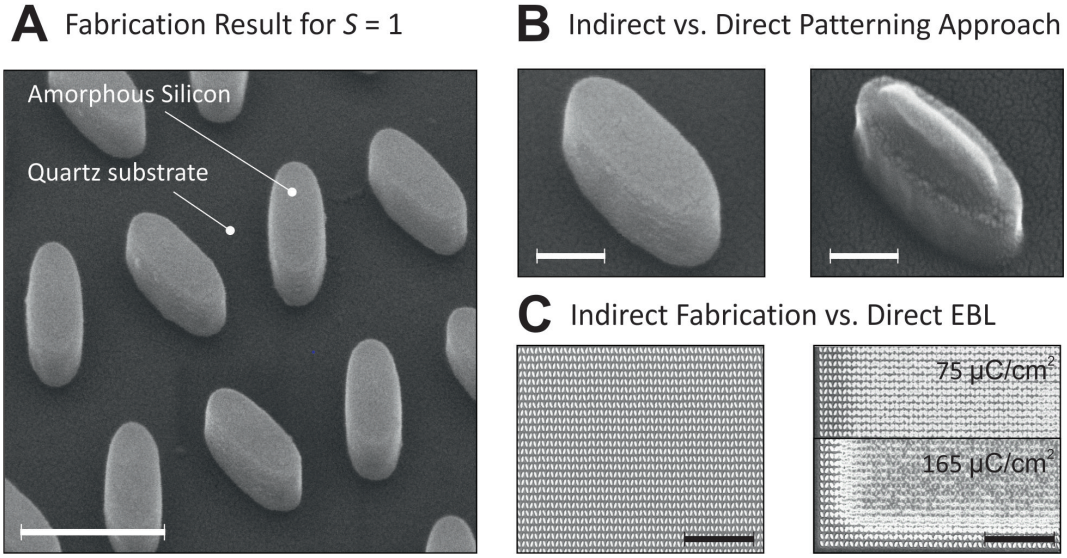
A Fabrication Result for *S* = 1

Amorphous Silicon

Quartz substrate

B Indirect vs. Direct Patterning Approach

C Indirect Fabrication vs. Direct EBL

75 µC/cm²

165 µC/cm²

FIGURE 3.17: SEM images of the final device: (A) Example of
ellipses fabricated for S = 1.00 (with a = 280 nm, b = 100 nm,
and h = 100 nm) on a transparent quartz substrate (scaling bar:
300 nm). (B) Comparison of indirect and direct patterning ap-
proaches for individual ellipses (scaling bars: 100 nm). (C) SEM
images acquired at the corner of an array fabricated by the in-
direct process (left) versus directly patterned by EBL (at 20 kV)
(right); the two nominal exposure doses indicated are both var-
ied substantially towards the center of the array according to
iterative, empirical electron proximity effect (PEC) corrections,
as explained in Section 3.2 (scaling bars: 5μm).

3.7 Conclusions

A novel fabrication route to create high-accurate ($<$ 10 nm) metasurfaces on
transparent substrates was demonstrated (Figure 3.18).

The fabricated structures were geometrically scaled to be able to tune in res-
onance behavior, from the NIR to the visible wavelength range, as it will be
shown in the next chapters. These devices, combined with a scalable and
mass-fabrication compatible fabrication route, represent an opportunity to
leverage the unique optical properties of Si-based metasurfaces, such as their
narrow and sensitive resonances, for various applications. The presented
processing approach allows cost-effective samples, which are roughly 2-3 or-
ders of magnitude lower in price compared to EBL processing alone, to be
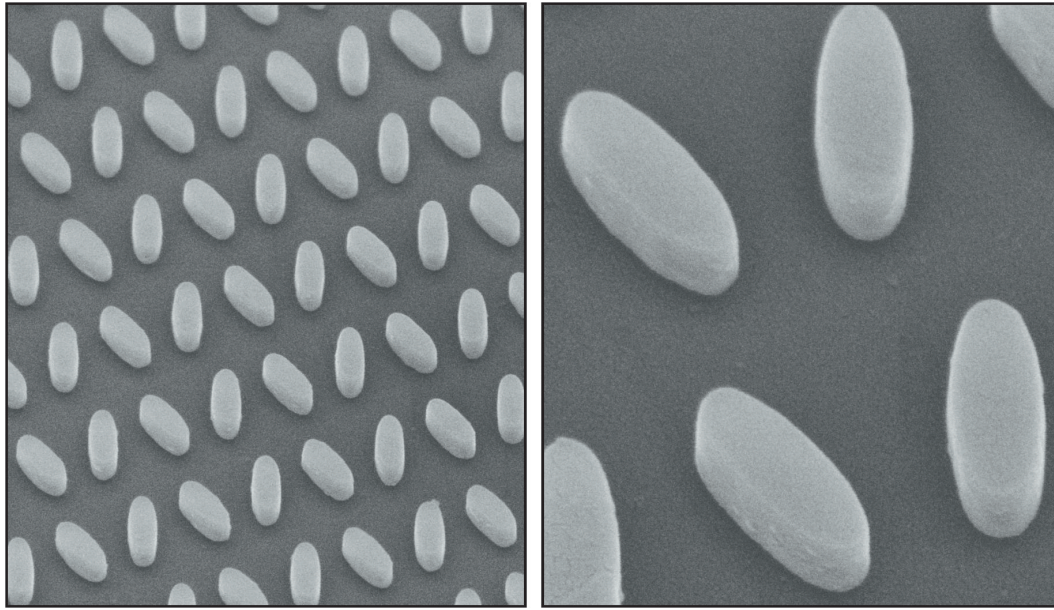
FIGURE 3.18: SEM Micrographs of the final device

fabricated by combined EBL and NIL, and which can fully compete with non-scalable fabrication approaches on the nanometer scale. The novel fabrication route presented is generic to other geometries, different material stacks, other operation principles and applications beyond optics and metasurfaces. The process can be realized with masters created by any nano-patterning method, including EBL, and is upscalable to large areas by step-and-repeat techniques.

Chapter 4

Optical Characterization

4.1 Introduction

In order to characterize and evaluate the optical performances of the fabricated metasurfaces, different approaches can be used. These methods depend on the purposes and application of the metasurfaces, but also on the physical working principle which produce the resonance shift in the metasurface. In the following, a customized microscopy system will be introduced to quantify the intensity shifts of the fabricated metasurfaces. First, a short introduction to optical transmission spectroscopy is given together with the general signal processing method that will be used in the following chapters. Next, a short overview of microfluidic systems capable of incorporating metasurfaces is provided. Later, in the results section, the optical setup design is described in detail and the control of the system is demonstrated by using commercially available software. Finally, the microfluidic chamber design and fabrication thereof are shown.

4.2 Optical Transmission Spectroscopy

In general, the purpose of optical spectroscopy is to analyze the connection between the variation of the light intensity and the wavelength of the input light source employed to optically characterize the response of a sample. For instance, the light interacts with a sample and is spectrally analyzed with the

help of a spectrometer to determine properties such as reflectivity, transmissivity, emissivity, or absorption.
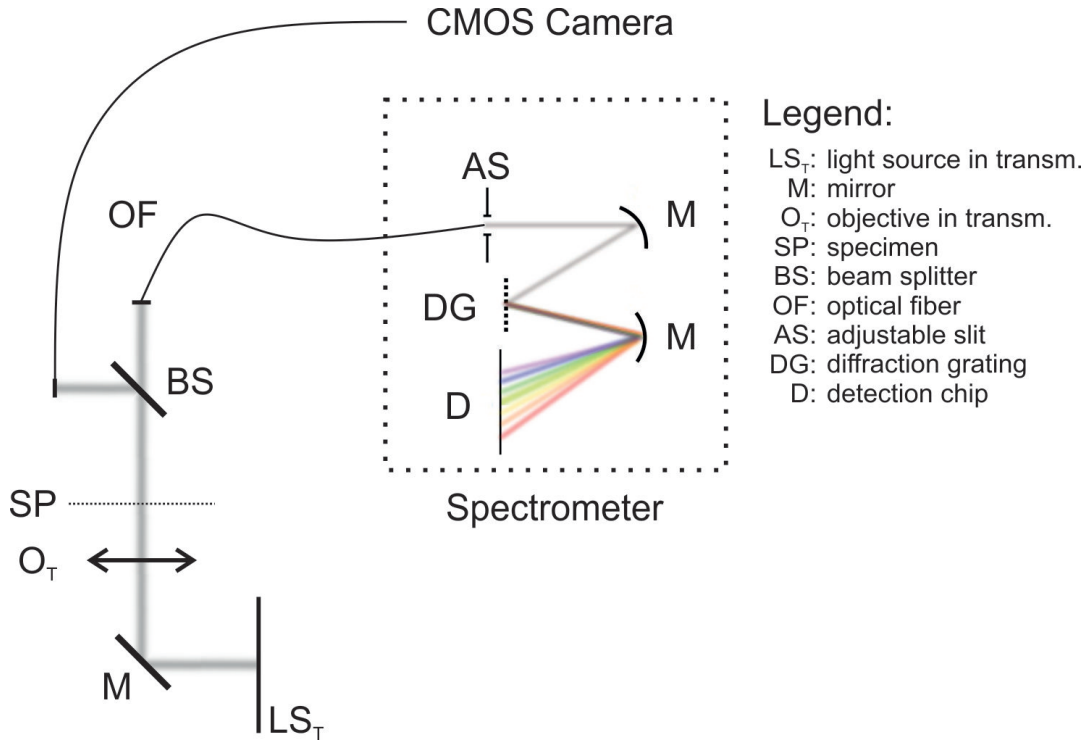

FIGURE 4.1: Transmission optical spectroscopy schematic. Simplified schematic of setup use for transmission optical spectroscopy. The light source is connected through an optical fiber to the microscope, allowing the light to be directed into the spectrometer. Before entering the spectrometer, the light is spatially separated by the help of a diffraction grating, based on its wavelength. In this way, the light intensity can be collected by a photo-sensitive detector (e.g., photodiode) and expressed with a certain spectral resolution.

In Figure 4.1 an optical spectrometer schematic is shown, which can be employed in transmission configuration. Here, the light impinging on the specimen is then collected and sent, through an optical fiber, to the spectrometer. The light coming to the spectrometer can be adjusted with the help of a slit with controllable aperture, to select the amount of light that can reach the detector in order to do not saturate it. Furthermore, it is possible, by selecting the suitable diffraction grating in the spectrometer, to rule the output detection spectral resolution. More specifically, the lower the grating pass,

the higher the resolution. On the other hand, in this configuration, only a finite spectral wavelength range can be analyzed. Here, the light diffracted by the grating is splitted and collected by the detector region, giving the output transmitted light spectra with respect to the wavelength range of the selected grating. It is usually necessary to conduct two measurements to gather sufficient information and enable a relevant analysis of samples using optical spectroscopy in order to collect the characteristic emission of each light source.
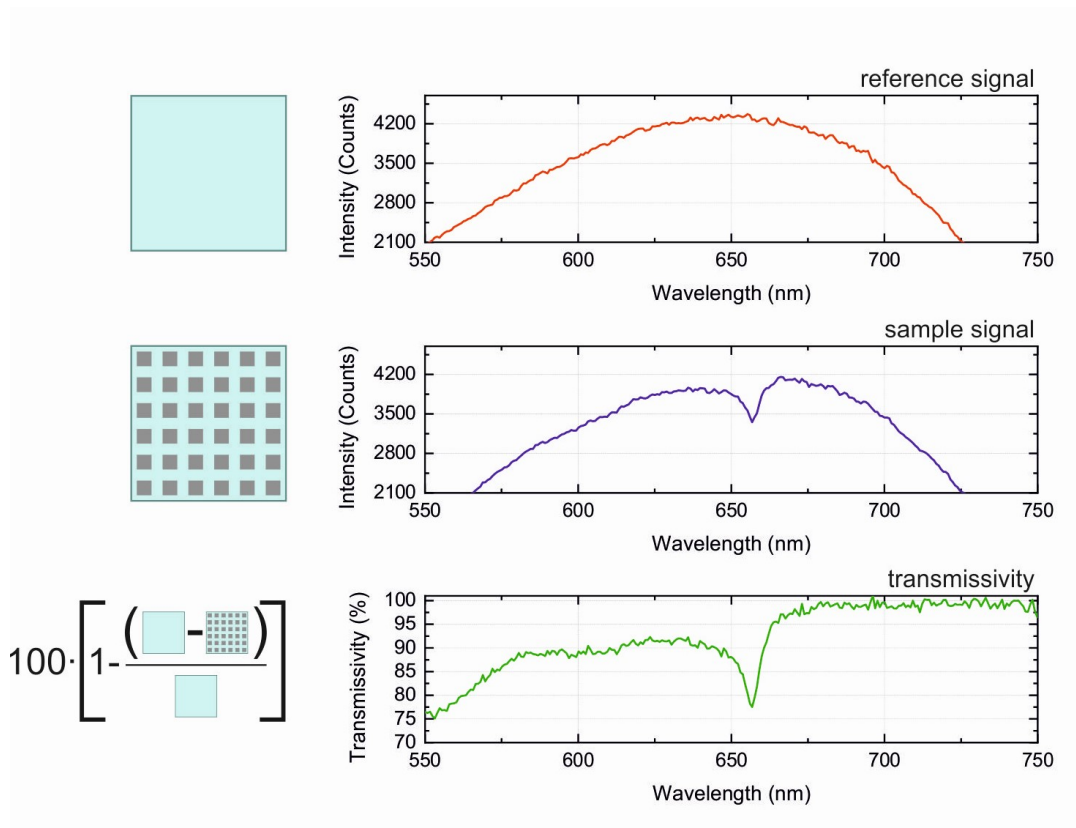
FIGURE 4.2: Optical spectroscopy spectra processing and manipulation. The sample output spectra is usually subtracted from a reference one, acquired previously to determine the light source's emission spectrum. The result is then normalized and multiplied by 100 to obtain the transmissivity value in percent.

First, the reference spectrum of the substrate without devices is collected, red in Figure 4.2, it will be used later to avoid any influence from the substrate optical properties, the characteristic emission of each light source, but also

from the external environment. These reference measurements can be different depending on the type of experiment conducted. For example, it can be a clear, unpatterned part of the same sample, or a totally different sample where the optical response is already known. The second measurement to be conducted is the sample spectrum, violet in Figure 4.2, which represents the optical response of the analyzed sample, consisting of both substrate and devices. The two collected spectra are then usually subtracted from each other and normalized, as shown in green in Figure 4.2, to determine the inherent optical properties.

4.3   Metasurfaces Integration into Microfluidic Devices

Integrating dielectric metasurfaces in microfluidic devices enables practical sensing experiments. Microfluidics is a field of research for controlling and guiding the flow of liquids and gasses at the microscale level. Microfluidics is crucial to enable operation with minute quantities of analytes and bioanalytes, therefore significantly improving the sensitivity of optical and electrochemical sensors[175,115,190,29]. Besides, microfluidic devices have the capabilities to mix various analytes, sort different particles, and form droplets of specific sizes[133,143]. Additionally, microfluidic systems are highlighted by their user-friendly operation principles, which is a relevant aspect for real-world applications.

Figure 4.3 shows some examples of microfluidic devices. The microfluidic integration of metasurfaces operating at visible and near-IR spectral ranges has been successfully demonstrated before[175]. An image of the integrated multichannel microfluidic chip is presented in Figure 4.3 A. The chip is 25 mm x 25 mm with a thickness of 0.5 cm, and the sensor array in the center is visible as a darker zone below the channels. Another microfluidic application is shown in Figure 4.3 B. In this study[190], a microfluidic network of 1000 μm (L) x
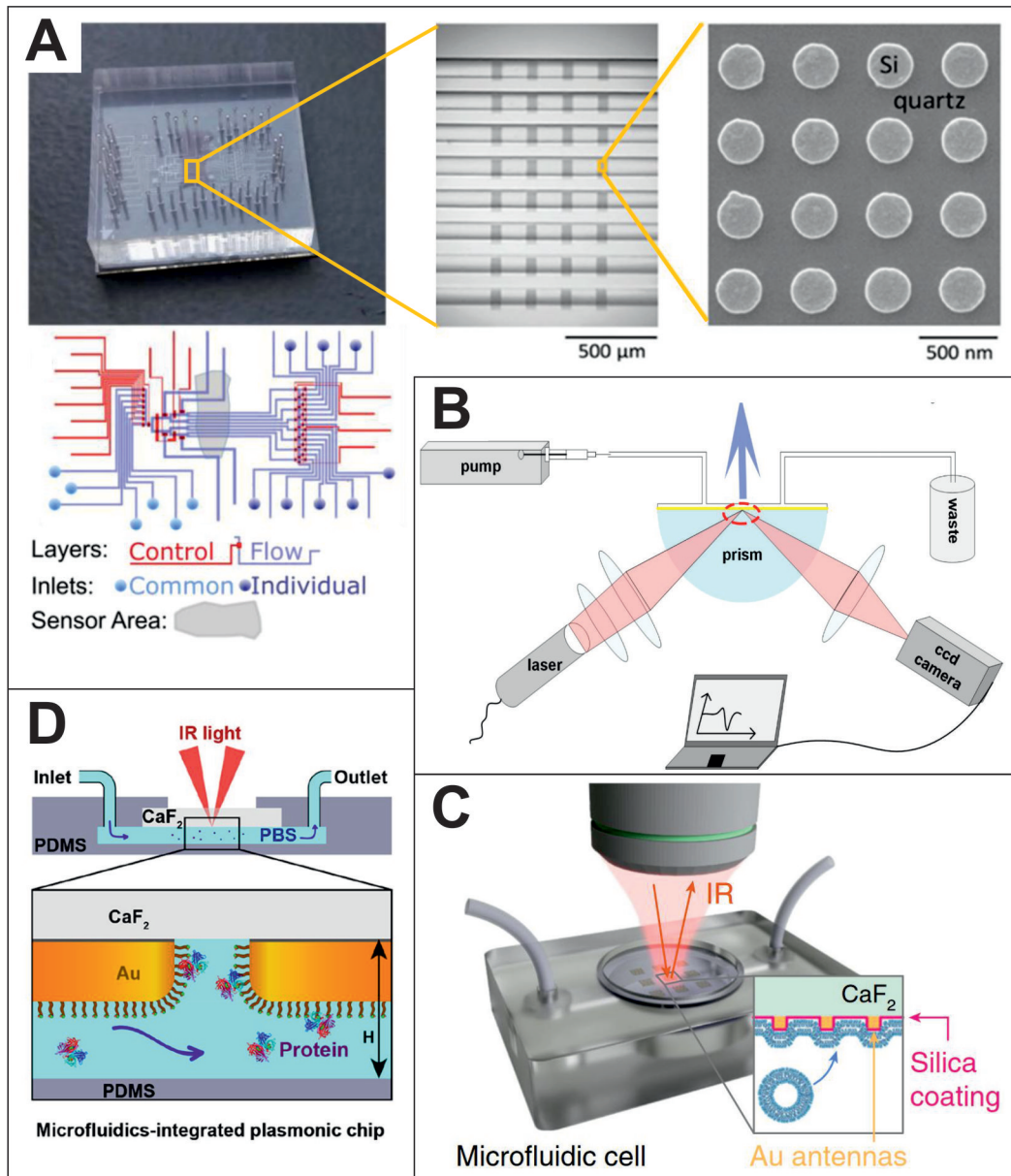
FIGURE 4.3: Schematics of different microfluidic implementations. (A) Multichannel microfluidic device (left), a nearer view of the 8 flow channels revealing several sensors (middle), and a SEM image of a Si nanodisk metasurface (right). The sensor array in the chip's midsection appears as a darker zone beneath the channels (adapted from [175]). (B) Surface plasmon resonance (SPR) sensor device optical system's schematic (adapted from [190]). (C) PDMS micro-fluidic cell for controlled delivery, with experimental configuration (adapted from [131]). (D) Illustration of the in-solution experimental setup, not to scale, showing the fluidic inflow, outflow, and optical pathway (adapted from [70]).

100 μm (W) x 180 μm microchannels was constructed on a polydimethyl-siloxane (PDMS) slab as an optical system for the surface plasmon resonance (SPR) sensor device. The PDMS chip was made using a traditional replication molding process, in which the master was made using SU8 photoresist and a silicon wafer by the use of structured photolithography. A PDMS microfluidic cell, as shown in Figure 4.3 C, provides for the controlled delivery of diverse compounds[131]. The time evolution of both lipid bilayer synthesis and subsequent streptavidin-binding kinetics may be studied *in situ* using this combined microfluidic technique. Another example is shown in Figure 4.3 D, where, given that the CaF_2 substrate is highly transparent in the mid-IR range, it was possible to illuminate the chip from the back-side and integrate the microfluidic devices. The PDMS device's flow channel height H in this example is 30 μm. The zoom shows biotin groups exposed by functionalized gold antennas, which capture proteins from the flowing solution[70].

4.4 Results

For characterization of the metasurface device fabricated, a custom-built optical microscopy system was designed and assembled to image the transmitted light intensity upon exposure to different analytes. The setup described here allows, in parallel, to have both a high-resolution spectroscopic read-out and an additional CMOS camera read-out. In contrast to conventional spectrometers, using a CMOS camera allows spatially probing of the spectral response of the metasurface over substantial areas (up to cm-scale), allowing also to scan different arrays by scanning the sample as will be described later. The use of such a setup is possible thanks to the very narrow resonances (< 5 nm), adsorption dips, and large shifts (tens of nms) of Mie resonances, described in Section 1.6.2, in combination with a narrow excitation.
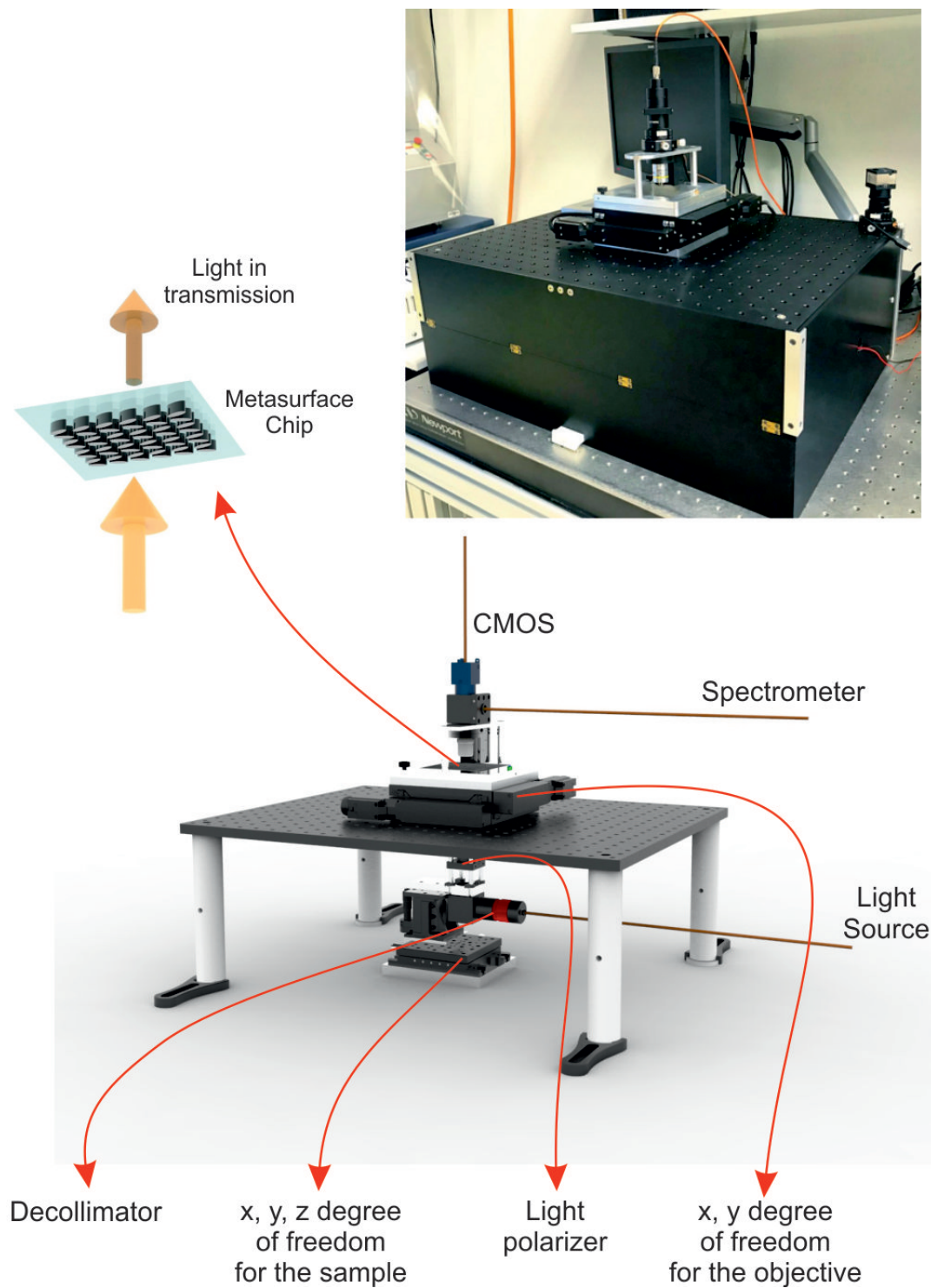
FIGURE 4.4: Characterization Set-Up Design Rendering. A customized setup allows to work with light in transmission and to have many degrees of freedom, both for the sample and the objective. Moreover, the characterization system is able to work in parallel with a spectrometer and a CMOS imager, thanks to a beam splitter. On the top right, a picture of the setup is displayed.

4.4.1 Design and Implementation of the Optical Set-up

The design presented in this chapter allows for characterizing Mie resonances occurring at normal incidence. Hence, the chips can be mounted in a collinear handheld sensing system working in transmission. In Figure 4.4, a rendering of the final design for the characterization setup is shown. Here, a Newport Q-Series quartz tungsten halogen lamp 66877 with 100 W and approximately 850 lm flux was used to acquire the absorption resonances in transmission. Before illuminating the sample, the broad-band light was decollimated and then linearly polarized using a Glan-Taylor polarizer with 10 mm clear aperture, coated between 650 nm and 1050 nm. After that, the light was collected using an Olympus LMPLFLN100x objective, with a magnification of 100x, a numerical aperture of 0.86, and a working distance of 3.4 mm. Additionally, the objective was equipped with a piezoelectric stage for fine tuning of the focus distance, allowing spot measurements to be taken.

The spectra can be acquired either by:

- an Ocean Optics QEPro spectrometer with back-thinned Si CCD, TEC-cooled and a sensitivity from 400 to 1100 nm, or

- a CMOS imager working in the VIS-NIR regime.

The whole system was designed using Rhinoceros, a commercial 3D computer-aided design (CAD) software. In Figure 4.4, it is possible to observe the final setup, with the customized and the commercial components assembled together. Apart from the adapting parts designed to combine the XY- and Z-stages in a final setup, a special focus was set to customize the top part of the set-up, where the piezoelectric objective is mounted, as shown in Figure 4.5.

The top part is removable and an extra degree of freedom was added by implementing a 3-point stage to be able to tilt the objective with respect to the sample by using fine adjuster screws. Moreover, to be able to hold the two adapter stages together, 3 pockets in each stage were fabricated and filled
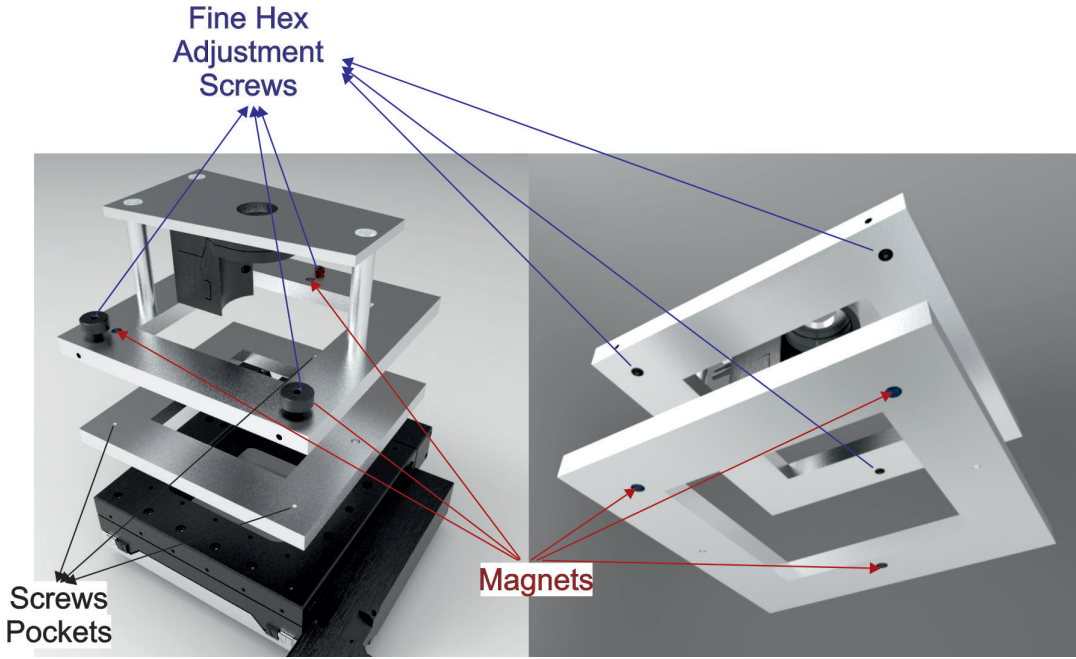
FIGURE 4.5: Schematic of the top part of the characterization setup.

with small super-magnets, providing enough force to keep a stable position but also easy to remove if necessary. To allow the spectrometer to be replaced by a simple CMOS imager and to observe thereby changes in the integrated absorption, a narrow-band light source needs to be used instead of the classic, broad-band, halogen lamp. For this reason, a monochromator was used as a light source to conduct experiments.

In the right panel of Figure 4.6, a picture of the monochromator used is shown. Since many settings of this tool need to be controlled, together with the setting of the other tools, a custom-made program was developed which communicates with all the devices used (spectrometer, monochromator, CMOS imager, XY stage). This will be explained in details in the next section.

4.4.2 LabVIEW^{TM} -Based Control Software

As mentioned in the previous section, automation and control of all actuators and detectors of the optical read-out system were developed with

LabVIEW$^{\text{TM}}$ software. In particular, all the controls related to the μm-precise positioning of the XY stage, the spectrometer, the CMOS image sensor, and the various settings of the monochromator are combined in one software.
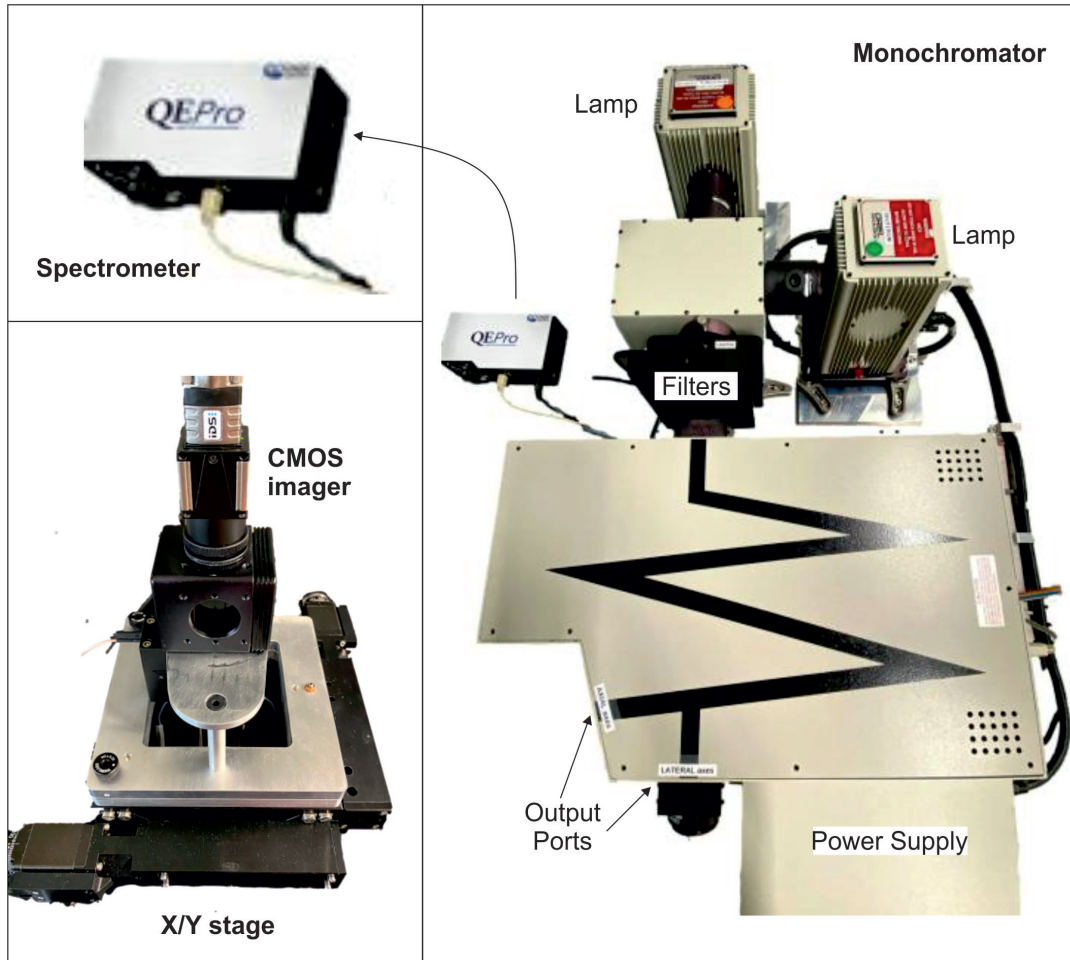
FIGURE 4.6: Pictures of the components used in the read-out system. All components (spectrometer, monochromator, CMOS imager, XY stage) were controlled by a custom-made software to automate the experiments, e.g., for scanning and combined spectral acquisitions.

LabVIEW$^{\text{TM}}$ is a software developed by National Instruments that provides an environment for graphical programming. User-friendly programs and user interfaces can be developed not only for instrument control, operational control systems, and data acquisition but also as a tool for data analysis. An intuitive tool for the user to perform the entire read-out procedure was developed, starting from the basic procedures for characterization over analyzing

the spectral results to saving the data in the desired format, (e.g., ".txt" format).
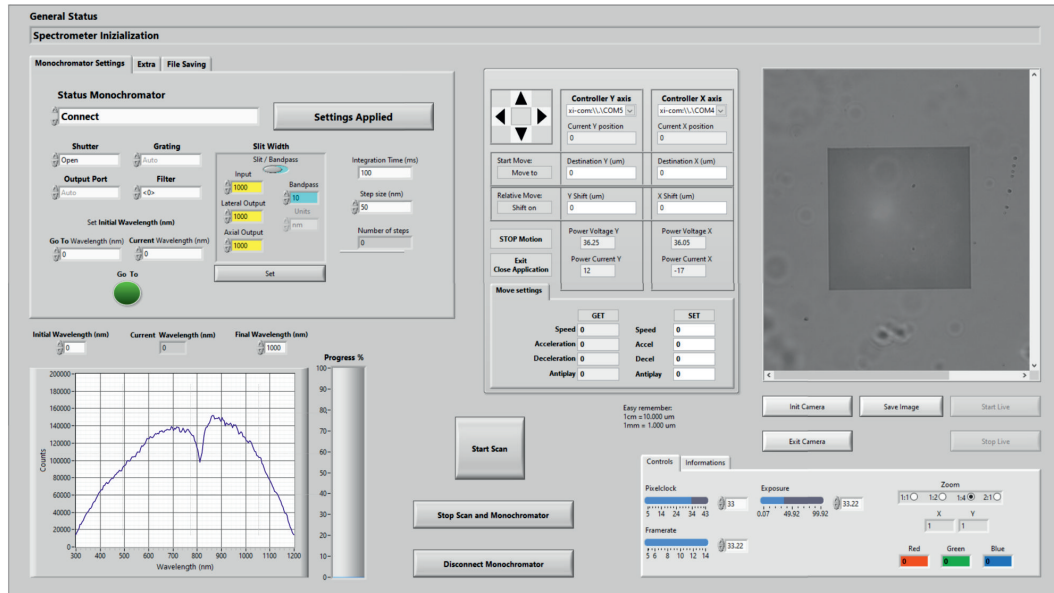
FIGURE 4.7: Screenshot of the graphical interface of the software to control the optical read-out system. It shows the following environments: XY stage (top, center), monochromator (top, left), spectrometer (bottom, left), and CMOS camera imager (right).

As it can be seen in Figure 4.7, the software can be divided into four main components:

1. **XY Stage**: in this component, shown in Figure 4.7 top center, it is possible to independently set the parameters for the controllers in the horizontal X and Y axes. In more detail, the following parameters and settings can be customized:

   (a) Move to: in this configuration, it is possible to reach an absolute position by entering the coordinates;

   (b) Relative move: here, the position can be changed relative to the current one;

(c) <u>Extra settings</u>: in this panel, the values for speed, acceleration, and deceleration can be set;

(d) <u>Manual movement</u>: moreover, to be able to move in a quick but less accurate way, a manual controller was implemented, which acts by pressing the buttons for a certain time duration to trigger the movement.

2. **Monochromator**: in this component, shown in Figure 4.7 top left, the following parameters and settings can be customized:

   (a) <u>Shutter</u> position, which can be open or closed to allow the light to pass;

   (b) <u>Filter</u> setting, which is composed of 5 different choices, each one with a different wavelength range. These filters can be exchanged in the filter wheel;

   (c) <u>Grating</u> range for 4 different wavelength ranges: 200-600 nm, 200-1400 nm, 475-1400 nm, and 875-2200 nm;

   (d) <u>Wavelength</u> setting, choosing the initial and final wavelengths, and the number of steps to be performed, upon scanning;

   (e) <u>Output Port</u>, since two different light exits are present in the tool, the desired one has to be selected (lateral or axial);

   (f) <u>Slit / Bandpass</u>, here, it is possible to set the bandpass value or to define the desired input and set, separately, the output for the axial and the lateral port independently.

3. **Spectrometer**: in this component, shown in Figure 4.7 bottom left, the output spectrum is displayed in the working wavelength range and the data is saved in the selected folder path with the desired name of the file. Moreover, the measurement progress percentage is shown in the left column.
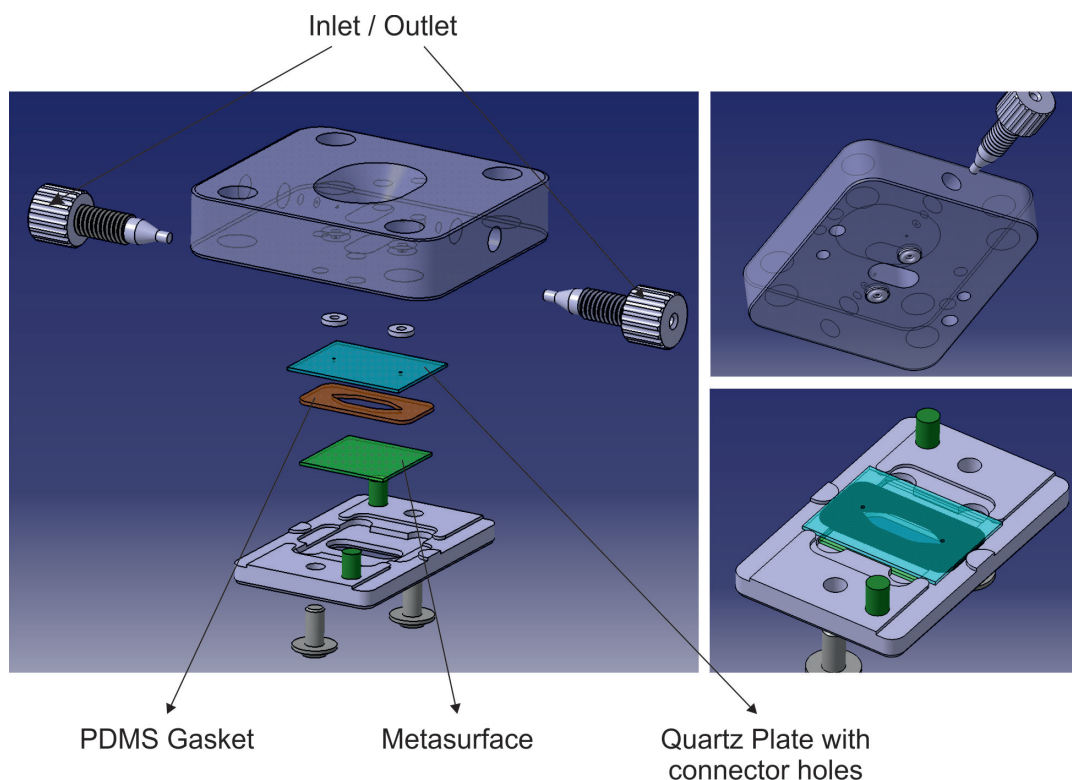
FIGURE 4.8: Microfluidic chamber design and working principle. The analyte is introduced through the inlet of the microfluidic channel and incubated on the metasurface, loaded between the chip and the quartz plate divided by the PDMS gasket. The analyte solution can be washed and the spectroscopic measurements performed iteratively.

4. **CMOS Imager**: in this component, shown in Figure 4.7 at the top and bottom right, the image is shown. Here one can adjust the exposure and zoom to the desired values and then save the image. Furthermore, by moving the cursor on the image acquired, it is possible to read the Cartesian position and the values of the red, green, and blue components.

4.4.3 Microfluidic Design and Fabrication

In this section, a custom-built flow microfluidic system is introduced, that enables liquid exchange of precise quantities, e.g., used for rapid cycles of metasurface washing and incubation steps.

The custom-made microfluidic cell shown in Figure 4.8 consists of two different aluminum parts, which are tightened together by two screws. Due to its outstanding mechanical qualities, reusability, simplicity of manufacturing in conventional mechanical micromachining, and ease of setup, aluminum is a good contender for the microfluidic chip substrate.

In the left part of Figure 4.8, the opened structure of the microfluidic chamber is displayed. Here, the sensor chip is placed on top of the bottom aluminum part of the microfluidic cell with the metasurfaces facing up inside the microfluidic chamber. Here, they can interact with the analytes. On top of it, a quartz plate with connector holes was used to allow the liquid to flow in a transmission configuration. To ensure zero water leakage from the quartz and metasurface chip interface, a thin PDMS-based gasket is introduced, which allows to hermetically insulate the microfluidic cell. In addition, two small o-rings were used between the holes in the quartz plate and the top aluminum part in order to hermetically seal the system upon liquid exchange. Inlet and outlet connectors were designed for 1/16 inch tubing. Figure 4.9 shows the microfluidic chamber fabricated, disassembled (top left), partially assembled (bottom left), and entirely assembled and mounted on the setup, ready for use (right).

Experiments of flow microfluidics are tipically conducted in different steps. The sample is first mounted in the chamber previously described, then the analytes are introduced through the inlet by using a peristaltic pump with a fixed flow rate of 30 μl / min. The metasurfaces are then exposed to the target analyte for a certain amount of incubation time. To flush away any unbound molecules, the analyte is washed away through the outlet with the desired solution after incubation. In such a way, the microfluidic system enables operation with minute quantities of analytes. The final step within each cycle is the VIS-NIR measurement of the surface-bound biomolecules. The cycle can then be restarted from step one after the measurement. Interestingly, this microfluidics method enables signal read-out after each step of surface functionalization while lowering the risk of sample contamination. Furthermore,
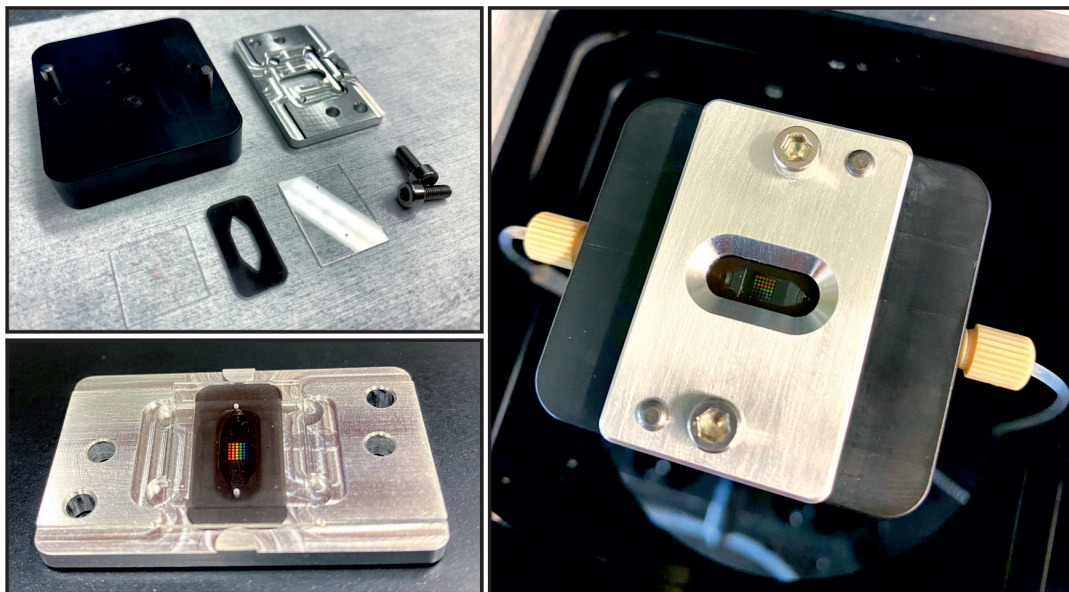
FIGURE 4.9: Microfluidic chamber fabricated. Each component of the chamber can be mounted in a pre-defined, precise position thanks to the different pockets mechanically manufactured on the aluminum part to keep in position the metasurface chip, quartz plate, and gasket.

the system can be expanded to perform real-time monitoring of molecular binding kinetics.

4.5 Conclusion

This chapter provided an introduction into optical transmission spectroscopy and microfluidics with a detailed description of the design, implementation, installation, and tools software interfacing of the custom-build optical transmission system developed during this thesis. The system is capable of measuring simultaneously with a spectrometer and a CMOS imager the output signals. Moreover, the all-dielectric metasurfaces were integrated into a custom-made flow microfluidic chamber for precise analyte delivery.

In the next chapter, the system described here will be used to measure the optical response of metasurfaces under different environments.

Chapter 5

Operation in Different Environments

Sections of this chapter are adapted from one published article, which appeared in Advanced Photonics Research (DOI: 10.1002/adpr.202200014) [126]

5.1 Introduction

The use of metasurfaces made of high-index dielectric nanopatterns has a variety of advantages for achieving great tunability. An essential property of dielectric nanostructures is their capacity to support electric and magnetic multipolar Mie-like resonances over the visible and near-infrared wavelength spectrum[51,88]. These resonances can be explained analytically by the Mie-theory, as was previously discussed in Section 1.6.2. Mie-resonant nanostructure-based dielectric metasurfaces offer a number of intrinsically resonant features, making them particularly advantageous for engineering tunability.

Notably, a strong spectral dispersion is associated with the resonant optical response of metasurfaces in the transmittance and reflectance spectra. In contrast to plasmonic metasurfaces, dielectric metasurfaces can also display quite high quality (Q) factors because of the practical absence of absorption losses[165,171,37]. Tuning is made simpler since similar spectral resonance

shifts produce more pronounced changes in optical response at particular operating wavelengths. In this chapter, an overview of the different ways to tune dielectric metasurfaces will be given, with the main focus on the tunability provided by geometrical changes and local environment refractive index changes.

5.2 Dielectric Metasurfaces Tunability

As previously introduced, there are numerous benefits to using high-efficiency dielectric metasurfaces with different functionality for next-generation tiny, low-power, and compact optical systems, and they could enable innovative and exciting functions comparable to those available today. In order to bring dielectric metasurfaces closer to practical applications, tunable metasurfaces with optical responses that can be controlled in a reversible and reproducible manner will become increasingly important.

According to this approach, numerous adjustable dielectric metasurfaces with resonance frequencies spanning from the microwave to the visible spectral range have been identified[196]. Here, optical metasurfaces with visible or near-infrared operating frequencies will be the main topic of discussion. Three groups of tunable dielectric metasurfaces can be distinguished based on their specific tuning mechanisms, as schematically shown in Figure 5.1:

- **Changes in geometry**: it is possible to vary the optical response of a metasurface by modifying the nanoresonators' shape or altering the resonator array's periodicity, either homogeneously or inhomogeneously. Changes in geometry result in changes in the nanoresonator modes and inter-element coupling strength, which affects the metasurface optical response (Figure 5.1 i).

- **Changes in the surrounding environment**: the inter-elements coupling strength and local resonances of a dielectric metasurface depend on the properties of the surrounding material. Then, metasurfaces can be
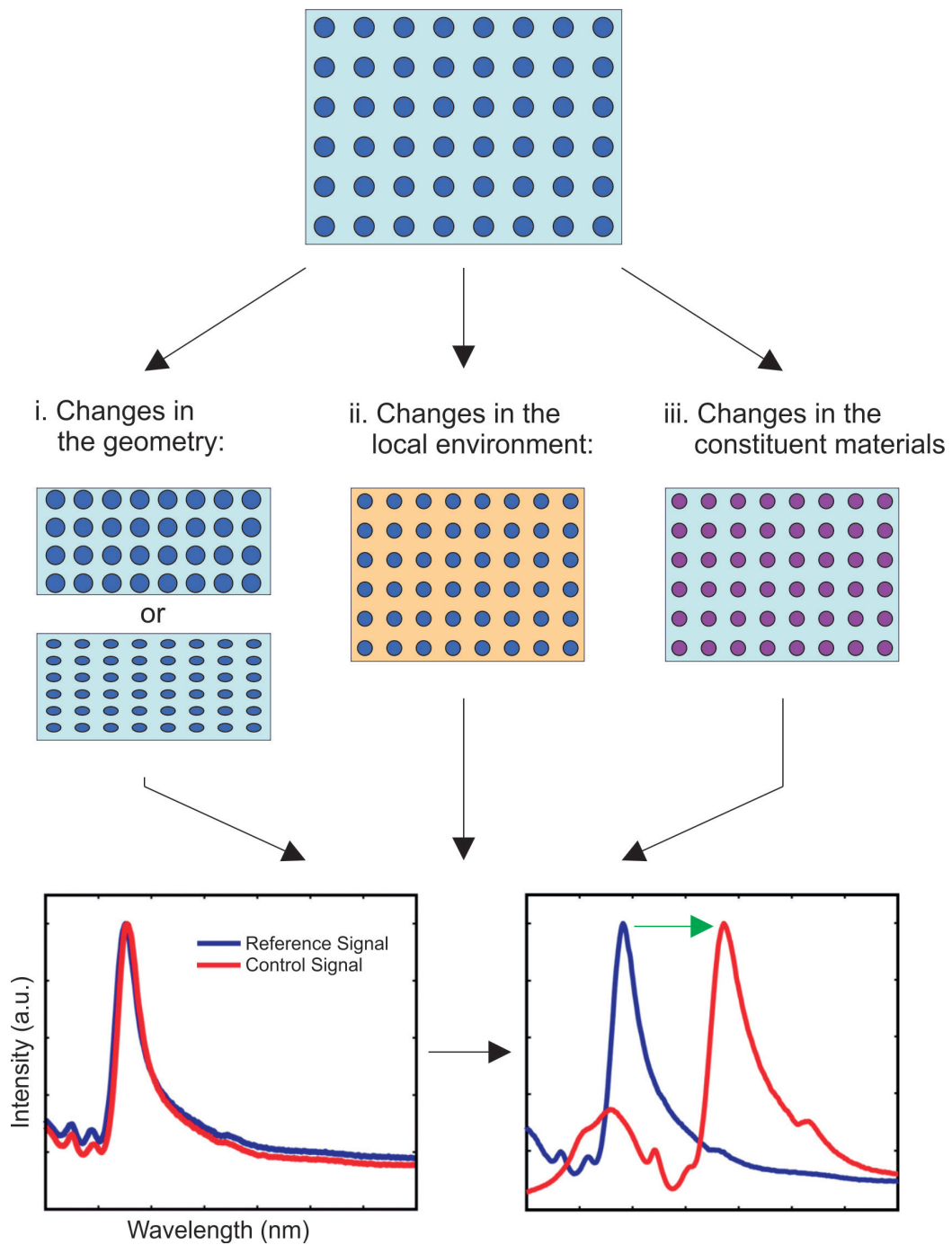
FIGURE 5.1: Schematic of dielectric metasurfaces tunability mechanisms for (i) changes in geometry, (ii) changes in the surrounding environment, (iii) changes in the metasurface constituent materials.

made tunable by immersing them in a functional material that alters their optical properties based on local environmental changes (Figure 5.1 ii).

- **Changes in the metasurface constituent materials**: changing the constituent material of nanoresonators themselves can also cause dynamic changes in a metasurface's optical response (Figure 5.1 iii).

In this work, the focus has been mainly put on the first two points, which are the changes in the geometry and the changes in the surrounding environment, as will be presented in the following Results section.

5.3 Results

In this chapter, the geometric effect of nano-elliptic structures on the optical response and the refractive index (n) sensing performance of the quasi-BIC mode has been systematically studied. Arrays of optimized tilted nano-ellipses pairs were experimentally demonstrated, and the sensitivity of tilted nano-ellipses pairs was quantified by examining their spectral variation under exposure to different surrounding media with n ranging from 1 to 1.38.

5.3.1 Sensitivity towards geometrical changes

First, the chip described in Chapter 3, Section 3.6.1, was measured in DI water (n = 1.33). Here, the unit cell and the dimensions of the ellipse were linearly scaled as described in Figure 3.7 A. The scaling factor ranging from 0.85 to 1.20 with $S = 1.00$ having major axis $a = 280$ nm, minor axis $b = 100$ nm, and height $h = 100$ nm constant.

Figure 5.2 B shows a representative absorption resonance for $S = 0.9$, acquired in transmission (thickness of the quartz substrate 525 μm) under illumination with the linearly polarized, broad-band light emitted from a tungsten lamp and the scattered and transmitted light collected with the objective and the spectrometer, as described in Chapter 4. As a consequence of the small spot

size (estimated to be $< 5\ \mu$m), the spectrum is rather noisy, but the number of metasurfaces acting actively as absorbers is finite.
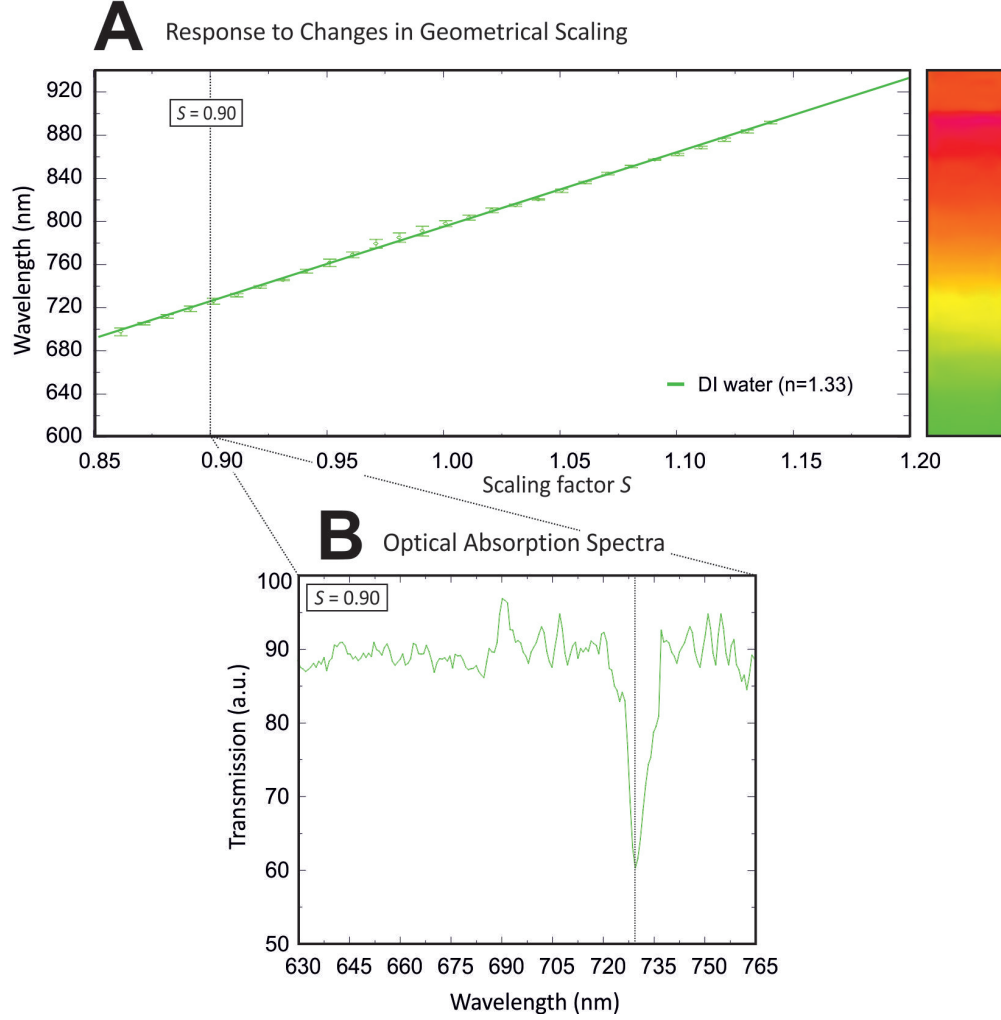
FIGURE 5.2: Optical characterization of metasurfaces under geometrical changes: (A) Scaling behavior of the resonance position as a function of *S*, varied from 0.85 to 1.20. The scaling is found to be linear, as expected. C) Spectral absorption data example for DI water as surrounding medium, exemplarily for *S* = 0.9.

Looking at the green trace for metasurfaces immersed in a 200 μm thick cavity filled with a solution of deionized (DI) water (dielectric index, n = 1.33), the full width at half maximum (FWHM) of the resonances is around 6-8 nm with extinction factors of 30 - 40 %, both depending on the chosen baseline.

When plotting the resonance as a function of scaling factor S, a linear behavior is found (green curve in Figure 5.2 A). The deviation from the linear fit is $\pm$ 2.5 nm at maximum (green dotted lines; each data point represents three measurements over the entire array).

5.3.2   Sensitivity towards dielectric environment changes

To test the same chip under different dielectric environments, first, the spectrum was collected in air (n = 1) for all the available scaling factors S, then the metasurfaces were immersed in the 200 μm thick cavity, shown in Chapter 4, Figure 4.9.

The microfluidic chamber was first filled with a solution of DI water (n = 1.33; conductivity = 0.059 μS cm^{-1}; green trace), and then isopropanol (IPA; n = 1.38; blue trace). As can be seen in Figure 5.3, the absorption resonances shifted by $\Delta\lambda$ with FWHM of 6-8 nm, similar to the previously mentioned one. Both shifts are quite consistent throughout all the scaling factors, with:

- $\Delta\lambda_{water-air}$ = (69.7 $\pm$ 2.7) nm,

- $\Delta\lambda_{IPA-air}$ = (82.7 $\pm$ 2.3) nm, and

- $\Delta\lambda_{IPA-water}$ = (13.0 $\pm$ 2.3) nm respectively.

The deviation from the linear slope for the metasurfaces immersed in solvents increased slightly to $\pm$ 9 nm (blue and green lines), most probably due to instabilities in the flexible PDMS-glass cavity on top of the metasurfaces upon moving the stage.

The sensitivity, Se, is defined as the wavelength shift of the resonant dip per refractive index unit change and measured in nm/RIU:

$$Se = \frac{\Delta\lambda}{\Delta n} \qquad\qquad (5.1)$$
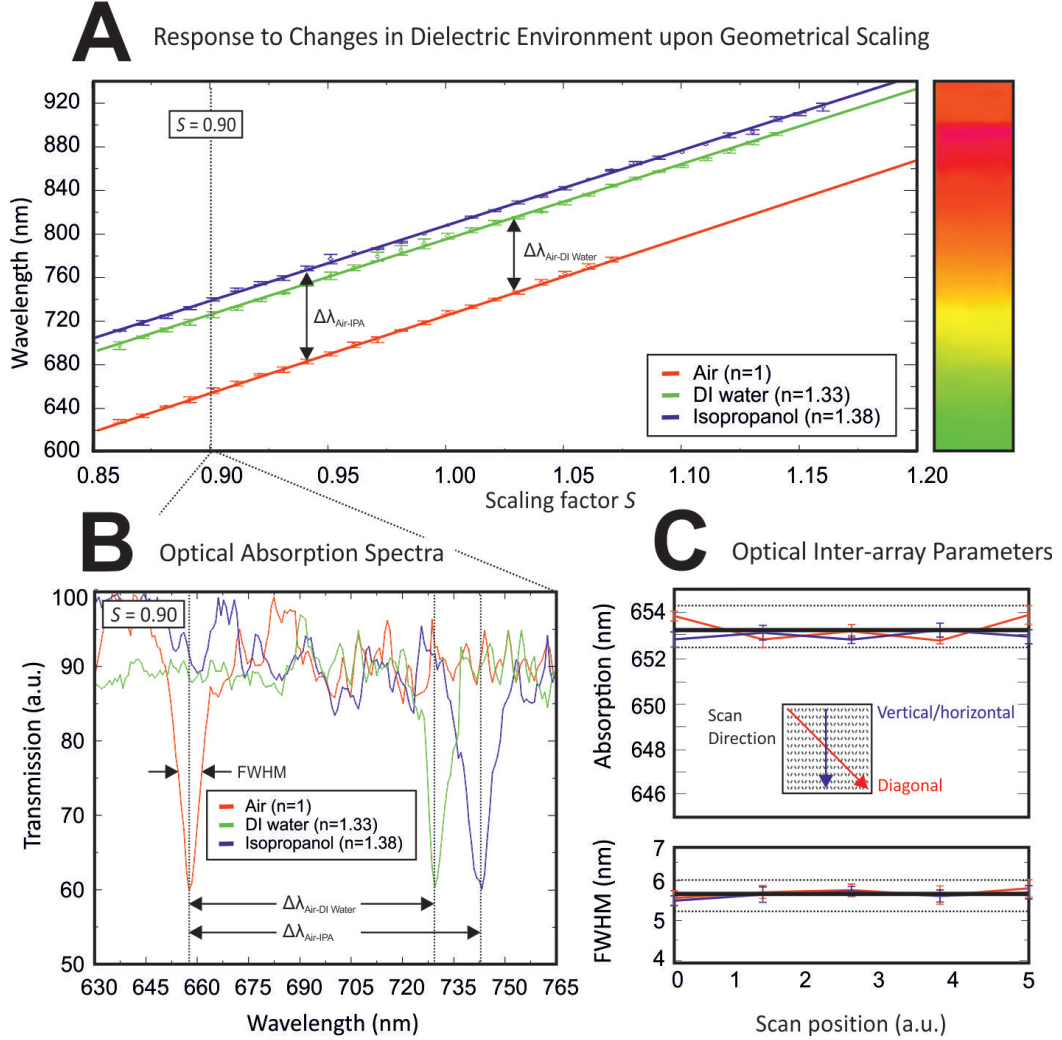
FIGURE 5.3: Optical characterization of metasurfaces under geometrical and dielectric environment changes: (A) Scaling behavior of the resonance position as a function of *S* (varied from 0.85 to 1.20) and dielectric environment (air, DI water and isopropanol). (B) Spectral absorption data for air (red data), DI water (green data), and isopropanol (blue data) as surrounding medium, exemplarily for *S* = 0.9. (C) Inter-array uniformity of the absorption resonance positions (top) and FWHMs (bottom) along vertical/horizontal (blue data) and diagonal (red data) line scans.

while the figure of merit, FOM, value, useful to quantify and compare the optical response to dielectric changes, is calculated as the ratio of the refractive index sensitivity to the full-width at half-maximum (FWHM) of the corresponding resonance:

$$FOM = \frac{Se}{FWHM} \tag{5.2}$$

The following table shows a schematic of the obtained results:

	Δλ (nm)	Δn	FWHM (nm)	S (nm/RIU)	FOM
Air / DI Water	69. 7	0.33	6.5	211	32.5
Air / IPA	82.7	0.38	6.7	218	32.5
DI Water / IPA	13.0	0.05	6.4	260	40.6

FIGURE 5.4: Table schematizing the sensitivity, *Se*, and the figure of merit, FOM, values obtained from the experimental results for air, DI water, and IPA.

Moreover, similarly to the SEM metrology, the optical assessment of the interarray uniformity revealed very low variations in positions of the optical absorption resonances ($\pm$ 1.0 nm) and the FWHMs ($\pm$ 0.3 nm) across the entire array, as displayed in Figure 5.3 C.

5.3.3 Sensitivity towards changes in NaCl concentration

Further experiments were performed by using different NaCl concentrations in DI Water. This is a good preliminary test since, if the responses result repeatable and show good sensitivity, makes the metasurfaces a good candidate for biosensing applications.
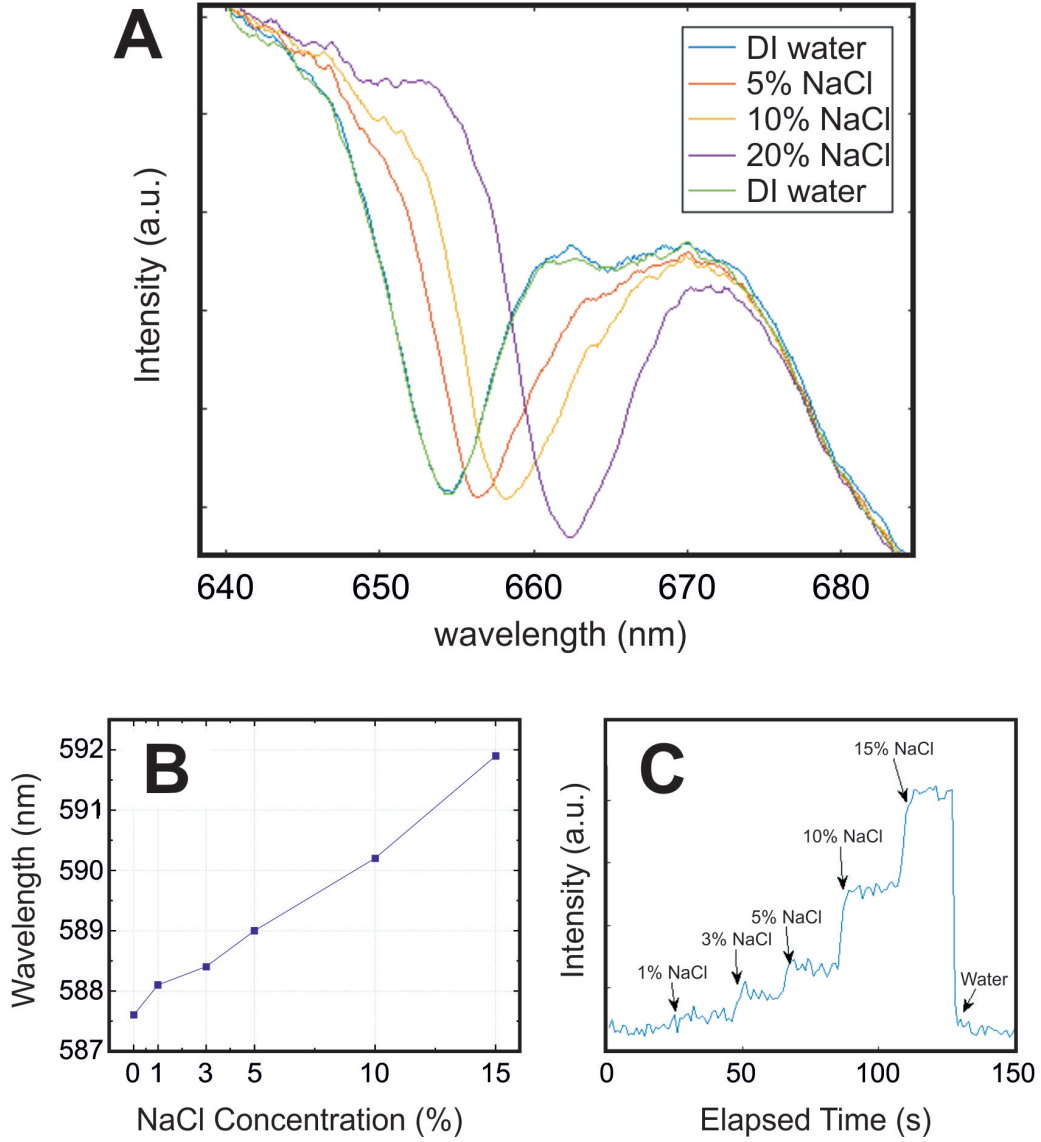
FIGURE 5.5: Experimental detection of NaCl concentrations. (A) Metasurface transmittance spectra for DI water and NaCl different concentrations, with n ranging from 1.32 up to 1.36. Spectral sensitivity of around 423 nm/RIU is measured. (B) Metasurface resonance position for different NaCl concentrations. (C) Time dependency of the signal at different NaCl concentrations.

The spectral characterization of the metasurface sensing device was performed for DI water (n=1.331) and water with different concentrations (% w/v) of NaCl salt, with n ranging like this:

- 0%: 1.332, $\Delta n = 0.001$

- 5%: 1.342 $\Delta n = 0.011$

- 10%: 1.346 $\Delta n = 0.015$

- 20%: 1.361 $\Delta n = 0.030$

to demonstrate the frequency shift of the transmittance peak (Figure 5.5 A). The measured transmittance peak shifted towards higher wavelengths with the increase of NaCl concentration (% w/v), which corresponds to a higher refractive index. This result is coherent with the ones obtained in Section 5.3.2, and also the behavior of the characteristic results linear (Figure 5.5 B) like the one shown previously. Moreover, as can be seen in Figure 5.5 C, the response time of the measurement is very fast and the signal remains constant in the exposure time slot.

From this measurement, considering the scaling factor $S = 0.9$, a sensitivity of around 769 nm/RIU and FOM of 85 was calculated.

NaCl concentration	0%	5%	10%	20%
Resonance peak position for s = 0.9	723,8 nm	732,0 nm	741,5 nm	746,1 nm

These results show that the measurement of a single wavelength using metasurface-based dielectric sensing offers enormous potential. This technology offers high sensitivity and high-speed measurements, together with affordable, small, and integrable components, making this technique performance-competitive.

5.4 Conclusion

This chapter presented an insight into dielectric metasurface sensitivity towards changes of different features, starting with a general introduction to dielectric metasurfaces tunability, which can be performed varying different features, starting from the geometry, then the surrounding environment changes up to the change of the metasurface material himself. After, a deeper analysis of the results obtained in the research project was given. Here, first, the sensitivity towards geometrical changes was shown, where a linear resonance behavior with respect to the linear scaling was demonstrated. Then, the sensitivity to dielectric environment changes was shown. Here, the focus was put on two different analytes, DI water, and isopropanol, together with air measurements. The dielectric metasurface here was able to show a sensitivity of around 215 nm/RIU and a FOM of around 32.5. But, more interestingly, the sensitivity towards changes in NaCl concentration was analyzed, showing a sensitivity of around 769 nm/RIU and a FOM of 85, which is a promising result for biosensing applications.

Then, in general, the demonstrated all-dielectric metasurfaces show spectrally selective resonances that can be tuned by scaling the meta-atom unit cell from one array to another. With a narrow spectral linewidth, such ultrahigh-sensitive dielectric nanoresonators could be used for practical sensing applications and improve detection limits. Furthermore, such a low-loss all-dielectric platform allows for the avoidance of photothermal degradation and enables highly effective and feasible optical sensors for biomedical applications. This high-Q metasurface design has great potential for ultrasensitive and label-free chemical fingerprint detection of various analytes and molecules, some of which will be tested in the next chapter.

Chapter 6

Sensing Experiments

6.1 Introduction

In the area of metasurfaces and nanoantennas, high-index all-dielectric resonant nanostructures like silicon nanoparticles received a lot of scientific interest recently[192,37,89,84,172]. Furthermore, robust and customizable resonance properties as well as tuneability have been demonstrated for silicon nanostructures[148,135]. As a result, such dielectric nanostructures hold exciting potential for biosensing applications by promising light to be manipulated at the nanometer scale with high flexibility and efficiency[17]. Dielectric silicon nanostructures have two significant advantages over their metallic counterparts. First, silicon overcomes the issue of local heating by having a significantly lower absorption loss in the optical spectrum area[23]. Second, compared to plasmonic nanoparticle resonances, dielectric nanoparticle resonances can reach a higher quality factor due to the low losses, leading to increased sensitivity[37]. In fact, sensitivities similar to LSPR sensors have been achieved in refractive-index sensing utilizing dielectric nanoparticles with high quality factor Fano resonances[171].

The significance of ultra-thin layers for biosensing is likewise debatable, because dielectric nanostructures' resonant electromagnetic modes are not as effectively limited at the surface similarly to the plasmonic equivalents. In fact, the vast spatial extent of the modes[18] is helpful for refractive-index

detection[171], leading to great sensitivity. But in biosensing, the analytes are often restricted to a very thin (typically tens of nm) layer at the nanostructures' surface, thus only this area has to have electromagnetic fields amplified. As a result, it's critical to choose the proper resonance modes for dielectric biosensors that may provide significant field amplification at the nanoresonator surface.

Notably, it is critical to design adequate surface functionalization procedures for sensing applications that allow selective binding of the target analytes. Furthermore, the coated layers must be highly stable throughout time and multiple washing operations.

Here, a three-step surface functionalization strategy will be first described, followed by an insight in an application: a standard Biotin-Streptavidin binding response. Here, the detection of molecules will be performed by employing dielectric detection systems previously described based on localized resonance shift.

6.2   Surface Engineering

Both the composition and the chemical nature of the interface are crucial for physical properties and chemical reactions at phase boundaries. As a result, various surface coatings have been created and optimized for a wide range of applications, from medical, such as antimicrobial coatings for implants[169], via low-friction surfaces in engines[36], to analyte-specific coatings of biosensors[77,162].

Compact molecular monolayers that fine-tune the surface's characteristics using minuscule quantities of material make up attractive surface coatings. These surface engineering techniques frequently use bifunctional molecules[158,28], interlinking two moieties:

- a surface-anchoring group (comprising eventually a molecular backbone), and

- a mutable head with the functionality of interest to be exposed on the surface.

For specific applications, a wide range of surface properties has been produced, including wettability[94], catalytic activity[123], interactions with analytes[152], single charge transport layers[20], thin film transistors[194], molecular field-effect devices[109], etc. The wide spectrum of materials used includes metals, metal alloys, semiconductors, and different metal-oxides.
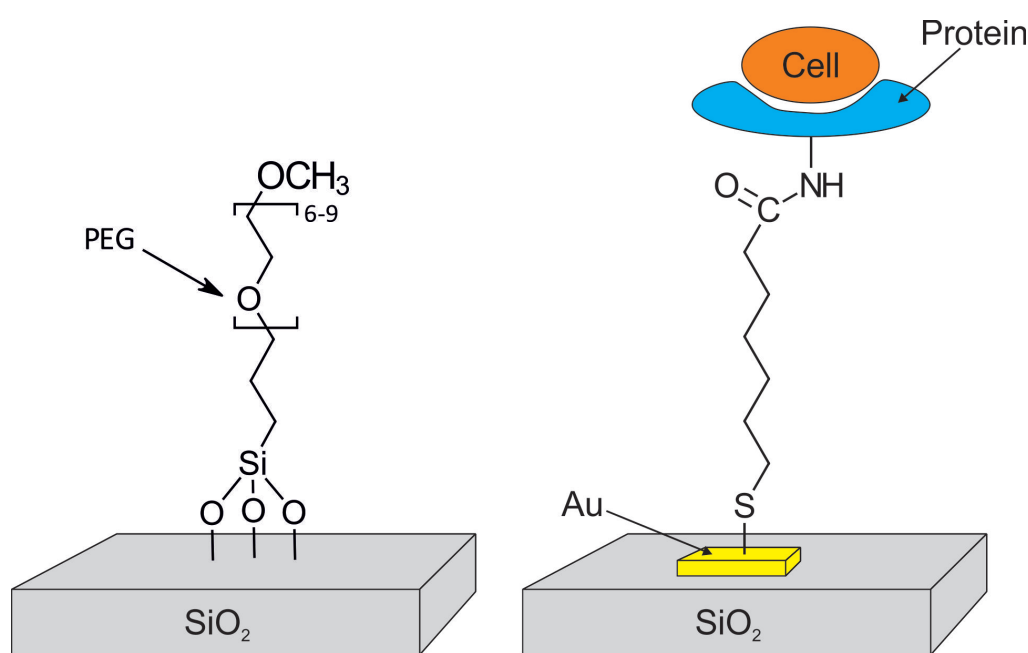
FIGURE 6.1: Example of surface modifications. A schematic illustration of a PEG surface chemistry for solid silicon substrates (left) also silicon substrates with gold patterns for site-selective cell adhesion by material contrast (right). Adapted from ref. [90].

The most often used ones include:

- gold surfaces because of the inherent affinity to bind thiols, allowing self-assembled monolayers (SAMs) to be formed[159], and

- silicon surfaces because of their crucial significance in complementary metal-oxide-semiconductor (CMOS) technology[163].

An example is shown in Figure 6.1. While the functionalization of both types of surfaces is based on chemisorption and the creation of chemical bonds between the substrate and the coating layer, the formation process and the nature of the resulting coating layers are very different:

- Gold surface decoration is a dynamic process. On gold, the mobility of the immobilized molecule on the surface necessary to create densely packed, self-assembling monolayers (SAM) is made possible by the balanced strength of the sulfur-gold bond. Even tiny gold clusters can disperse over the surface of amorphous and polycrystalline gold, affecting to the coating's density and defect level.

- On the other side, the silicon-oxygen connection created at the silicon surface during silanization is too strong to exhibit reversibility surface construction. The absence of spontaneous surface reconstructions in the silicon lattice is, however, an additional benefit. As a result, the molecules do not need to undergo any additional rearrangement procedure in order to achieve the optimal packing density and homogeneity; the molecules are pinned where they first touched the surface. As a result, compared to their Au counterparts, the Si coatings produced are often less homogeneous but - as a consequence - more durable.

Because of the differing surface reactivities of the two surfaces, distinct immobilization techniques produced libraries of molecules for molecular functionalization which are, however, incompatible with one another.

Numerous sensing concepts that take advantage of thiol-immobilized molecules used as analyte-specific interfaces have been developed thanks to the reliable immobilization of molecules exposing a sulfhydryl group on a gold surface as well as advantageous material properties of Au, like accessibility to nanostructures and nanoparticles, high electrical and thermal conductivity, beneficial optical properties like transparency, and high plasmonic

activity[127,73]. As a result, there is now a large and varied library of receptor architectures, e.g., for biomolecules, that expose sulfhydryls as anchor groups.

However, gold is a undesired element in the CMOS industry due to its high diffusibility and behavior as a deleterious dopant when embodied in silicon[178,132]. With CMOS miniaturization and the increasing complexity of mobile devices, sensing modalities will soon be introduced and gold will no longer be available as an interfacial material, necessitating novel immobilization concepts on Si or SiO_2. As a result, while using existing sulfhydryl-decorated compounds produced for Au-based devices is intriguing due to the previously described diversity of established and mature concepts, it is also hard due to synthetic reasons.

6.3 Results

6.3.1 Three-Step Immobilization Strategy

Parts of this section are adapted from one submitted article: D. Vogel, G. Prone, D. Scherrer, E. Lörtscher, and M. Mayor "A Universal Three-Step Immobilization Strategy for Thiols on Silicon Surfaces"

A simple and generic three-step coupling protocol for the immobilization of thiols on Si surfaces is presented.

The thus discovered immobilization approach for thiols on Si surfaces, as seen in Figure 6.2, is based on linker molecules and composed of three major steps:

- an inert 2-(methylthio)benzothiazole is adhered to the Si surface;

- the 2-(methylsulfonyl)benzothiazole, which has strong electrophilic properties, is then formed by oxidizing the 2-(methylthio)benzothiazole;

- the methylsulfonyl component is effectively replaced by the nucleophilic thiol, leading to the covalent attachment of the sulfhydryl-exposing derivative to the surfaces.
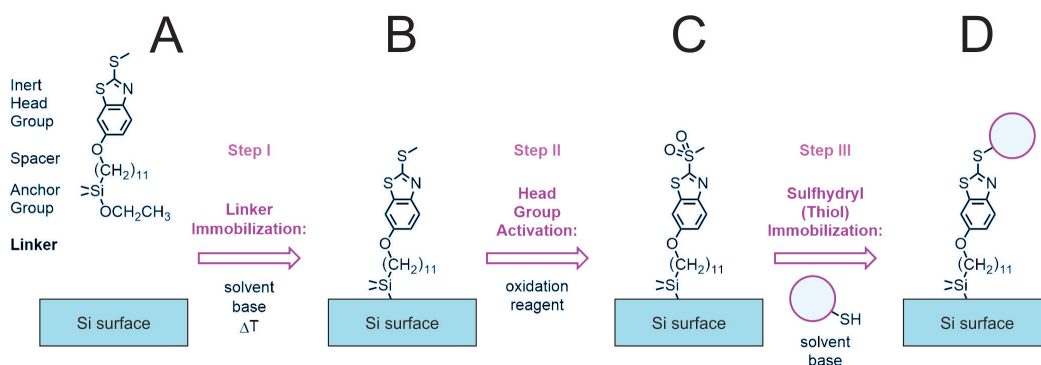

FIGURE 6.2: Thiol immobilization technique on Si surfaces. The linker structure is initially immobilized on the (previously oxidatively cleaned) Si surface, coupling a terminal dimethylethoxysilane anchor group with a 2-(methylthio)benzothiazole subunit at the opposite end. The exposed 2-(methylthio)benzothiazole is oxidized to the electrophilic 2-(methylsulfonyl)benzothiazole in the second activation phase. In the last phase, the thiol-exposing molecule (big dot with -SH terminal) undergoes a nucleophilic substitution reaction with the exposed 2-(methylsulfonyl)benzothiazole, attaching the thiol compound covalently to the Si surface.

The linker molecule was synthesized by David Vogel, PhD student at the University of Basel in the Marcel Mayor group.

Anchor Group

Dimethylethoxysilane was chosen as the anchor group to promote the production of molecular monolayers on the silicon surface[187]. While the alternative triethoxysilane would most likely result in thicker and more robust coatings, it was presumed that the cross-linked polymer nature of the coating would result in head groups hidden within the branched polymer coating, making them less accessible for successive wet chemical processing. The possible lability of the linker-coated surface when subjected to nucleophilic solvents such as water or alcohol was also evaluated. Such solvents may

substitute the linker molecule at the surface after penetrating the molecular monolayer and interacting with the anchor structure, reducing functionality.

Spacer

An eleven-carbon long alkyl chain was used as a spacer to limit the likelihood of polar solvent molecules reaching the anchoring group of the linker. The goal was to keep polar solvent molecules away from the linker's anchor by including a hydrophobic section in the coating as a blocking layer.

Molecule Immobilization and Characterization

The immobilization of the linker molecules on the Si surface was explored. A thin layer of linkers was formed on the silicon oxide surface (Figure 6.2 B) after drop casting a solution having a concentration of 1 mM of linker onto a silicon wafer, pre-heated to 90 °C. Two separate techniques were used for the study and characterization of the formed layer:

- X-ray photoelectron spectroscopy (XPS) for the analysis of the wafers' chemical composition, and

- contact-angle goniometry for the analysis of the wafers' surface characteristics.

These techniques will be explained in more depth later in the Experimental Section.

It is important to note that the analysis was limited to these two strategies in order to provide proof of concept for the immobilization strategy. This because, due to the small dimensions, the molecules do not provide sufficient dielectric contrast to be sensed by the metasurface's resonances. Larger molecules (like biomolecules) are required.

One wafer, identified as *Blank Si*, was treated using the same procedure but without linker molecules in the coating solution. Figure 6.3 shows the measured contact angles performed with DI water. After immobilization of the
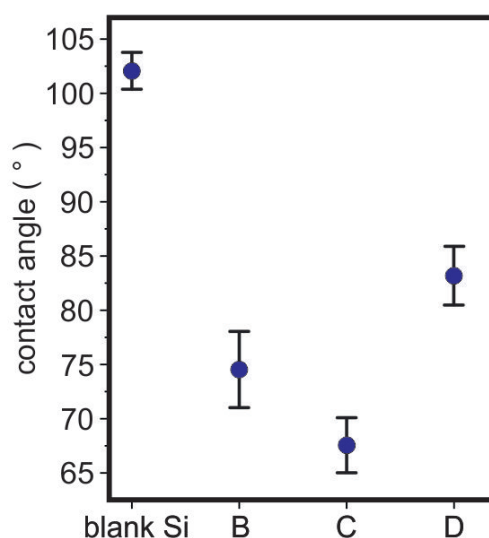
FIGURE 6.3: Contact angles were measured for monocrystalline Si surfaces exposed to the reaction conditions shown in Figure 6.2. Each value was obtained by probing six different spots on four distinct silicon wafers. Referring to the labels in Figure 6.2, the recorded values are: $(102.1 \pm 1.7)°$ for ***Blank Si***, $(74.5 \pm 3.5)°$ for B, $(67.5 \pm 2.5)°$ for C, and $(83.2 \pm 2.7)°$ for D.

linker molecule, the silicon wafer's measured contact angle shifts from $(102.1 \pm 1.7)°$ for the reference ***Blank Si*** to $(74.5 \pm 3.5)°$ for Figure 6.2 B. Repeated measurements taken at various locations on the wafer surface with a pronounced contact angle difference of $(27.6 \pm 3.9)°$ indicate that a compact and uniform layer of the linker molecule has formed.

The linker-coated wafer was soaked overnight in a 0.1 M mCPBA solution in DMF to activate the surface coating's head group by oxidizing the methylthio functional group. After washing with DMF, acetone, and DCM, the wafer was dried in vacuum and then with an argon stream to remove solvent residues. The contact angle recorded for the activated wafer in Figure 6.2 C was $(67.5 \pm 2.5)°$, which was approximately $7°$ less than the contact angle reported for the linker coated wafer (Figure 6.2 B). As the polarity of the exposed structure increased due to the oxidation stage, the contact angle decreased, as expected for a more hydrophilic surface.

The activated wafer was then exposed to the thiol-immobilization conditions. There are different reasons why this particular thiol (3,3,3-trifluoropropylmercaptane) was chosen:

- for the XPS experiment, fluorine atoms operate as labels since their signals appear in the XPS spectra in a region that is not covered by any other non-metallic elements and are therefore simple to distinguish (highlighted by a green background in Figure 6.4 A);

- it is compact, which is a benefit for XPS analysis and enables X-ray penetration deep enough to discover the molecular structure's composition;

- it is very volatile and soluble in the majority of organic solvents, making it easier to remove any unreacted species from the surface following the immobilization process. This is a crucial feature to prevent additional signals from being produced by purely physisorbed species in the surface analysis.

The activated precursor wafer (Figure 6.2 C) was then treated with the thiol molecule in DMF overnight. DMF, acetone, and DCM were used to wash the wafer. The remaining solvents were then removed from the wafer by vacuum exposure and argon blow drying.

Contact Angle Analysis: The thiol-functionalized wafer (Figure 6.2 D) shown a contact angle of $(83 \pm 22.7)°$ that was significantly greater than the activated precursor wafer's. The increase of $16.7°$ was expected because, in Step III, the more hydrophobic thiol group (trifluoropropylthiol) should replace the polar and hydrophilic methylsulfonyl group on the activated precursor wafer. Moreover, since the trifluoropropyl chain exposed at the surface is more hydrophobic than the methyl group of the linker (Figure 6.2 A), it was also expected that the recorded contact angle of the thiol-functionalized wafer would be bigger (of around $8.7°$) than that of the linker decorated wafer.
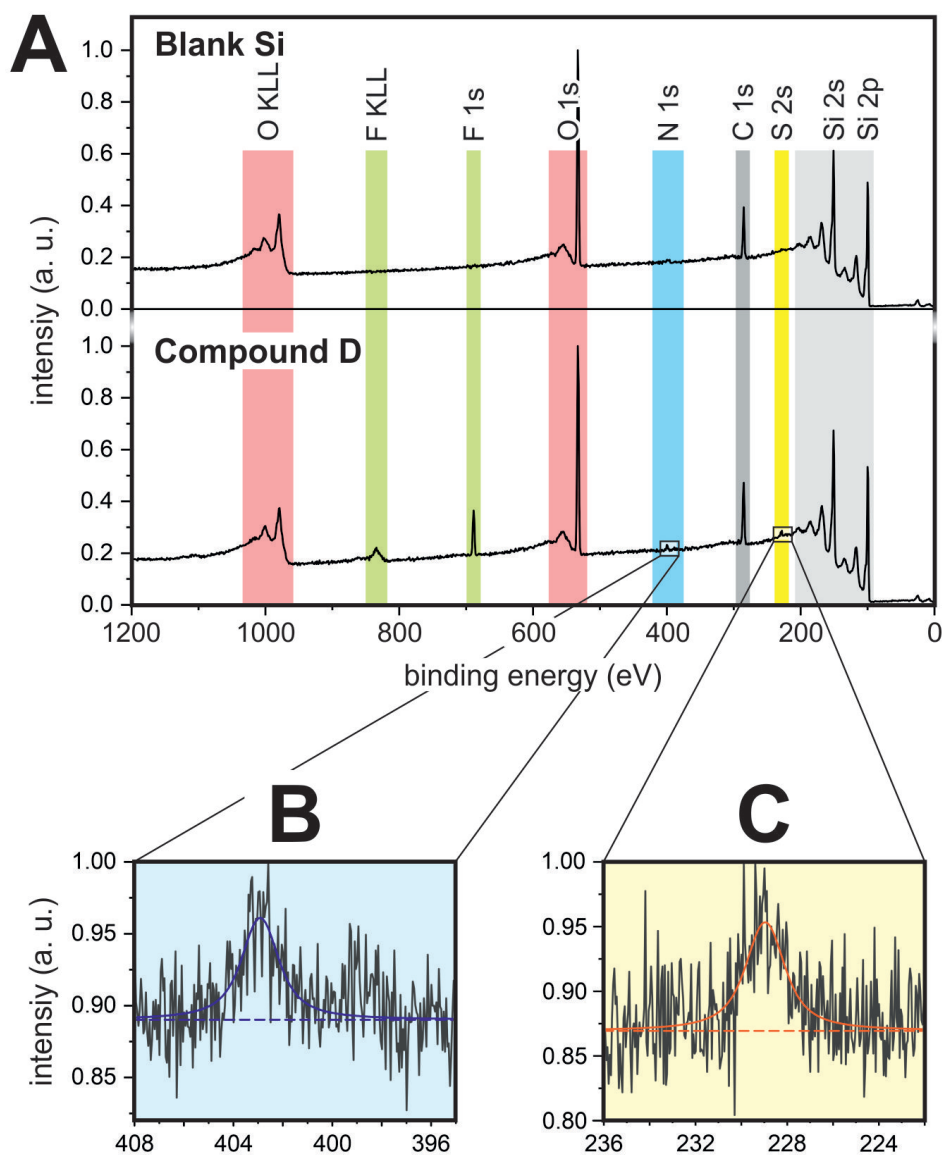
FIGURE 6.4: (A) XPS survey spectra of naked wafer **Blank Si** and thiol-functionalized wafer D. A colored background highlights the binding energy regions of interest, which are labeled by the transitions recorded in these regions. (B) and (C) show the core level spectra of the N1 s and S2 s regions, which correspond to the faded signal marked in blue and yellow in the survey spectra of the thiol-functionalized wafer D. The solid lines (blue for N1 s and red for S2 s) correspond to the calculated chemical states at 403 eV for N1 s and 229 eV for S2 s. The computed Shirley or Tougaard background is represented by the dashed line.

XPS Analysis: While the contact-angle study supported the suggested on-surface alterations, XPS investigations can offer more information about the coatings' composition. Figure 6.4 A shows the survey XPS spectra of the reference wafer ***Blank Si*** and the thiol-immobilized wafer D. The XPS spectra show strong silicon peaks between 90 and 200 eV corresponding to the silicon substrate and all silicon species contained within the penetration depth of the XPS device, which is approximately 5 nm. This is expected for monocrystalline silicon surfaces coated with a naturally grown silica layer and capped by a thin organic layer (light grey background in Figure 6.4 A). Additionally, the signals for carbon (dark grey background) and oxygen (red background) are clearly visible on both wafers . It appears that the wet chemical treatment of the reference wafer (***Blank Si***) deposits a substantial number of organic species despite the lack of a linker molecule. The chemical changes from the ***Blank Si*** non-functionalized wafer to the linker-coated wafer ***B*** and to the activated coating of ***C*** cannot be investigated or confirmed using the XPS spectra. The very faint peaks attributed to N 1s and S 2s are the only other signals (Figure 6.4 B and C). Unfortunately, the dominating silicon signals cover the region of the more pronounced and distinctive sulfur S $2p^{1/2}$-$2p^{3/2}$ signals (164-165 eV), making it impossible to see[113]. The XPS spectra are excellently suited to corroborate the whole transformation from the non-functionalized wafer (***Blank Si***) to the thiol-decorated wafer ***D*** because of the fluorine labels added during the thiol-immobilization step. Only in the XPS spectrum of ***D*** does the fluorine signal appear, revealing the immobilized thiol. It is remarkable that the thiol-immobilization conditions also produce a weak fluorine signal when applied to the reference wafer (***Blank Si***) without an immobilized linker. However, the recorded signal is significantly weaker and not similar to that for the thiol-functionalized wafer D. However, it does show that despite cleaning procedures, fluorinated species were still present on the surface of the blank wafer. While the activated linker-exposed wafers were successful in retaining the thiol molecule by creating a covalent bond, the nature of the interaction on the reference wafer (***Blank Si***) is less obvious.

Bromine Label

The success of the thiol-immobilization and the potential of the immobilization strategy are documented by the stepwise evolution of the recorded contact angles and the overall transformation, which is supported by XPS analyses. However, the absence of interpretable XPS data for each individual transformation on the wafer was unsatisfactory. The immobilized thiol's presence was demonstrated with the use of a halide label, therefore the linker molecule's presence will be shown with the same method. To demonstrate surface immobilization, in addition to the previously presented linker molecule, David Vogel synthesized a new brominated version of it, to be able to use XPS with the help of a new label. The bromine was located at position 7, which was both far enough from the reactive site to prevent interfering with the intended chemical transformations, and exposed enough to be identified by the XPS analysis. The novel bromine linker was subjected to the same linker immobilization, head group activation, and thiol-immobilization conditions as those previously employed.
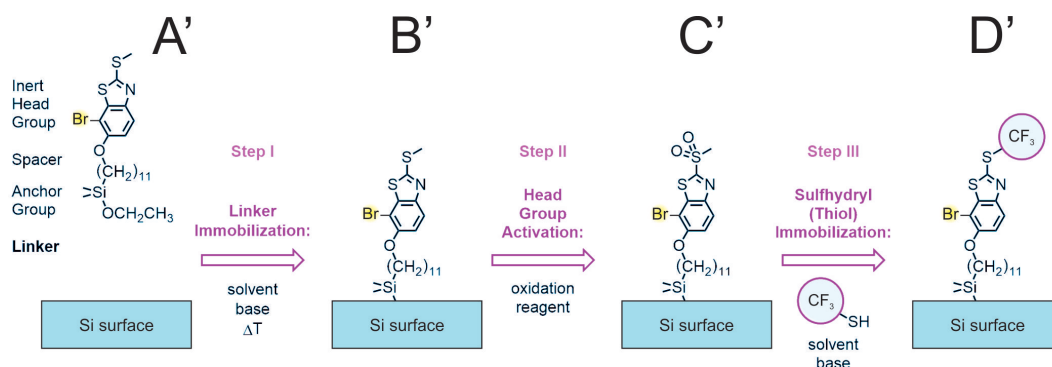

FIGURE 6.5: Immobilization strategy for the brominated thiols on Si surfaces

Contact Angle Analysis: Figure 6.6 shows the contact angles that were recorded for the obtained wafers **B'**, **C'**, and **D'**. During the functionalization processes, the contact angle developed in a very same way. The contact

angle for **B'** decreases to $(86.3 \pm 3.1)°$ upon immobilization of the brominated linker. The wafer becomes even more hydrophilic after activation, with a contact angle of $(76.9 \pm 4.8)°$ for **C'**. The surface becomes less hydrophilic following the final thiol immobilization, as seen by the increased contact angle of $(89.4 \pm 2.0)°$. In general, the contact angles recorded after the different stages of the procedure for the new linker are 6° - 12° higher than the ones discussed previously for the first linker. This is due to the slightly greater hydrophobicity of the new linker's brominated head group. The similarity in contact angles reported at different stages of the immobilization process with both the first and brominated linkers indicates that the surface chemistry is extremely similar in both situations.
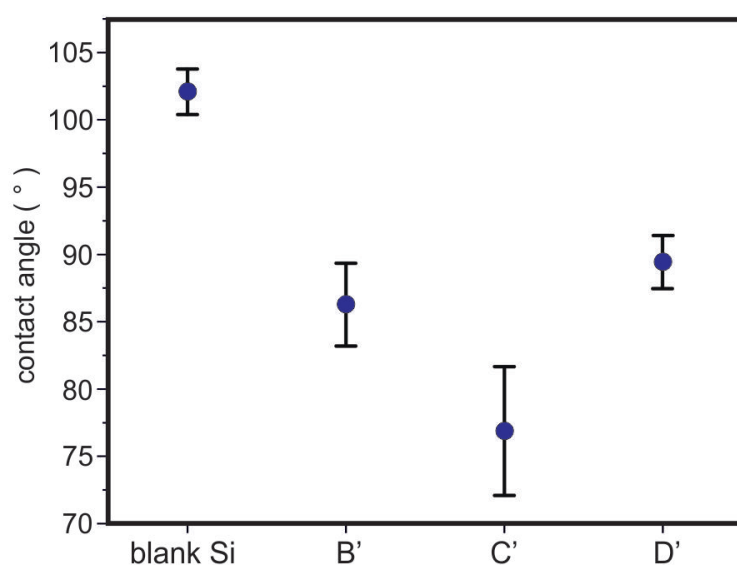

FIGURE 6.6: Contact angles measured on wafers exposed to the reaction conditions. Six spots at various sites on four individually produced silicon wafers were probed to obtain each value. The recorded values are: $(102.1 \pm 1.7)°$ for **Blank Si**, $(86.3 \pm 3.1)°$ for **B'**, $(76.9 \pm 4.8)°$ for **C'**, and $(89.4 \pm 2.0)°$ for **D'**

XPS Analysis: The XPS analyses performed on wafers treated with the brominated linker are very interesting (Figures 6.7 A and B). In fact, the immobilization of the linker results in the observation of a discernible Br 3d signal as a $3d^{3/2}$ - $3d^{5/2}$ doublet separated by 0.66 eV. The visibility of the bromine signal is enhanced by the lack of any other signals in the energy region, which

enables its integration to calculate the relative coating densities of the individual species. No notable changes in the XPS spectra of either sample are seen after the linker-decorated wafer **B′** is oxidized to the activated wafer **C′**. This was expected since the two extra oxygen atoms in the two organic coatings constitute the only difference between them, and the excessive oxygen signatures of the silica coating obscure their signals. On the other hand, the Br 3d signal is still present in equivalent intensity in the XPS spectrum of **C′**, indicating that the coating is stable under the current oxidation conditions. This is because washing away the linker molecules would reduce the intensity of the bromine signal. Finally, **D′** was produced by subjecting the activated wafer **C′** to the thiol-immobilization process. The fluorine signals of the immobilized thiol are clearly evident in the XPS spectrum. The Br 3d signal likewise remains at comparable levels for the thiol-decorated wafer **D′**, indicating that the coating is equally resistant to these reaction conditions. This is particularly interesting since the immobilized anchoring group's silicon atom may also be attacked by the sulfhydryl group, which would liberate the linker molecule.

Thiol-immobilization Quantification

Two alternative methods, shown in Figure 6.8, were used to produce wafers exposing the thiol-decorated linker in order to enable the direct quantification of the thiol-immobilization by XPS:

a) the previously mentioned thiol-immobilizing reaction process; and

b) direct immobilization of a synthesized molecular compound equal to the one expected at the end of the immobilization process on the wafer.

The two thiol-functionalized wafers were analyzed and compared.

Contact Angle Analysis: a) and b) final compounds had fairly similar measured contact angles of $(89.4 \pm 2.0)°$ and $(89.6 \pm 1.3)°$, respectively (Figure 6.8 B). As expected, similar contact angle values for these wafer sets were
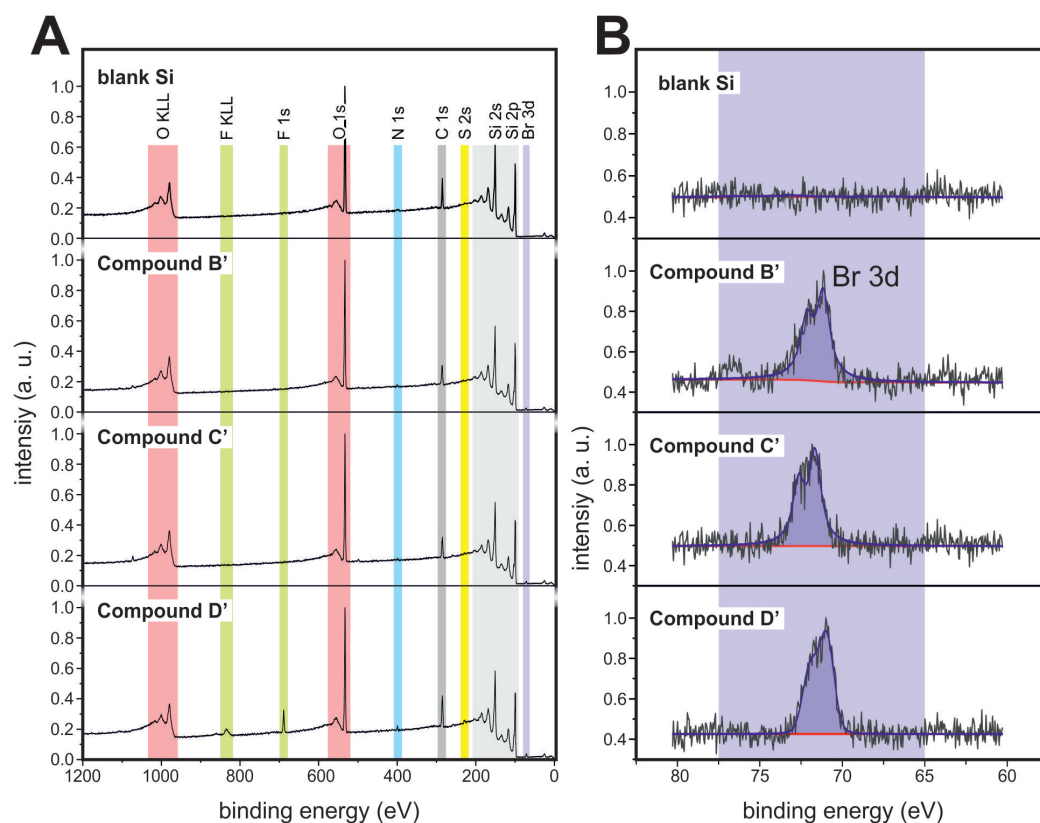
FIGURE 6.7: (A) XPS spectra of naked wafer *Blank Si* and wafers *B′*, *C′*, and *D′*. The transitions recorded in the relevant binding energy ranges are indicated, and the locations are highlighted with a colored background. A light purple backdrop highlights the Br 3d signal (70–73 eV), and the associated core level spectra are shown in (B).
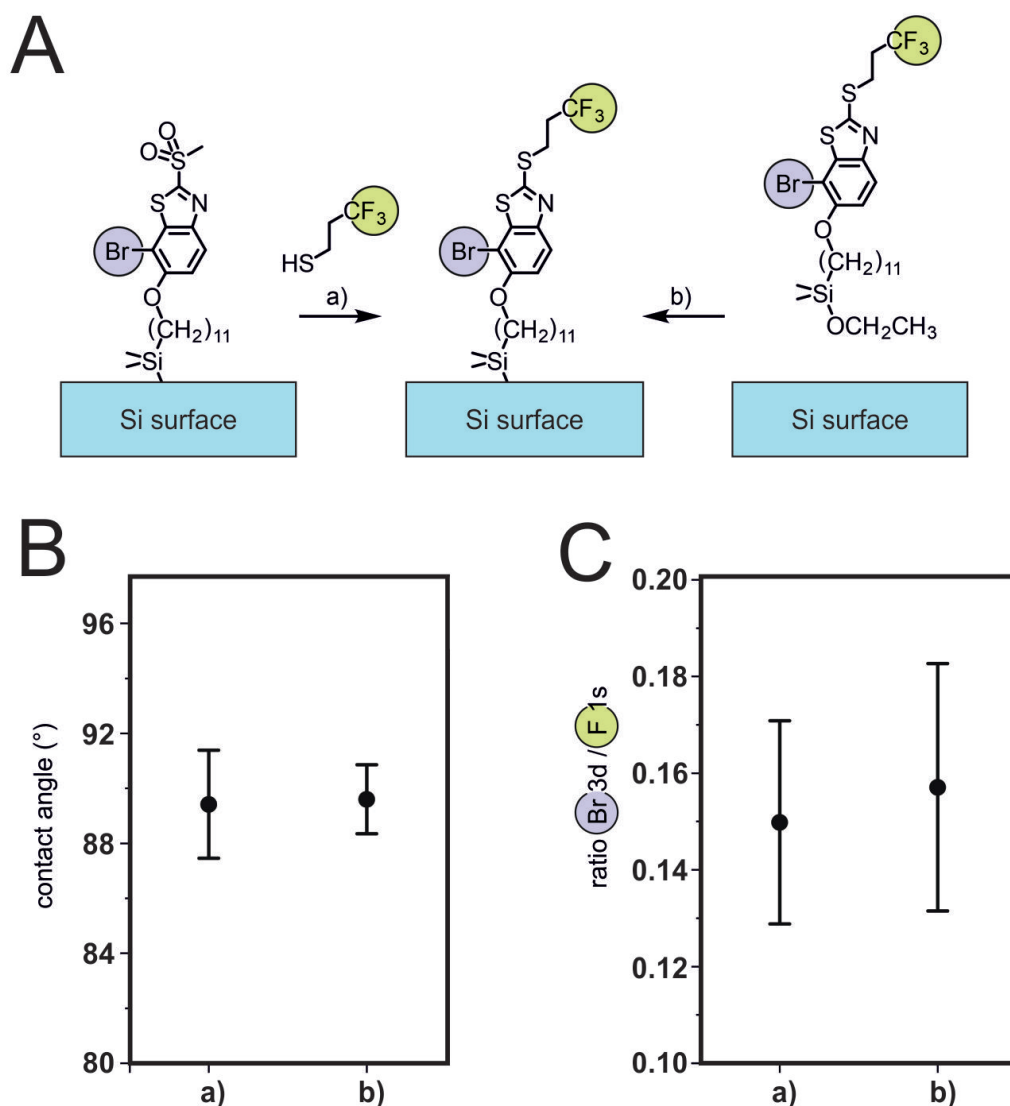
FIGURE 6.8: A) Two distinct methods to produce wafers exhibiting the linker coated with thiol. a) The activated wafer **C′** underwent a thiol-immobilizing process, producing **D′**. b) The custom-made compound is immobilized on the wafer, serving as a reference for a quantitative thiol-immobilizing reaction. (B) Analysis of the final results from (a) and (b) using contact angle goniometry. The values were all gathered by probing four independently made silicon wafers at six different locations. The measurements are $(89.4 \pm 2.0)°$ for a) and $(89.6 \pm 1.3)°$ for b). (C) Ratio between the surface areas of the Br 3d and F 1s peaks in the XPS spectra of data from (a) and (b). The error bars show values that deviate by no more than one standard deviation from the average.

found, supporting the idea that the two methods produced similar surface coatings.

XPS Analysis: The comparison of the XPS spectra produced for the two sets of wafers was particularly interesting. The Br 3d signal was used to identify the linker's head group, while the F 1s peak was used to identify the immobilized thiol. The ratio of the Br 3d peak to the F 1s peak allows to calculate the concentration of the thiol molecule in relation to the available linker molecules in the coating, and hence the success of the thiol-immobilization technique (Figure 6.8 C). The XPS data support the conclusion obtained from the contact angle goniometric investigations, namely that the two coatings are the same within the analytical methods' precision. As a result, the on-surface modifications that occur during linker activation and subsequent thiol-immobilization must be quantitative.

Experimental Section

Water contact angle measurements: The contact angle measurements were carried out using Milli-Q water (2μl droplets). A Krüss FM40 EasyDrop Machine was used to record the drops. Drop Shape Analysis software for Windows from Krüss was used to analyze the droplets. Only images with a focus assistant value greater than 90 were evaluated for contact angle measurements. Six measurements were taken for each sample. The droplets were placed as follows throughout the wafer: one in each corner, one in the center, and one between the edge and the center. The error bars reflect values that are within one standard deviation of the mean.

XPS measurements: The prepared wafers were dried on a Schlenk line under a vacuum of $1 \cdot 10^{-2}$ mbar for 18 h and thereafter moved into an ultra-high vacuum (UHV) XPS chamber without breaking the vacuum. The pressure in the XPS chamber was kept in the range of $\sim 2 - 4 \cdot 10^{-9}$ mbar. A monochromatic Al-Kα X-ray source ($h\nu$ = 1486.6 eV) and a photoelectron spectroscopy analyzer (VG ESCALAB 210) with an energy resolution of 0.5 eV at 20 eV pass

energy were installed in the UHV chamber. Surveys and high-resolution core level spectra were measured using 10 scans at a pass energy of 100 eV and 60 scans at a pass energy of 20 eV, respectively. The Au $4f^{7/2}$ peak was calibrated with an electron binding energy (BE) of 84 eV. After a Shirley background subtraction, the core level lines were fitted using DoniachSunjic functions using the UNIFIT for Windows (Version 2015) program[41,140,62].

6.3.2 Biotin-Streptavidin Binding Response

Utilizing the arrays of silicon nano-ellipses that were previously described, experimental biosensing is here demonstrated using biotin and streptavidin, a high-affinity vitamin-protein complex pair that is frequently utilized in biosensing research[43]. Here, using the metasurface chip coated with biotin, a streptavidin concentration of 10^{-7} M was measured. It was demonstrated that simple resonant dielectric structures can act as an innovative platform for reliable biosensing and recognition of label-free analytes at small concentrations in the near-infrared wavelength range. This is accomplished by merging the powerful Mie-type magnetic resonances[88,45], which are optically-induced, with the tunability of silicon nano-ellipses[30].

As a proof-of-concept for the streptavidin proteins' detection, Figure 6.9 depicts the schematic of the biosensing procedure. The bio-recognition linker molecules are coated on the silicon nano-ellipses array (blue/green block), which serves as a sensor. The linker molecules are subsequently attached to the target proteins, the streptavidin. The spectra are collected for the spectral shift analysis once the measurement is completed (red arrow).

Surface Functionalization

More specifically, there are three steps in this biosensing procedure (Figure 6.10): surface activation (1.), linker functionalization (2.), and streptavidin binding (3.).
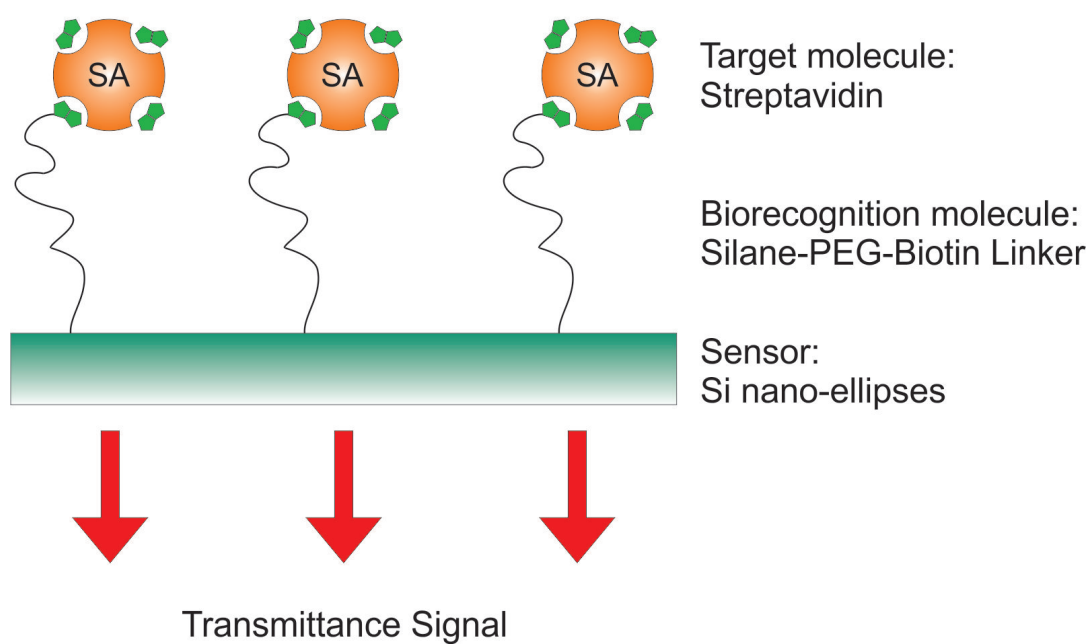
FIGURE 6.9: Schematic for biosensing measurement. The silicon ellipses sensor is coated by physisorption with linker molecules. The biotin moiety of the linker molecules is linked to the target streptavidin proteins (orange circles). For spectral shift analysis, transmittance spectroscopy is used (arrows), and spectra are gathered.

1.) Surface Activation

2.) Linker Functionalization
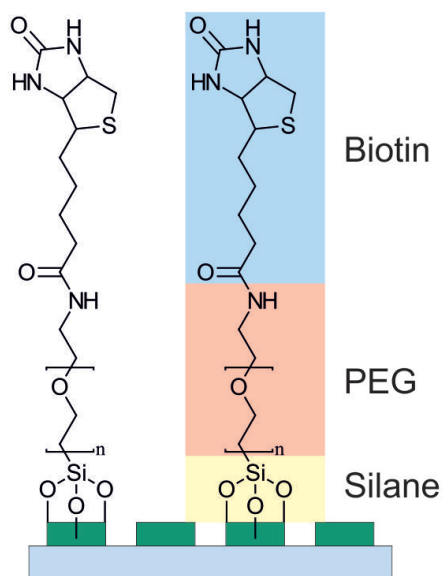
3.) Streptavidin Capture
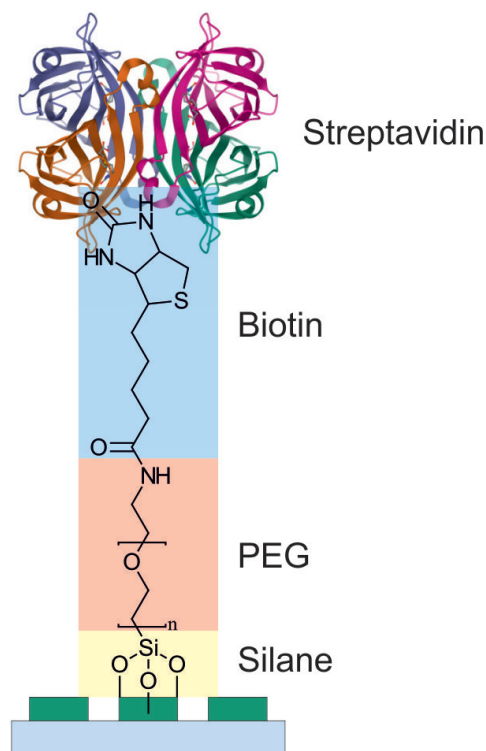
FIGURE 6.10: Streptavidin binding procedures for silicon nanoellipses. In the first step, oxygen plasma is used to generate hydroxyl groups, -OH, on the sample's surface. In the second step, a interaction of the silane group on the linker molecules with the hydroxyl groups on the sample's surface causes the linker molecules to attach to the sample. In the third step, the binding sites on the linker molecule are used to bind streptavidin to the biotin.

1. First, using an oxygen plasma cleaning procedure, it was possible to achieve surface activation by producing hydroxyl groups, -OH, on the metasurfaces' surface (5 min at 200 W). Since silicon contains a small layer of native SiO_2 after manufacture, oxygen plasma cleaning can easily introduce the -OH groups, making this surface activation procedure conceivable.

2. Second, silane/PEG/biotin molecules (Mw = 2000 g/mol, supplied by NANO-CS) were used as the linker between the silicon nanostructures and the streptavidin to carry out linker functionalization. Three functional groups:

   - biotin (in azure),

   - PEG: polyethylene glycol (in red), and

   - silane (in light yellow)

   make up this linker molecule. While the analytes are captured by the biotin group, the silane group is required to connect with the Si surface. PEG represents a polymer joining the two functional groups. To obtain the average molecular weight, n repeating units are used. The above linker molecules are dissolved in a PBS (phosphate-buffered saline) aqueous solution with pH 7.4 to produce a solution that contains 10^{-4} M of such linker molecules. After the sample has been cleaned with oxygen plasma, each array is immediately coated with a 12 μl droplet of linker solution and allowed to air-dry. The reaction between the linker molecules' silane groups and the -OH of the nanostructures results in the formation of strong bonds[5]. Following the droplet's evaporation, the sample is rinsed with DI water to get rid of any remaining unspecifically bounded linkers, and then it is dried using compressed nitrogen gas.

3. Finally, the streptavidin is attached to the linker molecules' biotin groups. To attain the desired concentration (10^{-7} M), the streptavidin

solution is produced by dissolving streptavidin powder (purchased from Sigma Aldrich) in a pH 7.4 aqueous PBS solution. After using the linker molecules to conduct surface functionalization, each array is coated with a 12 μl droplet[60] of the produced streptavidin solution, which is then allowed to dry in air. The four Streptavidin's binding sites can then create strong bonds with the linker molecules' biotin, thanks to the high affinity for one another (dissociation constant $K_d = 10^{-14}$ M). Following the droplet's evaporation, the sample is cleaned with DI water to get rid of any unreacted streptavidin before being dried with pressurized nitrogen gas. Before characterization, the sample was checked for particle residues under optical microscope.

Optical Characterization

The linear-optical spectrum of the unfunctionalized silicon arrays were acquired as a reference. This measuring procedure makes use of linearly polarized incident light and the specially constructed spectroscopic equipment that was previously discussed in Chapter 4. The incident light is focused on the sample, and the light that passes through it is collected. A sample's unstructured area is used as the reference for the transmittance through the sample.

Results

For the measurements, the following steps were taken:

1. Pristine measurement: spectrum of the bare sample in PBS, without biotin.

2. Baseline measurement: Take a baseline spectrum measurement of the biotin-coated nanoellipses arrays.

3. Streptavidin binding: as previously described.

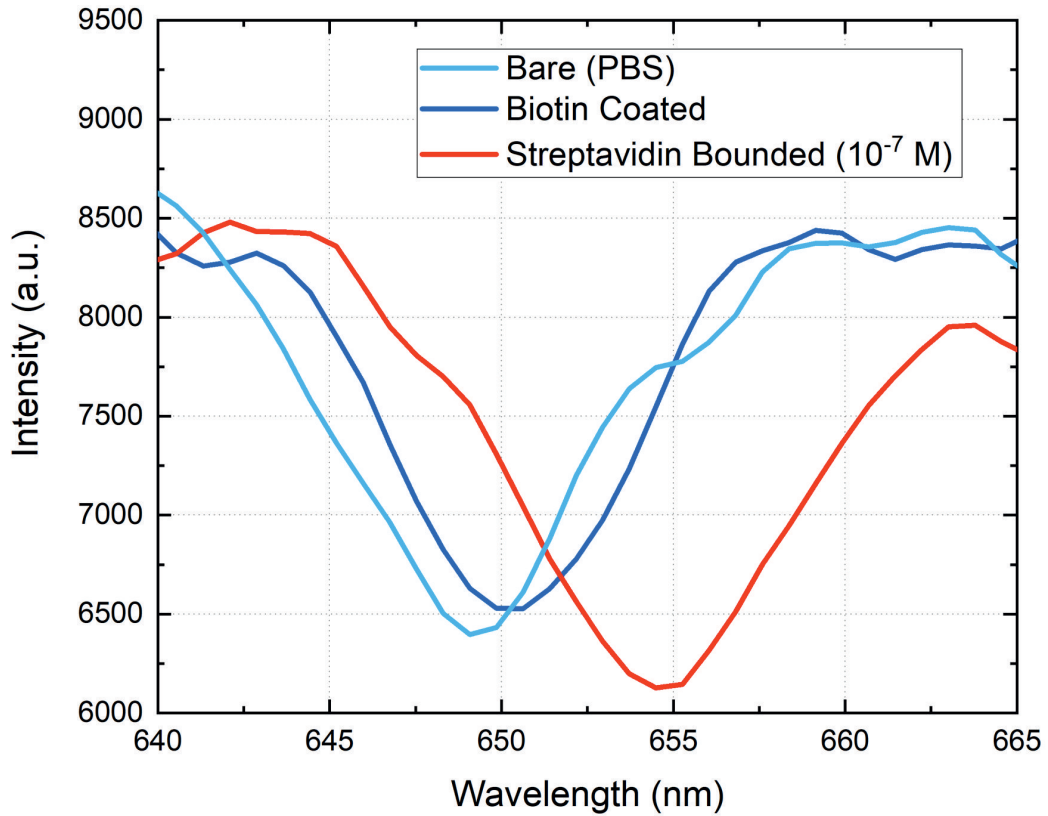4. Bound measurement: record the spectra of the streptavdin-bound sample.

FIGURE 6.11: Linear-optical spectra for the bare sample in PBS (azure), biotin-coated (blue) and streptavidin-bound (red) nanostructures with polarized light.

Figure 6.11 represents the measurement process's spectrum.

As a result of applying a drop of 10^{-7} M streptavidin solution to the biotin-coated nanoellipses, the resonance dip of the biotin bound at (650,5 ± 0,6) nm red shifts to (655,7 ± 0,2) nm, with a difference of about $\Delta = 5,2$ nm.

This finding suggests that biocompatible, reliable, and robust protein sensing at low concentrations may be possible using all-dielectric nanostructures as a new platform. Furthermore, such a dielectric sensing substrate is particularly well suited for sensing and accommodates a wide variety of surface functionalization processes. On the other side, thiols and a few other groups comprising more complicated procedures are typically the only functional

groups appropriate for plasmonic sensors. This implies that compared to a plasmonic sensing platform[2], a platform for dielectric sensing offers additional paths or methods for identifying various target biological species.

Moreover, because silicon is a dielectric element, it does not cause Ohmic losses and local heating like metals do. These benefits increase the silicon-based nanophotonic sensors' resistance to various sensing environments, making them more suitable for *in vivo* measurements. Looking into the potential for practical and commercial use, the remarkable cost effectiveness of these nanostructures makes it possible to mass produce an all-dielectric sensing platform. Since silicon is the most common material in CMOS compatible devices, which are a major component of the modern electronic industry, an adaptation for silicon sensor manufacture is likely to occur as the technology for dielectric nanophotonic sensing develops.

6.4   Conclusion

In this chapter, a general immobilization technique for structures exposing a sulfhydryl group (thiols) on silicon substrates is described. Contact-angle goniometric and XPS analyses are used to track the changes that are occurring on the surface. Each individual transformation step is tracked during immobilization by the change in contact angle. In contrast, the XPS studies reinforce the inferences made from the development of the contact angle and gain from the addition of halide atoms as labels. Two distinctive XPS labels were developed in order to aid in the XPS analysis. Both of these labels provide XPS signals in regions of the spectrum where non-metallic signals are absent. By observing the intensity of the labels, it is possible to confirm the reported surface transition because these different XPS labels are present on both the linker structure and the model thiol. Without the use of noble metal coatings or noble metal-nanostructures, this immobilization technique permits the use of the huge libraries of receptors exposing a sulfhydryl, both for research and commercially available ones, on silicon surfaces. Numerous

innovative miniaturized silicon-based applications in diagnostics, sensing, and/or electronics will be made possible thanks to the robustness of silicon-based technology.

After that, experimental streptavidin sensing was demonstrated utilizing arrays of silicon nanoellipse resonators coated with biotin. This experiment demonstrates the potential of a nanosized, all-dielectric system for biosensing. Applications for resonant silicon nanosensors in medicine include more precise molecular identification, disease diagnostics, and medication detection. These applications may be combined with additional benefits of the silicon technology, like low conductivity, excellent resonance quality, and biocompatibility.

Chapter 7

Conclusions

The thesis provides evidence of advancements in the field of NIR and VIS metasurfaces and their nanofabrication techniques for label-free sensing applications. The doctorate thesis's first chapter discusses the idea of metasurfaces and examines the most recent metasurfaces and sensing modalities. In Chapter 2, the elliptic unit-cell structure is defined, and the metasurface unit-cell design is demonstrated. The focus of Chapter 3 is on manufacturing, starting with the several issues that must be resolved in order to build such a device, and providing a brief overview of electron-beam lithography (EBL) and nanoimprint lithography (NIL). The description of a special three-layer transfer method based on EBL and NIL follows.

Results are then given for master fabrication, substrate preparation, NIL patterning, pattern transfer, metrology, and overall fabrication. The intensity variations of the fabricated metasurfaces are measured in the fourth chapter using a specially designed microscope equipment. First, a brief description of optical transmission spectroscopy and the fundamental signal processing approach are given. An overview of microfluidic devices that can contain metasurfaces is provided later. After that, the optical setup design is provided, and commercially available software is used to demonstrate system control. Finally, a microfluidic chamber's design and production are presented.

An overview of the various tuning methods for dielectric metasurfaces is

given in Chapter 5, with a focus on the tunability provided by geometrical alterations and changes in the refractive index of the immediate surroundings. For structures that expose a sulfhydryl group (thiols) on silicon substrates, an universal immobilization approach is presented in Chapter 6. Contact-angle goniometric and XPS measurements were utilized to monitor the changes that are taking place on the surface. Then, using products that were easily available on the market, experimental streptavidin sensings are demonstrated employing arrays of silicon nano-ellipse resonators covered with biotin. It experimentally illustrates the capability of a nanoscale, all-dielectric biosensing device.

In summary, this thesis showed how to successfully fabricate and optically characterize dielectric metasurfaces in the NIR-visible region of the electromagnetic spectrum.

Chapter 8

Outlook

The dielectric metasurface exhibited here exemplifies the potential of biosensing. Dielectric metasurfaces' unique capacities to enhance the light-matter interactions as well as their additional degrees of freedom in their optical responses will have a significant impact on how on-demand functions are designed. Despite the fact that they have showed considerable promise, there are still a number of unresolved issues. One of them is to provide a general technique for the mass production of various types of dielectric metasurface sensors. Despite the efficient manufacture of metasurfaces reported both in this thesis and in some recent works, such as nanoimprinting[59,27], laser direct writing[49,156], and hole-mask lithography[182,185,25], there are still no techniques that are compatible with conventional semiconductor processes. The improvement of the dielectric metasurfaces' sensitivity is another area for future research. Dielectric metasurfaces can give enough sensitives, according to recent studies, but their total performance is still below that of their state-of-the-art plasmonic equivalents.

Additionally, the development of dielectric metasurfaces and the application of these materials in devices is facilitated by advances in material science. Many materials' potential applications for metasurfaces have not yet been fully explored, but they can be looked into to expand the field of dielectric metasurfaces. Multifunctional metasurfaces with the ability to both provide near-field enhancements and serve as light sources on-chip can be

created for ultracompact sensor integration by utilizing active materials, like GaN and GaAs. Additionally, certain unusual materials have lately been exploited for metasurfaces to develop new optical features. These materials include high-index chalcogenides[160,86], phase-change media[35,92], multiple quantum wells[166,139], and perovskites[50,54]. Further research into atypical metasurface materials could result in high-performance optical biosensors.

Concurrently, metasurface-based sensing technologies can address the miniaturization of the present bioanalytical and clinical devices. Providing a quick, effective, and accurate diagnosis is crucial for treating life-threatening illnesses on time. Devices that enable point-of-care diagnostics and constant health screening nowadays are more and more important for preserving life and enhancing quality of life[170,144]. Whereas the incorporation of plasmonic metasurfaces in systems like lab-on-a-chip[15], CMOS-based chips[66,26,67], and microfluidic devices[70,131,29] is more developed, the incorporation of dielectric metasurfaces is still in its early life and is anticipated to take advantage of collected knowledge in order to achieve new functionalities.

Last but not least, artificial intelligence is a useful technique for increasing the capability of metasurface sensors. The new areas to research are novel methods to design metasurfaces and cutting-edge data processing. Inverted designs of metasurfaces owning specified optical qualities have never before been possible thanks to machine learning, as demonstrated by a number of publications[101,106]. A fresh approach to developing metasurface sensors with qualities that need rigorous requirements can be found in artificial intelligence. It is possible to create optical sensors that can recognize molecular patterns, differentiate molecules in complex settings, and observe dynamic molecular interactions by fusing machine learning and innovative dielectric metasurfaces.

List of Figures

List of Abbreviations

2D / 3D	two / three dimensional
a-Si	amorphous silicon
AFM	atomic force microscopy
ALD	atomic layer deposition
BE	binding energy
BHF	buffered hydrofluoric acid
BIC	bound state in the continuum
CAD	computer-aided design
CCD	charge-coupled device
CMOS	complementary metal–oxide–semiconductor
CVD	chemical vapour deposition
DCM	dichloromethane
DI	deionized
DLW	direct-laser writing
DMF	dimethylformamide
DNA	deoxyribonucleic acid
DUV	deep ultraviolet
EBL	electron-beam lithography
ELISA	enzyme-linked immunosorbent assay
FFT	fast fourier transform
FIB	focus ion beam lithography
FOM	figure of merit
FWHM	full width at half maximum
HeIM	helium ion microscopy
HSQ	hydrogen silsesquioxane

ICP	inductively coupled plasma
IPA	isopropanol
IR	infrared
LSPP	localised surface plasmon polariton
LSPR	localised surface plasmon resonance
mCPBA	meta-chloroperoxybenzoic
Mw	molecular weight
n	refractive index
NIL	nanoimprint lithography
NIR	near infrared
NP	nanoparticle
PBS	phosphate-buffered saline
PCR	polymerase chain reaction
PDMS	polydimethylsiloxane
PEC	proximity effects correction
PECVD	plasma-enhanced physical vapour deposition
PEG	poly(ethylene glycol)
PhC	photonic crystal
POCT	point-of-care testing
Q	quality
QCM	quartz crystal microbalance
RF	radio frequency
RIE	reactive ion etch
RIU	refractive index unit
RNA	ribonucleic acid
rpm	rounds per minute
SAM	self-assembled monolayer
SE	secondary electron(s)
SEM	scanning electron microscopy
S	sensitivity
SLB	supported lipid bilayers

SPL	scanning probe lithography
SPP	surface plasmon polariton
SPR	surface plasmon resonance
UHV	ultra-high vacuum
UV	ultraviolet
VIS	visible
XPS	X-ray photoelectron spectroscopy

Bibliography

[1] Alessandro Alabastri et al. "Resonant energy transfer enhances solar thermal desalination". In: *Energy and Environmental Science* 13.3 (2020), pp. 968–976.

[2] Ivano Alessandri and John R. Lombardi. "Enhanced Raman Scattering with Dielectrics". In: *Chemical Reviews* 116.24 (Oct. 2016), pp. 14921–14981.

[3] Hatice Altug, Dirk Englund, and Jelena Vučković. "Ultrafast photonic crystal nanocavity laser". In: *Nature Physics* 2.7 (July 2006), pp. 484–488.

[4] Andrea Alu and Nader Engheta. "Achieving transparency with plasmonic and metamaterial coatings". In: *Physical Review E* 72.1 (July 2005).

[5] P. Amirfeiz et al. "Formation of Silicon Structures by Plasma-Activated Wafer Bonding". In: *Journal of The Electrochemical Society* 147.7 (2000), p. 2693.

[6] Jeffrey N. Anker et al. "Biosensing with plasmonic nanosensors". In: *Nature Materials* 7.6 (June 2008), pp. 442–453.

[7] Amir Arbabi and Andrei Faraon. "Fundamental limits of ultrathin metasurfaces". In: *Scientific Reports* 7.1 (Mar. 2017).

[8] Amir Arbabi et al. "Efficient dielectric metasurface collimating lenses for mid-infrared quantum cascade lasers". In: *Optics Express* 23.26 (Dec. 2015), p. 33310.

[9] Jose Luis R. Arrondo et al. "Quantitative studies of the structure of proteins in solution by fourier-transform infrared spectroscopy". In: *Progress in Biophysics and Molecular Biology* 59.1 (1993), pp. 23–56.

[10]   Harry A. Atwater and Albert Polman. "Plasmonics for improved photovoltaic devices". In: *Nature Materials* 9.3 (Feb. 2010), pp. 205–213.

[11]   Michael D. Austin et al. "Fabrication of 5nm linewidth and 14nm pitch features by nanoimprint lithography". In: *Applied Physics Letters* 84.26 (June 2004), pp. 5299–5301.

[12]   Suneev Anil Bansal et al. "Role of gold nanoparticles in advanced biomedical applications". In: *Nanoscale Advances* 2.9 (2020), pp. 3764–3787.

[13]   Andreas Barth. "Infrared spectroscopy of proteins". In: *Biochimica et Biophysica Acta (BBA) - Bioenergetics* 1767.9 (Sept. 2007), pp. 1073–1101.

[14]   Frerik van Beijnum et al. "Surface Plasmon Lasing Observed in Metal Hole Arrays". In: *Physical Review Letters* 110.20 (May 2013).

[15]   Alexander Belushkin et al. "Rapid and Digital Detection of Inflammatory Biomarkers Enabled by a Novel Portable Nanoplasmonic Imager". In: *Small* 16.3 (Dec. 2019), p. 1906108.

[16]   A.D. Boardman and A.V. Zayats. "Nonlinear Plasmonics". In: (2014), pp. 329–347.

[17]   Nicolo Bontempi et al. "Plasmon-free SERS detection of environmental CO_2 on TiO_2 surfaces". In: *Nanoscale* 8.6 (2016), pp. 3226–3231.

[18]   Nicolo Bontempi et al. "Probing the spatial extension of light trapping-induced enhanced Raman scattering in high-density Si nanowire arrays". In: *Nanotechnology* 25.46 (Oct. 2014), p. 465705.

[19]   Sophie Brenet et al. "Highly-Selective Optoelectronic Nose Based on Surface Plasmon Resonance Imaging for Sensing Volatile Organic Compounds". In: *Analytical Chemistry* 90.16 (July 2018), pp. 9879–9887.

[20]   J. J. Brondijk et al. "Charge transport in dual-gate organic field-effect transistors". In: *Applied Physics Letters* 100.2 (Jan. 2012), p. 023308.

[21]   Lisa V. Brown et al. "Surface-Enhanced Infrared Absorption Using Individual Cross Antennas Tailored to Chemical Moieties". In: *Journal of the American Chemical Society* 135.9 (Feb. 2013), pp. 3688–3695.

[22] S. Cabrini et al. "Focused ion beam lithography for two dimensional array structures for photonic applications". In: *Microelectronic Engineering* 78-79 (2005), pp. 11–15. ISSN: 0167-9317.

[23] Martin Caldarola et al. "Non-plasmonic nanoantennas for surface enhanced spectroscopies with ultra-low heat conversion". In: *Nature Communications* 6.1 (Aug. 2015).

[24] Linyou Cao et al. "Tuning the Color of Silicon Nanostructures". In: *Nano Letters* 10.7 (May 2010), pp. 2649–2654.

[25] Stefano Cataldo et al. "Hole-Mask Colloidal Nanolithography for Large-Area Low-Cost Metamaterials and Antenna-Assisted Surface-Enhanced Infrared Absorption Substrates". In: *ACS Nano* 6.1 (Dec. 2011), pp. 979–985.

[26] Benjamin Cerjan and Naomi J. Halas. "Toward a Nanophotonic Nose: A Compressive Sensing-Enhanced, Optoelectronic Mid-Infrared Spectrometer". In: *ACS Photonics* 6.1 (Dec. 2018), pp. 79–86.

[27] Debashis Chanda et al. "Large-area flexible 3D optical negative index metamaterial formed by nanotransfer printing". In: *Nature Nanotechnology* 6.7 (June 2011), pp. 402–407.

[28] V. Chechik, R. M. Crooks, and C. J. M. Stirling. "Reactions and Reactivity in Self-Assembled Monolayers". In: *Advanced Materials* 12.16 (Aug. 2000), pp. 1161–1171.

[29] Chang Chen et al. "High spatial resolution nanoslit SERS for single-molecule nucleobase sensing". In: *Nature Communications* 9.1 (Apr. 2018).

[30] Katie E. Chong et al. "Polarization-Independent Silicon Metadevices for Efficient Optical Wavefront Control". In: *Nano Letters* 15.8 (July 2015), pp. 5369–5374.

[31] Stephen Y. Chou. "Nanoimprint lithography". In: *Journal of Vacuum Science & Technology B: Microelectronics and Nanometer Structures* 14.6 (Nov. 1996), p. 4129.

[32]   Stephen Y. Chou. "Sub-10 nm imprint lithography and applications". In: *Journal of Vacuum Science & Technology B: Microelectronics and Nanometer Structures* 15.6 (Nov. 1997), p. 2897.

[33]   Stephen Y. Chou, Peter R. Krauss, and Preston J. Renstrom. "Imprint Lithography with 25-Nanometer Resolution". In: *Science* 272.5258 (Apr. 1996), pp. 85–87.

[34]   Stephen Y. Chou, Peter R. Krauss, and Preston J. Renstrom. "Imprint of sub-25 nm vias and trenches in polymers". In: *Applied Physics Letters* 67.21 (Nov. 1995), pp. 3114–3116.

[35]   Cheng Hung Chu et al. "Active dielectric metasurface based on phase-change medium". In: *Laser and Photonics Reviews* 10.6 (Oct. 2016), pp. 986–994.

[36]   Narendra B. Dahotre and S. Nayak. "Nanocoatings for engine application". In: *Surface and Coatings Technology* 194.1 (Apr. 2005), pp. 58–67.

[37]   Manuel Decker and Isabelle Staude. "Resonant dielectric nanostructures: a low-loss platform for functional nanophotonics". In: *Journal of Optics* 18.10 (Sept. 2016), p. 103001.

[38]   Manuel Decker et al. "High-Efficiency Dielectric Huygens' Surfaces". In: *Advanced Optical Materials* 3.6 (Feb. 2015), pp. 813–820.

[39]   Romain Dezert. "Theoretical study of isotropic Huygens particles for metasurfaces". PhD thesis. Dec. 2019.

[40]   Liangliang Dong et al. "Nanogapped Au Antennas for Ultrasensitive Surface-Enhanced Infrared Absorption Spectroscopy". In: *Nano Letters* 17.9 (Sept. 2017), pp. 5768–5774.

[41]   S Doniach and M Sunjic. "Many-electron singularity in X-ray photoemission and X-ray line spectra from metals". In: *Journal of Physics C: Solid State Physics* 3.2 (Feb. 1970), pp. 285–291.

[42]   Ute Drechsler and Emanuel Lörtscher. "Mass-fabrication Compatible Structuring of Semiconductor Metasurfaces". In: *P201906800US01* (2020).

[43] Christopher M. Dundas, Daniel Demonte, and Sheldon Park. "Streptavidin-biotin technology: improvements and innovations in chemical and biological applications". In: *Applied Microbiology and Biotechnology* 97.21 (Sept. 2013), pp. 9343–9353.

[44] Faten Bashar Kamal Eddin et al. "Femtomolar detection of dopamine using surface plasmon resonance sensor based on chitosan/graphene quantum dots thin film". In: *Spectrochimica Acta Part A: Molecular and Biomolecular Spectroscopy* 263 (Dec. 2021), p. 120202.

[45] Andrey B. Evlyukhin et al. "Demonstration of Magnetic Dipole Resonances of Dielectric Nanospheres in the Visible Region". In: *Nano Letters* 12.7 (June 2012), pp. 3749–3755.

[46] L. A. Falkovsky and S. S. Pershoguba. "Optical far-infrared properties of a graphene monolayer and multilayer". In: *Physical Review B* 76.15 (Oct. 2007).

[47] MohammadSadegh Faraji-Dana et al. "Compact folded metasurface spectrometer". In: *Nature Communications* 9.1 (Oct. 2018).

[48] Guilherme N.M. Ferreira, Ana-Carina da-Silva, and Brigitte Tomé. "Acoustic wave biosensors: physical models and biological applications of quartz crystal microbalance". In: *Trends in Biotechnology* 27.12 (Dec. 2009), pp. 689–697.

[49] Justyna K. Gansel et al. "Gold Helix Photonic Metamaterial as Broadband Circular Polarizer". In: *Science* 325.5947 (Sept. 2009), pp. 1513–1515.

[50] Yisheng Gao et al. "Lead Halide Perovskite Nanostructures for Dynamic Color Display". In: *ACS Nano* 12.9 (Aug. 2018), pp. 8847–8854.

[51] A. Garcia-Etxarri et al. "Strong magnetic response of submicron Silicon particles in the infrared". In: *Optics Express* 19.6 (Feb. 2011), p. 4815.

[52] Laurie-Amandine Garçon et al. "A Versatile Electronic Tongue Based on Surface Plasmon Resonance Imaging and Cross-Reactive Sensor Arrays—A Mini-Review". In: *Sensors* 17.5 (May 2017), p. 1046.

[53] Vivian Garzon et al. "Optical Biosensors for Therapeutic Drug Monitoring". In: *Biosensors* 9.4 (Nov. 2019), p. 132.

[54] Behrad Gholipour et al. "Organometallic Perovskite Metasurfaces". In: *Advanced Materials* 29.9 (Jan. 2017), p. 1604268.

[55] V. Giannini, G. Vecchi, and J. Gómez Rivas. "Lighting Up Multipolar Surface Plasmon Polaritons by Collective Resonances in Arrays of Nanoantennas". In: *Physical Review Letters* 105.26 (Dec. 2010).

[56] Ana Goncalves et al. "Trends in Protein-Based Biosensor Assemblies for Drug Screening and Pharmaceutical Kinetic Studies". In: *Molecules* 19.8 (Aug. 2014), pp. 12461–12485.

[57] Tatjana Gric and Ortwin Hess. "Metasurfaces". In: (2019), pp. 131–154.

[58] J. van de Groep and A. Polman. "Designing dielectric resonators on substrates: Combining magnetic and electric resonances". In: *Optics Express* 21.22 (Oct. 2013), p. 26285.

[59] Tapajyoti Das Gupta et al. "Self-assembly of nanostructured glass metasurfaces via templated fluid instabilities". In: *Nature Nanotechnology* 14.4 (Feb. 2019), pp. 320–327.

[60] Amanda J. Haes and Richard P. Van Duyne. "A Nanoscale Optical Biosensor: Sensitivity and Selectivity of an Approach Based on the Localized Surface Plasmon Resonance Spectroscopy of Triangular Silver Nanoparticles". In: *Journal of the American Chemical Society* 124.35 (Aug. 2002), pp. 10596–10604.

[61] Jan Haisma. "Mold-assisted nanolithography: A process for reliable pattern replication". In: *Journal of Vacuum Science & Technology B: Microelectronics and Nanometer Structures* 14.6 (Nov. 1996), p. 4124.

[62] R. Hesse, T. Chasse, and R. Szargan. "Peak shape analysis of core level photoelectron spectra using UNIFIT for WINDOWS". In: *Fresenius Journal of Analytical Chemistry* 365.1-3 (Sept. 1999), pp. 48–54.

[63] L. R. Hirsch et al. "Nanoshell-mediated near-infrared thermal therapy of tumors under magnetic resonance guidance". In: *Proceedings of the National Academy of Sciences* 100.23 (Nov. 2003), pp. 13549–13554.

[64] David Holmes et al. "Bead-based immunoassays using a micro-chip flow cytometer". In: *Lab on a Chip* 7.8 (2007), p. 1048.

[65] Jiri Homola. "Surface Plasmon Resonance Sensors for Detection of Chemical and Biological Species". In: *Chemical Reviews* 108.2 (Jan. 2008), pp. 462–493.

[66] Lingyu Hong et al. "Fully Integrated Fluorescence Biosensors On-Chip Employing Multi-Functional Nanoplasmonic Optical Structures in CMOS". In: *IEEE Journal of Solid-State Circuits* 52.9 (Sept. 2017), pp. 2388–2406.

[67] Lingyu Hong et al. "Integrated Angle-Insensitive Nanoplasmonic Filters for Ultraminiaturized Fluorescence Microarray in a 65 nm Digital CMOS Process". In: *ACS Photonics* 5.11 (Sept. 2018), pp. 4312–4322.

[68] Helmuth Horvath. "Gustav Mie and the scattering and absorption of light by particles: Historic developments and basics". In: *Journal of Quantitative Spectroscopy and Radiative Transfer* 110.11 (July 2009), pp. 787–799.

[69] By Sudhir Husale et al. "ssDNA Binding Reveals the Atomic Structure of Graphene". In: *Langmuir* 26.23 (Oct. 2010), pp. 18078–18082.

[70] Aurelian John-Herpin, Andreas Tittl, and Hatice Altug. "Quantifying the Limits of Detection of Surface-Enhanced Infrared Spectroscopy with Grating Order-Coupled Nanogap Antennas". In: *ACS Photonics* 5.10 (Sept. 2018), pp. 4117–4124.

[71] Sajeev John. "Strong localization of photons in certain disordered dielectric superlattices". In: *Physical Review Letters* 58.23 (June 1987), pp. 2486–2489.

[72] Blake N. Johnson and Raj Mutharasan. "Biosensor-based microRNA detection: techniques, design, performance, and challenges". In: *The Analyst* 139.7 (2014), p. 1576.

[73] Qiushi Kang et al. "Low-Temperature Co-hydroxylated Cu/SiO_2 Hybrid Bonding Strategy for a Memory-Centric Chip Architecture". In: *ACS Applied Materials and Interfaces* 13.32 (July 2021), pp. 38866–38876.

[74] K. Lance Kelly et al. "The Optical Properties of Metal Nanoparticles: The Influence of Size, Shape, and Dielectric Environment". In: *The Journal of Physical Chemistry B* 107.3 (Dec. 2002), pp. 668–677.

[75] Mohammadreza Khorasaninejad et al. "Metalenses at visible wavelengths: Diffraction-limited focusing and subwavelength resolution imaging". In: *Science* 352.6290 (June 2016), pp. 1190–1194.

[76] Tugba Kilic et al. "microRNA biosensors: Opportunities and challenges among conventional and commercially available techniques". In: *Biosensors and Bioelectronics* 99 (Jan. 2018), pp. 525–546.

[77] Dong Min Kim et al. "Biosensing Applications Using Nanostructure-Based Localized Surface Plasmon Resonance Sensors". In: *Sensors* 21.9 (May 2021), p. 3191.

[78] Ueli Koch et al. "Plasmonics high-speed photonics for co-integration with electronics". In: *Japanese Journal of Applied Physics* 60.SB (Apr. 2021), SB0806.

[79] Katarzyna M. Koczula and Andrea Gallotta. "Lateral flow assays". In: *Essays in Biochemistry* 60.1 (June 2016). Ed. by Pedro Estrela, pp. 111–120.

[80] A. Femius Koenderink, Andrea Alù, and Albert Polman. "Nanophotonics: Shrinking light-based technology". In: *Science* 348.6234 (June 2015), pp. 516–521.

[81] A. A. Komar, D. N. Neshev, and A. E. Miroshnichenko. "Tunable Dielectric Metasurfaces Based on the Variation of the Refractive Index of the Environment". In: *JETP Letters* 106.11 (Dec. 2017), pp. 709–715.

[82] Jilie Kong and Shaoning Yu. "Fourier Transform Infrared Spectroscopic Analysis of Protein Secondary Structures". In: *Acta Biochimica et Biophysica Sinica* 39.8 (Sept. 2007), pp. 549–559.

[83] Kirill Koshelev and Yuri Kivshar. "Dielectric Resonant Metaphotonics". In: *ACS Photonics* 8.1 (Sept. 2020), pp. 102–112.

[84] Alexander E. Krasnok et al. "All-dielectric optical nanoantennas". In: *Optics Express* 20.18 (Aug. 2012), p. 20599.

[85] Alexander Krasnok, Mykhailo Tymchenko, and Andrea Alu. "Nonlinear metasurfaces: a paradigm shift in nonlinear optics". In: *Materials Today* 21.1 (Jan. 2018), pp. 8–21.

[86] H. N. S. Krishnamoorthy et al. "Infrared dielectric metamaterials from high refractive index chalcogenides". In: *Nature Communications* 11.1 (Apr. 2020).

[87] Eiichi Kuramochi et al. "Large-scale integration of wavelength-addressable all-optical memories on a photonic crystal chip". In: *Nature Photonics* 8.6 (May 2014), pp. 474–481.

[88] Arseniy I. Kuznetsov et al. "Magnetic light". In: *Scientific Reports* 2.1 (July 2012).

[89] Arseniy I. Kuznetsov et al. "Optically resonant dielectric nanostructures". In: *Science* 354.6314 (Nov. 2016).

[90] Sheeny Lan, Mandana Veiseh, and Miqin Zhang. "Surface modification of silicon and gold-patterned silicon surfaces for improved biocompatibility and cell patterning selectivity". In: *Biosensors and Bioelectronics* 20.9 (Mar. 2005), pp. 1697–1708.

[91] Gun-Yeal Lee et al. "Metasurface eyepiece for augmented reality". In: *Nature Communications* 9.1 (Nov. 2018), p. 4562.

[92] Aleksandrs Leitis et al. "All-Dielectric Programmable Huygens' Metasurfaces". In: *Advanced Functional Materials* 30.19 (Mar. 2020), p. 1910259.

[93] Rudolf M Lequin. "Enzyme Immunoassay (EIA)/Enzyme-Linked Immunosorbent Assay (ELISA)". In: *Clinical Chemistry* 51.12 (Dec. 2005), pp. 2415–2418.

[94] EnZe Li, ZhiPing Du, and ShiLing Yuan. "Properties of a water layer on hydrophilic and hydrophobic self-assembled monolayer surfaces: A molecular dynamics study". In: *Science China Chemistry* 56.6 (Jan. 2013), pp. 773–781.

[95] Inigo Liberal and Nader Engheta. "Near-zero refractive index photonics". In: *Nature Photonics* 11.3 (Mar. 2017), pp. 149–158.

[96] Bo Liedberg, Claes Nylander, and Ingemar Lunström. "Surface plasmon resonance for gas detection and biosensing". In: *Sensors and Actuators* 4 (Jan. 1983), pp. 299–304.

[97] Odeta Limaj et al. "Infrared Plasmonic Biosensor for Real-Time and Label-Free Monitoring of Lipid Membranes". In: *Nano Letters* 16.2 (Jan. 2016), pp. 1502–1508.

[98] Mingkai Liu and Duk-Yong Choi. "Extreme All-dielectric Huygens' Metasurfaces based on Quasi-bound States in the Continuum". In: *Nano Letters* 18.12 (2019), pp. 8062–8069.

[99] Mingkai Liu and Duk-Yong Choi. "Extreme Huygens' Metasurfaces Based on Quasi-Bound States in the Continuum". In: *Nano Letters* 18.12 (Nov. 2018), pp. 8062–8069.

[100] Na Liu et al. "Infrared Perfect Absorber and Its Application As Plasmonic Sensor". In: *Nano Letters* 10.7 (June 2010), pp. 2342–2348.

[101] Zhaocheng Liu et al. "Generative Model for the Inverse Design of Metasurfaces". In: *Nano Letters* 18.10 (Sept. 2018), pp. 6570–6576.

[102] Marko Lončar et al. "Waveguiding in planar photonic crystals". In: *Applied Physics Letters* 77.13 (Sept. 2000), pp. 1937–1939.

[103] S. A. Maier et al. "Plasmonics-A Route to Nanoscale Optical Devices". In: *Advanced Materials* 13.19 (Sept. 2001), pp. 1501–1505.

[104] Stefan A. Maier et al. "Local detection of electromagnetic energy transport below the diffraction limit in metal nanoparticle plasmon waveguides". In: *Nature Materials* 2.4 (Mar. 2003), pp. 229–232.

[105] Sergey V. Makarov et al. "Multifold Emission Enhancement in Nanoimprinted Hybrid Perovskite Metasurfaces". In: *ACS Photonics* 4.4 (Mar. 2017), pp. 728–735.

[106] Itzik Malkiel et al. "Plasmonic nanostructure design and characterization via Deep Learning". In: *Light: Science and Applications* 7.1 (Sept. 2018).

[107] Frank Marlow et al. "Opals: Status and Prospects". In: *Angewandte Chemie International Edition* 48.34 (Sept. 2009), pp. 6212–6233.

[108] C.F.R. Mateus et al. "Broad-band mirror (1.12–1.62 μm) using a sub-wavelength grating". In: *IEEE Photonics Technology Letters* 16.7 (July 2004), pp. 1676–1678.

[109] Simon G. J. Mathijssen et al. "Monolayer coverage and channel length set the mobility in self-assembled monolayer field-effect transistors". In: *Nature Nanotechnology* 4.10 (Aug. 2009), pp. 674–680.

[110] J.C. Maxwell Garnett. "Colours in Metal Glasses and in Metallic Films". In: *Philosophical Transactions of the Royal Society of London Series A* 203 (Jan. 1904), pp. 385–420.

[111] Gustav Mie. "Beiträge zur Optik trüber Medien, speziell kolloidaler Metallösungen". In: *Annalen der Physik* 330.3 (1908), pp. 377–445.

[112] Francesco Monticone and Andrea Alu. "Invisibility exposed: physical bounds on passive cloaking". In: *Optica* 3.7 (July 2016), p. 718.

[113] John F. Moulder and Jill Chastain. "Handbook of x-ray photoelectron spectroscopy : a reference book of standard spectra for identification and interpretation of XPS data". In: *Physical Electronics Division, Perkin-Elmer Corp., Eden Prairie, Minn.* (1992).

[114] Raghunath Murali et al. "Process optimization and proximity effect correction for gray scale e-beam lithography". In: *Journal of Vacuum Science & Technology B: Microelectronics and Nanometer Structures* 24.6 (2006), p. 2936.

[115] Frank B. Myers and Luke P. Lee. "Innovations in optical microfluidic technologies for point-of-care diagnostics". In: *Lab on a Chip* 8.12 (2008), p. 2015.

[116] Samiksha Nayak et al. "Point-of-Care Diagnostics: Recent Developments in a Connected Age". In: *Analytical Chemistry* 89.1 (Dec. 2016), pp. 102–123.

[117] Martin Nirschl, Florian Reuter, and Janos Vörös. "Review of Transducer Principles for Label-Free Biomolecular Interaction Analysis". In: *Biosensors* 1.3 (July 2011), pp. 70–92.

[118] Lukas Novotny. "Effective Wavelength Scaling for Optical Antennas". In: *Physical Review Letters* 98.26 (June 2007).

[119] Dong Kyo Oh et al. "Nanoimprint lithography for high-throughput fabrication of metasurfaces". In: *Frontiers of Optoelectronics* 14.2 (Apr. 2021), pp. 229–251.

[120] Andreea Olaru et al. "Surface Plasmon Resonance (SPR) Biosensors in Pharmaceutical Analysis". In: *Critical Reviews in Analytical Chemistry* 45.2 (Jan. 2015), pp. 97–105.

[121] Riikka Peltomaa et al. "Optical Biosensors for Label-Free Detection of Small Molecules". In: *Sensors* 18.12 (Nov. 2018), p. 4126.

[122] Eleonora Petryayeva and Ulrich J. Krull. "Localized surface plasmon resonance: Nanostructures, bioassays and biosensing—A review". In: *Analytica Chimica Acta* 706.1 (2011), pp. 8–24. ISSN: 0003-2670.

[123] Gregory Pieters and Leonard J. Prins. "Catalytic self-assembled monolayers on gold nanoparticles". In: *New Journal of Chemistry* 36.10 (2012), p. 1931.

[124] Alexander Pipchuk and Xiaolong Yang. "Using Biosensors to Study Protein–Protein Interaction in the Hippo Pathway". In: *Frontiers in Cell and Developmental Biology* 9 (Apr. 2021).

[125] U Plachetka. "Wafer scale patterning by soft UV-Nanoimprint Lithography". In: *Microelectronic Engineering* 73-74 (June 2004), pp. 167–171.

[126] Giulia Prone et al. "Scalable, Nanometer-Accurate Fabrication of All-Dielectric Metasurfaces with Narrow Resonances Tunable from Near Infrared to Visible Wavelengths". In: *Advanced Photonics Research* (May 2022), p. 2200014.

[127] Mengyao Qian et al. "A Non-Enzyme and Non-Label Sensitive Fluorescent Aptasensor Based on Simulation-Assisted and Target-Triggered Hairpin Probe Self-Assembly for Ochratoxin a Detection". In: *Toxins* 12.6 (June 2020), p. 376.

[128]   Somayyeh Rahimi et al. "Toward 300 mm Wafer-Scalable High-Performance Polycrystalline Chemical Vapor Deposited Graphene Transistors". In: *ACS Nano* 8.10 (Sept. 2014), pp. 10471–10479.

[129]   Haoran Ren et al. "Complex-amplitude metasurface-based orbital angular momentum holography in momentum space". In: *Nature Nanotechnology* 15.11 (Sept. 2020), pp. 948–955.

[130]   Liming Ren and Baoqin Chen. "Proximity effect in electron beam lithography". In: *IEEE* 1 (2004), pp. 579–582.

[131]   Daniel Rodrigo et al. "Resolving molecule-specific information in dynamic lipid membrane processes with multi-resonant infrared metasurfaces". In: *Nature Communications* 9.1 (June 2018).

[132]   Niranjan S et al. "Au-free recessed Ohmic contacts to AlGaN/GaN high electron mobility transistor: Study of etch chemistry and metal scheme". In: *Journal of Vacuum Science and Technology B* 38.3 (May 2020), p. 032207.

[133]   Thoriq Salafi, Kerwin Kwek Zeming, and Yong Zhang. "Advancements in microfluidics for nanoparticle separation". In: *Lab on a Chip* 17.1 (2017), pp. 11–33.

[134]   Shengbo Sang et al. "Progress of new label-free techniques for biosensors: a review". In: *Critical Reviews in Biotechnology* (Jan. 2015), pp. 1–17.

[135]   Jürgen Sautter et al. "Active Tuning of All-Dielectric Metasurfaces". In: *ACS Nano* 9.4 (Mar. 2015), pp. 4308–4315.

[136]   Helmut Schift. "Nanoimprint lithography: An old story in modern times? A review". In: *Journal of Vacuum Science and Technology B* 26 (2008), p. 458. ISSN: 1071-1023.

[137]   Michael Semmlinger et al. "Vacuum Ultraviolet Light-Generating Metasurface". In: *Nano Letters* 18.9 (Aug. 2018), pp. 5738–5743.

[138]   Matthias Seydack. "Nanoparticle labels in immunosensing using optical detection methods". In: *Biosensors and Bioelectronics* 20.12 (June 2005), pp. 2454–2469.

[139] Kun-Ching Shen et al. "Giant Efficiency of Visible Second-Harmonic Light by an All-Dielectric Multiple-Quantum-Well Metasurface". In: *Physical Review Applied* 12.6 (Dec. 2019), p. 064056.

[140] D. A. Shirley. "High-Resolution X-Ray Photoemission Spectrum of the Valence Bands of Gold". In: *Physical Review B* 5.12 (June 1972), pp. 4709–4714.

[141] D. R. Smith, J. B. Pendry, and M. C. K. Wiltshire. "Metamaterials and Negative Refractive Index". In: *Science* 305.5685 (Aug. 2004), pp. 788–792.

[142] Jack R. Smith, Marcus T. Cicerone, and Curtis W. Meuse. "Tertiary Structure Changes in Albumin upon Surface Adsorption Observed via Fourier Transform Infrared Spectroscopy". In: *Langmuir* 25.8 (Mar. 2009), pp. 4571–4578.

[143] Somayeh Sohrabi, Nour kassir, and Mostafa Keshavarz Moraveji. "Droplet microfluidics: fundamentals and its advanced applications". In: *RSC Advances* 10.46 (2020), pp. 27560–27574.

[144] Maria Soler et al. "How Nanophotonic Label-Free Biosensors Can Contribute to Rapid and Massive Diagnostics of Respiratory Virus Infections: COVID-19 Case". In: *ACS Sensors* 5.9 (Aug. 2020), pp. 2663–2678.

[145] Maria Soler et al. "Two-Dimensional Label-Free Affinity Analysis of Tumor-Specific CD8 T Cells with a Biomimetic Plasmonic Sensor". In: *ACS Sensors* 3.11 (Oct. 2018), pp. 2286–2295.

[146] Michelle L. Solomon et al. "Nanophotonic Platforms for Chiral Sensing and Separation". In: *Accounts of Chemical Research* 53.3 (Jan. 2020), pp. 588–598.

[147] P. Spinelli, M.A. Verschuuren, and A. Polman. "Broadband omnidirectional antireflection coating based on subwavelength surface Mie resonators". In: *Nature Communications* 3.1 (Jan. 2012), p. 692.

[148] Isabelle Staude et al. "Tailoring Directional Scattering through Magnetic and Electric Resonances in Subwavelength Silicon Nanodisks". In: *ACS Nano* 7.9 (Aug. 2013), pp. 7824–7832.

[149] Vin-Cent Su et al. "Advances in optical metasurfaces: fabrication and applications". In: *Optics Express* 26.10 (May 2018), p. 13148.

[150] Leila Syedmoradi et al. "Point of care testing: The impact of nanotechnology". In: *Biosensors and Bioelectronics* 87 (Jan. 2017), pp. 373–387.

[151] Giulia Tagliabue et al. "Ultrafast hot-hole injection modifies hot-electron dynamics in Au/p-GaN heterostructures". In: *Nature Materials* 19.12 (July 2020), pp. 1312–1318.

[152] Mutsuo TANAKA and Osamu NIWA. "Fabrication of Biosensing Interface with Monolayers". In: *Analytical Sciences* 37.5 (May 2021), pp. 673–682.

[153] Andreas Tittl et al. "Imaging-based molecular barcodingwith pixelated dielectric metasurfaces". In: *Science* 360 (2018), pp. 1105–1109. ISSN: 0036-8075.

[154] A.A. Tseng et al. "Electron beam lithography in nanoscale fabrication: recent development". In: *IEEE Transactions on Electronics Packaging Manufacturing* 26.2 (Apr. 2003), pp. 141–149. ISSN: 1521-334X.

[155] Ampere A. Tseng, Andrea Notargiacomo, and T. P. Chen. "Nanofabrication by scanning probe microscope lithography: A review". In: *Journal of Vacuum Science and Technology B* 23 (2005), p. 877. ISSN: 0734-211X.

[156] M.L. Tseng et al. "Fabrication of multilayer metamaterials by femtosecond laser-induced forward-transfer technique". In: *Laser and Photonics Reviews* 6.5 (July 2012), pp. 702–707.

[157] Buddhisha Udugama et al. "Diagnosing COVID-19: The Disease and Tools for Detection". In: *ACS Nano* 14.4 (Mar. 2020), pp. 3822–3835.

[158] C. Vericat et al. "Self-assembled monolayers of thiolates on metals: a review article on sulfur-metal chemistry and surface structures". In: *RSC Adv.* 4.53 (2014), pp. 27730–27754.

[159] C. Vericat et al. "Self-assembled monolayers of thiols and dithiols on gold: new challenges for a well-known system". In: *Chemical Society Reviews* 39.5 (2010), p. 1805.

[160] Ruggero Verre et al. "Transition metal dichalcogenide nanodisks as high-index dielectric Mie nanoresonators". In: *Nature Nanotechnology* 14.7 (May 2019), pp. 679–683.

[161] Jian Wang. "Metasurfaces enabling structured light manipulation: advances and perspectives". In: *Chinese Optics Letters* 16 (2018), p. 050006. ISSN: 1671-7694.

[162] Zhongwu Wang et al. "Microstructured Ultrathin Organic Semiconductor Film via Dip-Coating: Precise Assembly and Diverse Applications". In: *Accounts of Materials Research* 1.3 (Nov. 2020), pp. 201–212.

[163] Stephen R. Wasserman, Yu Tai Tao, and George M. Whitesides. "Structure and reactivity of alkylsiloxane monolayers formed by reaction of alkyltrichlorosilanes on silicon substrates". In: *Langmuir* 5.4 (July 1989), pp. 1074–1087.

[164] R.W. Wood. "On a remarkable case of uneven distribution of light in a diffraction grating spectrum". In: *The London, Edinburgh, and Dublin Philosophical Magazine and Journal of Science* 4.21 (Sept. 1902), pp. 396–402.

[165] Chihhui Wu et al. "Spectrally selective chiral silicon metasurfaces based on infrared Fano resonances". In: *Nature Communications* 5.1 (May 2014).

[166] Pin Chieh Wu et al. "Dynamic beam steering with all-dielectric electro-optic III-V multiple-quantum-well metasurfaces". In: *Nature Communications* 10.1 (Aug. 2019).

[167] R. Wüest et al. "An efficient proximity-effect correction method for electron-beam patterning of photonic-crystal devices". In: *Microelectronic Engineering* 67-68 (June 2003), pp. 182–188.

[168] Tongfang Xiao et al. "In Vivo Analysis with Electrochemical Sensors and Biosensors". In: *Analytical Chemistry* 89.1 (Nov. 2016), pp. 300–313.

[169] Jiahao Yan et al. "New type high-index dielectric nanosensors based on the scattering intensity shift". In: *Nanoscale* 8.11 (2016), pp. 5996–6007.

[170] Ting Yang et al. "Point-of-Care RNA-Based Diagnostic Device for COVID-19". In: *Diagnostics* 10.3 (Mar. 2020), p. 165.

[171] Yuanmu Yang et al. "All-dielectric metasurface analogue of electromagnetically induced transparency". In: *Nature Communications* 5.1 (Dec. 2014).

[172] Yuanqing Yang, Qiang Li, and Min Qiu. "Controlling the angular radiation of single emitters using dielectric patch nanoantennas". In: *Applied Physics Letters* 107.3 (July 2015), p. 031109.

[173] Yuhan Yao et al. "Line width tuning and smoothening for periodical grating fabrication in nanoimprint lithography". In: *Applied Physics A* 121.2 (June 2015), pp. 399–403.

[174] Yuhan Yao et al. "Nanoimprint-defined, large-area meta-surfaces for unidirectional optical transmission with superior extinction in the visible-to-infrared range". In: *Optics Express* 24.14 (June 2016), p. 15362.

[175] Ozlem Yavas, Mikael Svedendahl, and Romain Quidant. "Unravelling the Role of Electric and Magnetic Dipoles in Biosensing with Si Nanoresonators". In: *ACS Nano* 13.4 (Mar. 2019), pp. 4582–4588.

[176] Filiz Yesilkoy et al. "Ultrasensitive hyperspectral imaging and biodetection enabled by dielectric metasurfaces". In: *Nature Photonics* 13 (2019), pp. 390–396. ISSN: 1749-4885.

[177] Shinya Yoshioka and Shuichi Kinoshita. "Wavelength-selective and anisotropic light-diffusing scale on the wing of the Morpho butterfly". In: *Proceedings of the Royal Society of London. Series B: Biological Sciences* 271.1539 (Mar. 2004), pp. 581–587.

[178] Xin-Rong You et al. "Study of Au-Based and Au-Free Ohmic Contacts in AlGaN/GaN HEMTs by Recessed Patterns". In: *ECS Journal of Solid State Science and Technology* 10.7 (July 2021), p. 075006.

[179] Donghui Yu et al. "Biosensors in Drug Discovery and Drug Analysis". In: *Analytical Letters* 38.11 (Aug. 2005), pp. 1687–1701.

[180] Nanfang Yu and Federico Capasso. "Flat optics with designer metasurfaces". In: *Nature Materials* 13.2 (Jan. 2014), pp. 139–150.

[181] Nanfang Yu et al. "Light Propagation with Phase Discontinuities: Generalized Laws of Reflection and Refraction". In: *Science* 334.6054 (Oct. 2011), pp. 333–337.

[182] Lin Yuan et al. "Photocatalytic Hydrogenation of Graphene Using Pd Nanocones". In: *Nano Letters* 19.7 (June 2019), pp. 4413–4419.

[183] Meral Yüce, Elif Filiztekin, and Korin Gasia Özkaya. "COVID-19 diagnosis —A review of current methods". In: *Biosensors and Bioelectronics* 172 (Jan. 2021), p. 112752.

[184] Anatoly V Zayats and Igor I Smolyaninov. "Near-field photonics: surface plasmon polaritons and localized surface plasmons". In: *Journal of Optics A: Pure and Applied Optics* 5.4 (June 2003), S16–S50.

[185] Chao Zhang et al. "Al-Pd Nanodisk Heterodimers as Antenna-Reactor Photocatalysts". In: *Nano Letters* 16.10 (Sept. 2016), pp. 6677–6682.

[186] Cheng Zhang et al. "Low-loss metasurface optics down to the deep ultraviolet region". In: *Light: Science and Applications* 9.1 (Apr. 2020).

[187] Feng Zhang et al. "Chemical Vapor Deposition of Three Aminosilanes on Silicon Dioxide: Surface Characterization, Stability, Effects of Silane Concentration, and Cyanine Dye Adsorption". In: *Langmuir* 26.18 (Aug. 2010), pp. 14648–14654.

[188] Junxi Zhang, Lide Zhang, and Wei Xu. "Surface plasmon polaritons: physics and applications". In: *Journal of Physics D: Applied Physics* 45.11 (Feb. 2012), p. 113001.

[189] Qianzhe Zhang et al. "Micro/nanostructure engineering of epitaxial piezoelectric α-quartz thin films on silicon". In: *ACS Applied Materials & Interfaces* 12.4 (Dec. 2019), pp. 4732–4740.

[190] Xiao-ling Zhang et al. "Design and Performance of a Portable and Multichannel SPR Device". In: *Sensors* 17.6 (June 2017), p. 1435.

[191] Jing Zhao et al. "Glycan Determinants of Heparin-Tau Interaction". In: *Biophysical Journal* 112.5 (Mar. 2017), pp. 921–932.

[192] Nikolay I. Zheludev and Yuri S. Kivshar. "From metamaterials to metadevices". In: *Nature Materials* 11.11 (Oct. 2012), pp. 917–924.

[193] Lin Zhou et al. "3D self-assembly of aluminium nanoparticles for plasmon-enhanced solar desalination". In: *Nature Photonics* 10.6 (Apr. 2016), pp. 393–398.

[194] Zheng-Tao Zhu et al. "Humidity sensors based on pentacene thin-film transistors". In: *Applied Physics Letters* 81.24 (Dec. 2002), pp. 4643–4645.

[195] Jian Zi et al. "Coloration strategies in peacock feathers". In: *Proceedings of the National Academy of Sciences* 100.22 (Oct. 2003), pp. 12576–12578.

[196] Chengjun Zou et al. "Resonant dielectric metasurfaces: active tuning and nonlinear effects". In: *Journal of Physics D: Applied Physics* 52.37 (July 2019), p. 373002.

"Tutti i matematici sono pigri, ma non tutti i pigri sono matematici."